Multi-Wavelength Study Of Blazar Flares

Department of Astronomy and Astrophysics
Raman Research Institute
Bangalore-560 080, India

Thesis submitted for the degree of

Doctor of Philosophy
to
Jawaharlal Nehru University
New Delhi - 110067, India

by

Avik Kumar Das

Supervisor: **Nayantara Gupta**

Declaration of Original and Sole Authorship

I, Avik Kumar Das, declare that this thesis entitled *Multi-Wavelength Study Of Blazar Flares* and the data presented in it are original and my own work under the supervision of Dr. Nayantara Gupta. I confirm that the work presented here has not been submitted for the award of any other degree, diploma, membership, associateship, fellowship, etc. of any other university or Institute. I further confirm that references to the work of others have been clearly acknowledged. Quotations from the work of others have been clearly indicated, and attributed to them and in cases where others have contributed to part of this work, such contribution has been clearly acknowledged and distinguished from my own work. I have also run the thesis through the Turnitin software.

Avik Kumar Das
Research Fellow, RRI

Date:

Dr. Nayantara Gupta
Thesis Supervisor

Raman Research Institute,
Bangalore – 560 080
INDIA

Certificate

This is to certify that the thesis entitled " *Multi-Wavelength Study Of Blazar Flares*" submitted by Mr. Avik Kumar Das for the award of the degree of Doctor of Philosophy to the Jawaharlal Nehru University, is his original work done under my supervision and guidance, at the Raman Research Institute. This thesis has not been submitted or published for any other degree or qualification to any other university or institute.

Tarun Souradeep

Signature:
Prof. Tarun Souradeep
Director & Professor, RRI

Signature: Nayantara Gupta
Dr. Nayantara Gupta
Thesis Supervisor

Date:

Raman Research Institute,
Bangalore — 560080
INDIA

Abstract

Blazars are the most powerful Active Galactic Nuclei (AGNs) with relativistic jets oriented close to the observer's line of sight. Their total spectral energy distributions (SEDs) show two hump like structures. One peaking in low energy band (IR - X-ray) and another in high energy band (X-ray – gamma-ray). Low energy peak is well described by synchrotron emission. The origin of high energy peak is still under debate. However, we have two different models (leptonic and hadronic) that can explain the high energy peak. A sequence of blazar sub-classes, from FSRQ to low frequency peaked BL LAC objects (LBLs) to high frequency peaked BL LACs (HBLs), can be defined through the presence or absence of emission lines in their optical spectra and the peak frequencies of the synchrotron emission.

This thesis aims to understand the multi-wavelength properties of FSRQ type blazars. Temporal and spectral studies are done for two FSRQs in the multi-wavelength regime, from gamma-ray to optical and radio waveband.

Gamma-ray flares in the long-term light curve of 3C 454.3

3C 454.3 is frequently observed in the flaring state. The long-term light curve of this source has been analyzed with 9 years (August 2008 - July 2017) data from the Fermi-LAT detector. Five major flares and one quiescent state have been identified. The Flares have multiple phases, which include pre-flare, flare, post-flare, and plateaus. Even these flaring phases have several peaks. The estimated rise and decay time of the flares have been compared with the same observed from other similar sources. The modeling of gamma-ray spectral energy distributions show that in most cases Log-parabola function gives the best fit to the data. A time-dependent leptonic modelling of two flares has been done, for which simultaneous multi-wavelength data are available. These two long-lasting flares Flare-2A and Flare-2D, continued for 95 days and 133 days, respectively. The average values of Doppler factor, injected luminosity in electrons, size of the emission region, and the magnetic field in the emission region are used in modeling these flares. The emission region is assumed to be in the broad-line region in our single-zone model. The energy losses (synchrotron, synchrotron-self Compton, external Compton) and escape of electrons from the emission region have been included while doing the modelling. Although the total jet powers required to model these flares with leptonic models are higher than other sources, they are always found to be lower than the Eddington luminosity of 3C 454.3. The time variations in Doppler factor or the injected luminosity in electrons over short time scales have been studied to model the light curves of some peaks during flares.

Multi-wavelength study of 4C+28.07

4C+28.07 is a γ-ray Flat Spectrum Radio Quasar (FSRQ) type source. It is often monitored at different frequencies, though long-term multi-wavelength data of this source have not been modelled in detail before. Three major flares have been identified in the long-term 10 days binned γ-ray light curve history (Aug 2008 - May 2020). These flares are further studied in 3 days binning to identify the different states of activity (e.g., pre-flare, flare, etc.) by Bayesian block representation. γ-ray spectral analysis of these different activity phases has been performed, and the best fit model for its spectra is found to be a Log-parabola model. The correlation of simultaneous γ-ray light curves with the optical & radio counterparts in these flaring states have also been studied. We have reported the results of correlation study with 95% significance level. A large time delay is found between radio and gamma-ray data for two flares, indicating two emission zones. We have fitted the multi-wavelength data with a two zone leptonic model. In this two-zone leptonic model, the maximum required power in the jet is 9.64×10^{46} erg sec^{-1}, which is lower than its Eddington luminosity, 2.29×10^{47} erg sec^{-1}, of the source.

From the above studies, we can understand more about the physical properties of the FSRQs blazars, such as magnetic fields in the emission region, minimum & maximum Lorentz factors of the injected electrons, and their spectral indices. From the variability study of the γ-ray light curve, we can estimate the size of the γ-ray emission region in the jets, which is used in multi-wavelength SEDs modelling. Thus this thesis includes a detailed study on long-term behaviour of two important FSRQs, which would be helpful to compare in the future with other similar sources.

Acknowledgements

This part is one of the most difficult to write if someone takes it too seriously! Emotions and memories both play an essential role in this part. Either you acknowledge all the person you met from the beginning of your life (okay..that's an ideal case), or don't acknowledge anyone, leave it here. Since I should always take the middle path (my academic records help me to realize that!), I will mention those names which are related to RRI or known to me at a personal level.

First of all, I want to express my gratitude to my Ph.D. supervisor, Dr. Nayantara Gupta, for guiding me. A special thanks to Dr. Raj Prince for thesis proofreading. I have also learned many technical things from him. I want to thank prof. Shiv Sethi for fruitful discussions during my Ph.D days and keeping my motivation in physics alive.

I would like to thank Sudeb da and Atanu da from IISC, with whom I spent most of the time discussing physics in coursework days. That is the best academic company in my Ph.D life. I have learned a lot of things from them. After being detached from them, Dipak and Tanuman filled that gap. Thanks to them. I would also like to thank Narendranath Patra. I have learned python coding from him, which has been significantly influential in my work.

I thank my other group juniors and seniors: Agnibha, Sandeep, and Aditi for fruitful discussions. Tea break with Agnibha at 3 p.m. will be missed.

I thank all my RRI friends and seniors: Maheswar Da, Rishab, Bapan, Sagar da, Anindya da, Kaushik da, Sanchari, Shovan, Swarnadeep, Abhishek, Ion for creating a friendly environment here. I will miss the Friday nights with Maheswar da and Anindya da. Thanks to Saikat and Ranita di for lending their helping hands and supports in my critical time.

Last but not least, I would like to express my sincerest gratitude to my family members for their constant support and love. A special thanks to my beloved 'Kamalika' for making this journey beautiful and memorable. Without them, this journey is meaningless.

To my Father...

(1957 - 2018)

who always used to tell me -

"...please study hard...we have nothing but education..."

List of publications

- * "Gamma-Ray Flares in the Long-term Light Curve of 3C 454.3",

  Avik Kumar Das, Raj Prince, Nayantara Gupta, 2020, ApJS, 248, 8

- ** "Multi Wavelength Study of 4C+28.07",

  Avik Kumar Das, Raj Prince, Nayantara Gupta,

  Accepted for publications in ApJ

Other publication

- "Spectral Modeling of Flares in Long Term Gamma-Ray Light Curve of PKS 0903-57",

  Sandeep Kumar Mondal, Raj Prince, Nayantara Gupta, **Avik Kumar Das**

  Accepted for publications in ApJ

*Chapter-3
**Chapter-4

Contents

List of Figures

List of Tables

Chapter 1

Introduction

Active Galactic Nuclei (AGNs) are among the most spectacular and luminous objects in the universe. Only a few percent of galaxies [1] show very high energetic activity in the nuclei, galaxies of this type are known as AGN. Several special properties such as very small angular size, multi-wavelength spectra, variability in the light curves, etc. distinguish the AGNs from normal galaxies. AGNs are about 10 - 10^4 times more luminous than normal galaxies and emit radiation in radio to gamma-ray frequencies. It is believed that the inner part of all AGNs consists of a rotating super massive black-hole (SMBH) with mass in the range of 10^6 to $10^{10} M_\odot$, a rotating accretion disk from where matter falls inwards to the central SMBH and highly relativistic jets which are ejected from the two poles of SMBH and perpendicular to the accretion disk. In addition, there are ionized gaseous cloud regions like the Broad-Line Region (BLR), Narrow-Line Region (NLR), and molecular gas-dust region like Dusty Torus (DT) located in the outer part of the system. Emission spectra (Thermal + Non-thermal) of these regions are different from one another, which make multi-wavelength spectra of AGNs distinguishable from those of normal galaxies and other stellar objects.

1.1 History of AGN

The first spectroscopic detection of AGN NGC 1068 and NGC 3031 (also known as M81) was reported by Edward A. Fath in 1908 at Lick observatory bulletin [2]. After a decade, Heber D. Curtis first time discovered the AGN jet of M87 (also known as NGC 4486 or 3C274) from the same observatory [3]. He quoted in his paper about the jet - "...A curious straight ray lies in a gap in the nebulosity in p.a 20°, apparently connected with the nucleus by thin line of matter...". In the same year, a higher-resolution spectrum of NGC 1068 was obtained by Vesto M. Slipher at Lowell Observatory, which shows a similar emission line as planetary nebulae [4]. Soon after his discovery, several authors reported the presence of similar kind of emission lines in other AGN systems ([5], [6]). In 1943, an American astronomer Carl K. Seyfert, published the optical spectra results of several galaxies (NGC 1068, NGC 1275, NGC 3516, NGC 4051, NGC 4151 & NGC 7469), which have high central brightness and broader nuclear emission lines [7]. In his work, he found two main characteristics of these galaxies - i) the existence of broader emission lines in the spectra and ii) hydrogen lines are broader than other emission lines for few galaxies. For the first time, he gave a hint of a distinctive class of galaxies that are different from normal galaxies. Later, these types of galaxies are termed 'Seyfert galaxies' in honor of his pioneering work.

The progress in radio observation by Karl G. Jansky (in 1932) added further attention to galactic and extra-galactic astronomy. In 1939, Grote Reber discovered a radio galaxy - Cygnus A, which later played an important role in AGN studies. After that, Walter Baade and Rudolph Minkowski identified the radio sources in Cassiopeia and Puppis A with unusual type galactic emission along with the Cygnus A [8]. Several radio surveys was conducted between late 1950 to mid 1970 by different astronomical group across the world and published catalogs like 3C [9] & 3CR [10], PKS [11], 4C ([12], [13]), AO [14], Ohio ([15], [16]). These surveys found many new bright radio sources, and some of them also have optical counterparts. Few of these sources showed star-like (quasi-stellar) appearance in the photographic image but with much broader and stronger emission lines. Later, these types of sources are named as 'Quasars'.

X-ray observation started in the 1960s and 1970s, which suggested that both Seyfert galaxies and Quasars are also powerful sources in X-ray wavelength [17]. Most of these X-ray emissions emerge mainly from the inner part of the AGN system.

Gamma-rays are mainly detected from radio-loud AGNs, whose relativistic jets are aligned close to the line of sight of observers [18]. This subclass of AGNs are called Blazars (Blazars $\in$ AGN). The study of AGNs at gamma-ray regime started in 1991 after the launch of Compton Gamma-Ray Observatory (CGRO). The Energetic Gamma-Ray Experiment Telescope (EGRET) on CGRO, which covered the energy range between 20 MeV to 30 GeV detected 93 Blazars (66 high confidence + 27 low confidence detection) by the end of the mission timeline [19]. At the same time, ground-based gamma-ray telescope discovered several sources in Very High Energies (VHE) $>$ 100 GeV. After the launch of the Fermi-Large Area Telescope (Fermi-LAT) in 2008 [20], thousands of gamma-ray sources were detected [21], which provided an large wealth of data to explore the multi-wavelength emission from AGNs.

1.2 AGN Classification

AGNs can be classified into several classes and sub-classes based on their radio-loudness and width of the emission lines. Ratio of the radio to the optical luminosity ($\frac{L_{rad}}{L_{opt}}$) defines the radio-loudness. The distribution of this quantity is Bi-modal [22]. Hence it is good to divide the population into two groups - Radio loud and Radio quiet AGNs with a dividing line of $\frac{L_{rad}}{L_{opt}} \sim 10$, where L_{rad} and L_{opt} are the luminosity at 5 GHz radio band and optical B-band (5000 A$^{\circ}$) respectively [23]. Depending on the width of the emission (W) lines, AGNs can also be divided into two groups - Type-1 and Type-2 AGNs. The dividing line in this case is 1000 km/sec ($W >$ 1000 km/sec for Type-1 & $W <$ 1000 km/sec for Type-2 AGNs). Below, we describe the AGN classification scheme as discussed in Urry and Padovani [23].

1.2.1 Radio-quiet AGN

i) **Type-1 Seyfert:** Type-1 Seyfert galaxies are bright in Ultra-Violet (UV) and X-ray wavelength e.g. for NGC 5548, apparent magnitude is ~ 13.3 in the V band [24] and X-ray flux in 0.2 - 10 KeV energy band is $\sim 4 \times 10^{-14}$W m^{-2} [25]. They have a very bright nucleus which emits continuum emissions. Both broad and narrow lines are present in their spectra. The width of the broader emission lines can be extended up to $\sim 10^4$ km/sec ([26], [27]).

ii) **Type-2 Seyfert:** Type-2 Seyfert galaxies are bright in the infrared & visible wavelength, and also have bright cores. According to, Ulvestad and Wilson [28], these types of galaxies are more luminous than type-1 Seyfert galaxies in radio band (VLA; 6 - 20 cm observation). Spectra of these galaxies contain mainly narrow line emission [29] with the maximum width of the order of ~ 1000 km/sec [30]. For example, NGC 3147 is believed to be the best candidate for type-2 Seyfert galaxy [31] with V (5510Å) and J band (IR 12200 Å) magnitude of 10.61 and 8.37 respectively. [1]

Depending on the properties of the optical spectrum, Seyfert galaxies can be divided into more classes such as Type 1.2, Type 1.5, Type 1.8, Type 1.9, which were introduced by Donald Osterbrock in 1981 [32].

1.2.2 Radio-loud AGN

i) **BLRG:** Broad Line Radio Galaxies or BLRGs are Type-1 radio-loud AGNs with broader H I, He I, and He II emission line spectra. These types of galaxies partially share some of the properties of Type-1 Seyfert galaxies, such as broad optical emission lines and an optical-UV bump in the spectra [33]. However, BLRGs have much weaker Fe II emission lines, larger Hα/Hβ & [O III]/Hβ ratios compared to type-1 Seyfert

[1] `https://theskylive.com/sky/deepsky/ngc3147-object`

galaxies [34]. Some of the examples of BLRGs are - PKS 2349-01, 3C 227, 3C 445 , 3C 120 etc.

ii) **Radio Quasars:** These are also Type-1 radio-loud AGN, but luminosity is higher than the BLRG sources. According to Padovani [35], these are the global version of BLRGs. Radio Quasars are further divided into Flat Spectrum Radio Quasars (FSRQs) and Steep Spectrum Radio Quasars (SSRQs). The spectral indices of FSRQs and SSRQs in radio band are $\alpha_r \lesssim 0.5$ and $\alpha_r \gtrsim 0.5$ respectively, assuming the flux at radio band, $F_r \propto \nu^{-\alpha_r}$. Some of the examples of FSRQs are - 3C 273, 3C 454.3, PKS 1510-089, 4C+28.07, etc. Whereas 3C 245, 3C 179, 3C 191, etc. are the examples of some SSRQs.

iii) **NLRG:** Spectra of Narrow Line Radio Galaxies or NLRGs contain mostly narrow emission lines. Sometimes the emission lines are weak or absent [36]. These are Type-2 radio-loud AGNs. They are often elliptical type galaxies and can be further classified into two different categories.

- **Fanaroff-Riley I radio galaxies (FR I):** The extreme outer parts (referred as 'lobes') of these type of sources are fainter compared to the cores and central regions. They are also referred as 'edge darkened' sources. FR I types galaxies have luminosities in the range of - 10^{21} to 10^{25} W Hz^{-1} sr^{-1} (at 178 MHz) [37]. Spectra of the lobes are steeper in nature. Nearly 80% of FR I galaxies have jets, which are often symmetric. Some of the examples of FR I galaxies are 3C 40, 3C 449, 3C 278, B2 0149+358, etc.
- **Fanaroff-Riley II radio galaxies (FR II):** This type of sources are brighter than FR I galaxies. The luminosity range ($> 10^{25}$ W Hz^{-1} sr^{-1}) of FR II type galaxies at 178 MHz was reported in Fanaroff and Riley [37]. They often have one-sided jets with several radio knots and lobes with hot spots [38]. In contrary to FR I galaxies, these sources are more luminous at the extreme outer parts. Due to this reason, FR II galaxies are also called 'edge brightened' sources.

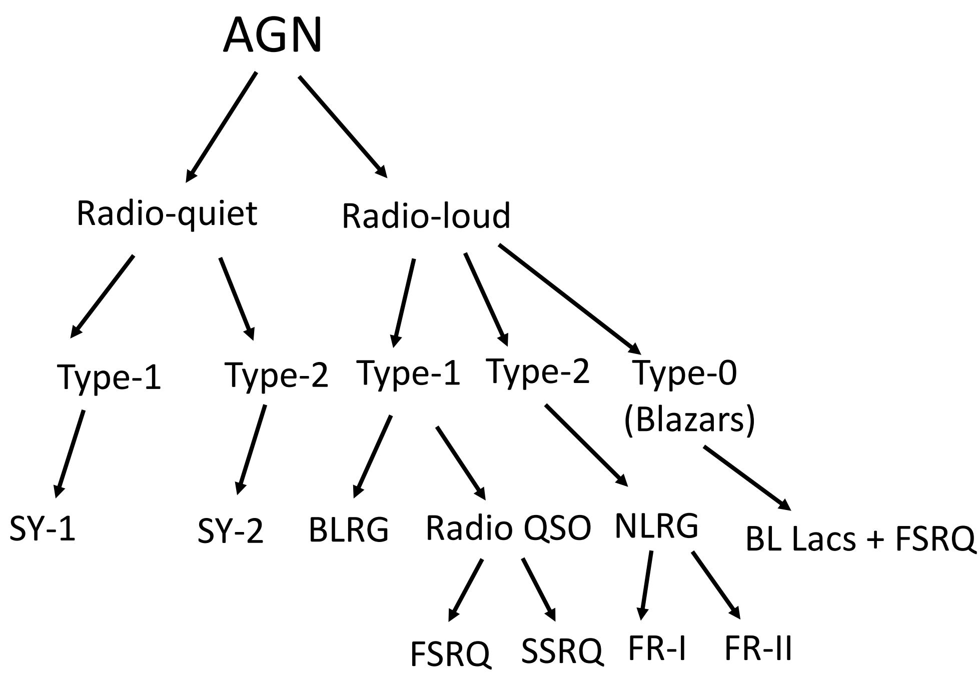

Figure 1.1: A complete tree chart of AGN classification. See text for more details

According to Baum et al. [39], the luminosities of emission lines of FR I galaxies are correlated with the optical luminosities of their host galaxies; whereas for FR II galaxies, this correlation is not observed. Other differences between FR I & FR II galaxies have also been described in Baum et al. [39]. Some of the examples of FR II galaxies are 3C 47, 3C 63, PKS 0349-278, PKS 0634-206, etc.

Apart from these, there are other types of sources, which are radio-loud but neither share the complete properties of Type-1 nor Type-2 radio-loud AGNs. These AGNs are called BL Lacertae objects or BL Lacs (referred to as 'Type-0 Radio Loud AGN'). These are highly polarized and variable sources. Generally, their spectra show weak emission lines.

FSRQs and BL Lacs share several similar properties such as rapid variability, high polarization, domination of non-thermal emission in their spectra, etc. These two types collectively form a new class- 'Blazars'. BL-Lacs can be further divided into more sub-classes. Properties of BL Lacs and FSRQs will be briefly discussed in the later section. A complete tree chart of AGN classification has been shown in Figure-1.1.

1.3 AGN Unification

The unified scheme suggests that the different classes of AGNs originate from the different viewing angles at which these sources are observed from earth. Thus the currently accepted unified model is based on the orientation of the system, also known as 'orientation-based unified model' ([40], [41], [42], [43]). This implies we are observing similar sources at different angles or orientations.

To visualize the unified scheme, first, we have to understand the morphology of an AGN. As we discussed earlier, the inner part of AGN consists of a bright central nucleus and a rotating accretion disk. This disk is covered by a thick molecular gas-dust region called 'Dusty torus' (Pier and Krolik [44], Pier and Krolik [45]). Two relativistic jets emerge from the two sides of the AGN, perpendicular to the accretion disk, and extend up to a few kpcs. BLRs are situated above the accretion disk and close to the SMBH, whereas NLRs are further from the SMBH.

If we observe the system from an edge-on location (when the angle between the accretion disk axis and the observer's line of sight is large), BLR regions are obscured by a dusty torus, but NLR regions are not. Also, according to the unified scheme, the presence of hot electrons far from the SMBH can produce broad lines in the polarised spectrum when the source is viewed from edge-on. These are the properties of Type-2 Seyfert galaxies. Similarly, the properties of the observed spectra from face-on view (when the angle between accretion disk axis and the observer's line of sight is small) will resemble Type-1 Seyfert galaxies. Both Type-1 and Type-2 Seyfert galaxies are radio quiet AGN and don't have prominent jets. All the radio-loud AGN have highly relativistic jets, and depending on the angle between jet axis & observer's line of sight, and they are also divided into

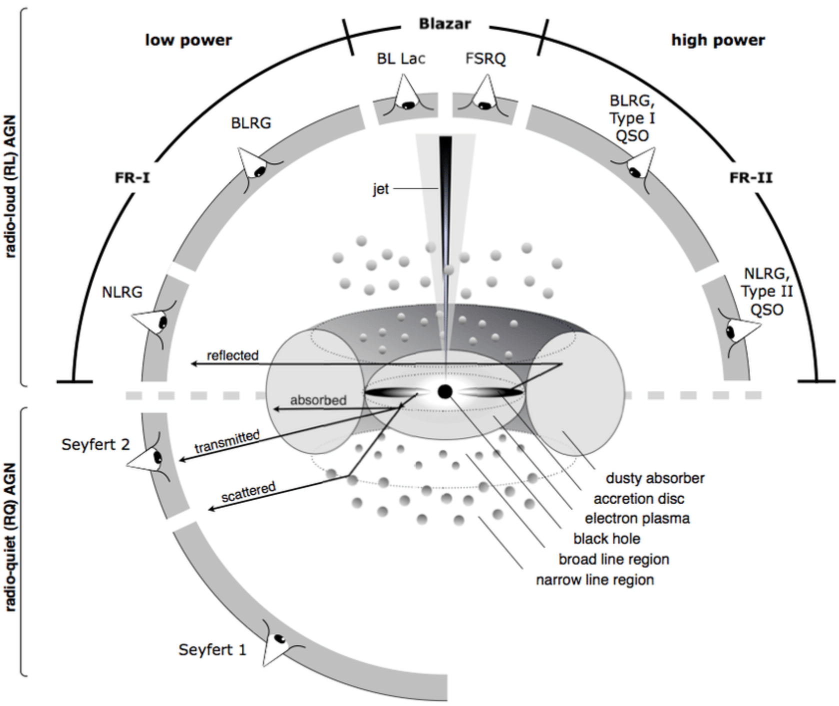

Figure 1.2: AGN unification scheme. Image is taken from Beckmann and Shrader [46].

different categories such as BLRG, NLRG, etc. When radio-loud AGNs are viewed from face-on (formally when the angle between observer's line of sight and jet axis $\lesssim 5°$), those sources are referred to as blazars. More details on the unified schemes for radio-loud AGN can be found in Urry and Padovani [23]. A complete picture of the AGN unified scheme is illustrated in Figure-1.2.

1.4 Different Regions of AGN

1.4.1 Accretion Disk

An accretion disk is basically formed by cold and diffused matter that initially has substantial angular momentum and is believed to be a source of magnetic fields around SMBH. Due to viscous forces and Magneto Rotational Instability (MRI; Balbus and Hawley [47]) angular momentum transfers outwards, and accreting matter solely falls into the SMBH with finite mass accretion rate. It is believed that because of the magnetic field in the accreting matter, there is a powerful outflow of energy from AGN via Blandford & Znajek (Blandford and Znajek [48]) or Blandford & Payne Mechanism (Blandford and Payne [49]). The disk spectrum is assumed to be purely thermal and peaks at the optical-UV regime, which is often used to model the spectra of quasars.

1.4.2 Dusty Torus

Dusty torus is a large region of warm molecular gas or dust that warps around the SMBH and BLR region and probably plays an important role for the unification of different types of AGN. Pier and Krolik [44] and Pier and Krolik [45] first suggested that this gas is distributed around SMBH as a torus or 'doughnut' shape. The size of this region is still not well understood. Earlier studies by Pier and Krolik [45] and Granato et al. [50] concluded that the size of this torus was greater than 100 pc, which was done by theoretical modelling of Spectral Energy Distribution (SED). Whereas High resolution IR observation show that region size is few pc only (Weigelt et al. [51], Mason [52], Tristram [53]). The disagreement between these two results can be resolved by taking into account the clumpy nature of the torus (see Nenkova et al. [54]). It is believed that optical-UV photons from the accretion disk surface is absorbed by the torus and re-emits at IR bands.

1.4.3 Broad Line Region (BLR)

Broad-Line Region (BLR) is made of many clumpy clouds (about $\sim 10^9$ clouds with a total mass of $\sim 10\ M_\odot$ [55]), which surround the SMBH and are spatially unresolved on the direct image. It is located at a distance $\sim$ 0.1 - 1 parsec (based on reverberation-mapping technique) away from the central engine, which means in the inner region of the dusty torus. It is believed that due to this region, AGN spectra show broad emission lines in optical and UV bands, which are created by photo-ionization in the outer regions of the accretion disk (Kollatschny and Zetzl [56]). By measuring the width of these lines, the estimated range of orbital speeds of these clouds are $\sim$ 1000 - 10000 km/sec [57]. The

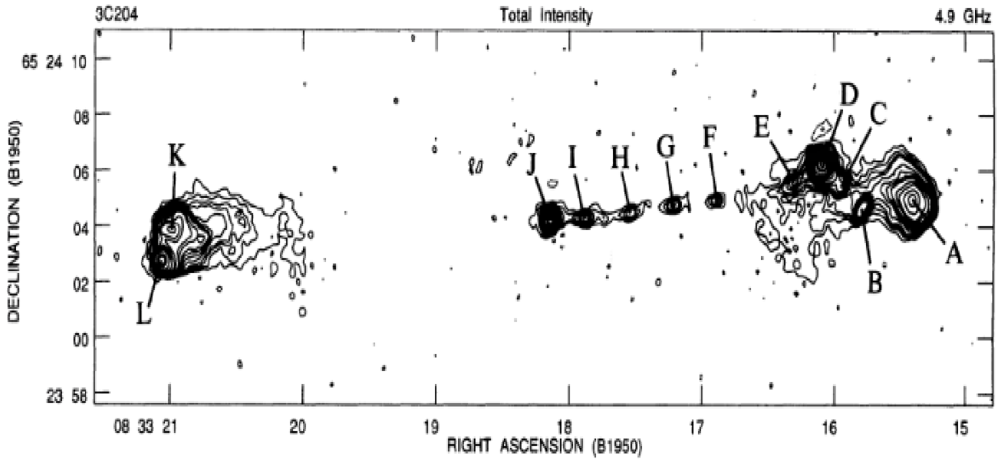

Figure 1.3: VLA intensity map of 3C204 at 4.9 GHz. Here J is the 'core' or central feature. A, B, C, D, E and K, L are the 'hotspots'. I, H, G, F are the 'knots'. This image is taken from Bridle et al. [66]

typical temperature of this region is assumed as $\sim 10^4$ K ([58], [59], [60]).

1.4.4 Narrow Line Region (NLR)

Narrow line region (NLR) is made of comparatively colder and less dense ($\sim 10^3$ - 10^6 cm^{-3}) ionized gases and clouds than BLR. It is located much further, typically $\sim$ 0.01 - 10 Kpc from the central engine [59]. This region is well studied and spatially resolved by many ground-based telescopes for several nearby Seyfert galaxies, which estimate the size of $\sim$ 100 - 1500 pc ([61], [62], [63]). The most distinctive emission lines of the NLR in optical band are: [O_{III}] and H_α + [N_{II}] lines with typical widths of $\sim$ 100 - 1000 km/sec (Bennert et al. [64]).

1.4.5 Jets and lobes

These are the most extended parts of AGN, emerging out from the two poles of SMBH and perpendicular to the accretion disk. Relativistically moving electron-proton or electron-positron plasma are ejected from the 'core' along with the high energy γ-ray radiations, which were confirmed by Jorstad et al. [65] in 2001. In this work, they showed that most

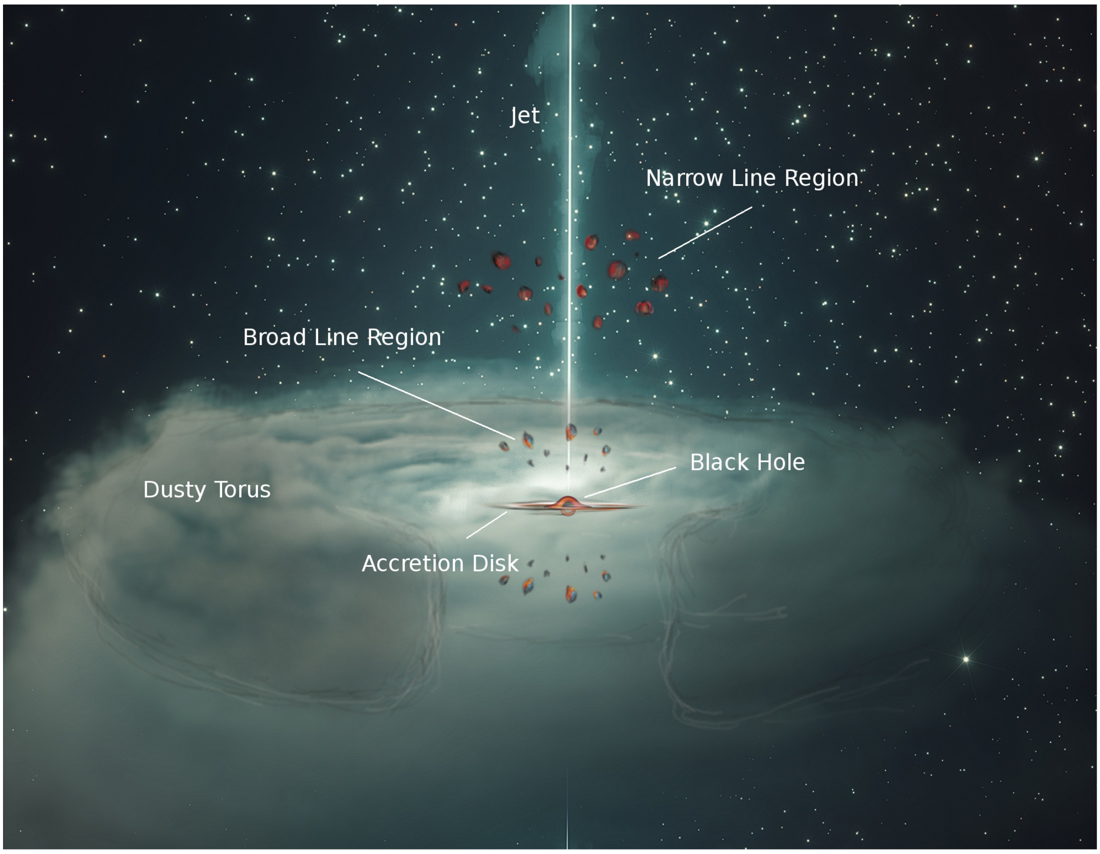

Figure 1.4: Artistic view of central part of the AGN. 'Lobes' are not shown here. Image is taken from: Heike Prokoph and DESY/Science Communication Lab. Link:`https://www.mpi-hd.mpg.de/hfm/HESS/pages/home/som/2020/03/Ref3`

of the epochs of γ-ray flares coincide with the epochs of zero separation of superluminal ejection from the 'core' within 1σ and 3σ uncertainties based on a Very Long Baseline Array (VLBA) monitoring program at 22 and 43 GHz. When these relativistic particles flow through extra-galactic medium, it interacts with the surroundings and continuously decelerates and ultimately produces a large structure of radio emission region at the two end of the core, known as 'lobes'. Within the lobes, there are several bright regions called 'hotspots'. Large filament-like structures (extended up to $\sim$ 100 Kpc - few Mpc; Blandford et al. [67]) connect the lobes with the nucleus of the active galaxies, which are basically called 'jets'. Inside the jets, there are also several bright regions, namely called 'radio knots' or shortly 'knots'. These different regions have been shown in Figure-1.3

A complete physical picture of AGN has been illustrated in Figure-1.4.

1.5 Study of Blazars

Blazars are the most violent and variable subclass of AGNs. The relativistic jet of the AGN can be closely oriented to the observer's line of sight within a few degrees. These types of objects are known as blazars. Edward Spiegel coined the term 'Blazar' in 1978 at the Pittsburgh Meeting for the first time to combine two different classes of rapid variable objects: BL Lacs and Optically Violent Variable (OVV) Quasars. Both sources are highly polarized in optical and radio bands (Fan et al. [68]) and emit radiation (mainly non-thermal), in all wavelengths, from radio to very high energy gamma-ray. Due to the relativistic boosting effect, the apparent brightness of blazars can be very high (e.g., observed brightness could be $\sim 10^5$ times more than the intrinsic brightness!).

1.5.1 Jet launching mechanism

Various issues such as the shining of jets, particle acceleration mechanism etc., can be addressed if we know properly about the launching mechanism of AGN jets. For this reason, Blazars study in multi-wavelength regime is instrumental to know directly or indirectly more about the properties of jet and the inner core.

There are two well-known theories, Blandford-Znajek (Blandford and Znajek [69]) and Blandford-Payne (Blandford and Payne [49]), which can explain the launching mechanism. Later these theories were further studied and confirmed via GRMHD simulations by several authors (Meier et al. [70], Semenov et al. [71], Tchekhovskoy et al. [72]). However, there is no direct observational evidence of any of these theories. According to the Blandford-Znajek mechanism, energy and angular momentum can be extracted from the rotational energy of the Kerr black hole. This is essentially electromagnetic version of the Penrose process. In the Blandford-Payne mechanism, energy or matter outflow is possible centrifugally from the accretion disk surface if the bending angle (angle between the rotation axis of the accretion disk and magnetic field line) of the magnetic field line is greater than $30°$.

A considerable amount of magnetic fluxes are likely required for both of these processes. What are the sources of these magnetic fields? That is still an open question! A possible origin may be the Inter-Stellar Medium (ISM).

1.5.2 Different classes of blazars

Blazars are divided into different categories based on their emission lines, variability, and polarization properties in the optical band. In recent years, it is ubiquitous to divide these sources mainly into two categories- BL Lacs and FSRQs, which are described earlier in subsection-1.2.2. The main property of BL Lacs is the absence of strong and broad emission lines in the optical band. Equivalent width of emission lines in BL Lacs are $W_\lambda <$ 5 Å while for FSRQs, it is $W_\lambda >$ 5 Å ([73], [74], [75]). The reason behind the absence of emission lines in BL Lacs is a controversial topic, but it is believed that accretion disk photons may be responsible for the emission lines in the optical band and the accretion process in BL Lacs are radiatively inefficient or Advection Dominated Accretion Flow (ADAF). The multi-wavelength or broadband SED (Spectral Energy Distribution) of blazars show two hump kinds of structures, one peaking at low energy (IR to soft X-ray) and the other peaking at higher energy (γ-ray) region. Depending on the peak frequency (ν_{peak}) at low energy hump, the BL Lacs are further divided into three categories. These are - low frequency peaked BL Lacs (LBL; $\nu_{peak} < 10^{14}$ Hz), Intermediate frequency peaked BL Lacs (IBL; $10^{14} < \nu_{peak} < 10^{15}$ Hz) and high frequency peaked frequency BL Lacs (HBL; $\nu_{peak} > 10^{15}$ Hz). Broadband SED of different classes and sub-classes have been shown in Figure-1.5 and Figure-1.6.

1.5.3 Observational Characteristics

Superluminal motion

In blazar jets, an emitting region moves with a relativistic velocity along the jet axis, and it makes a small angle to the observer's line of sight. From the observer's point of view,

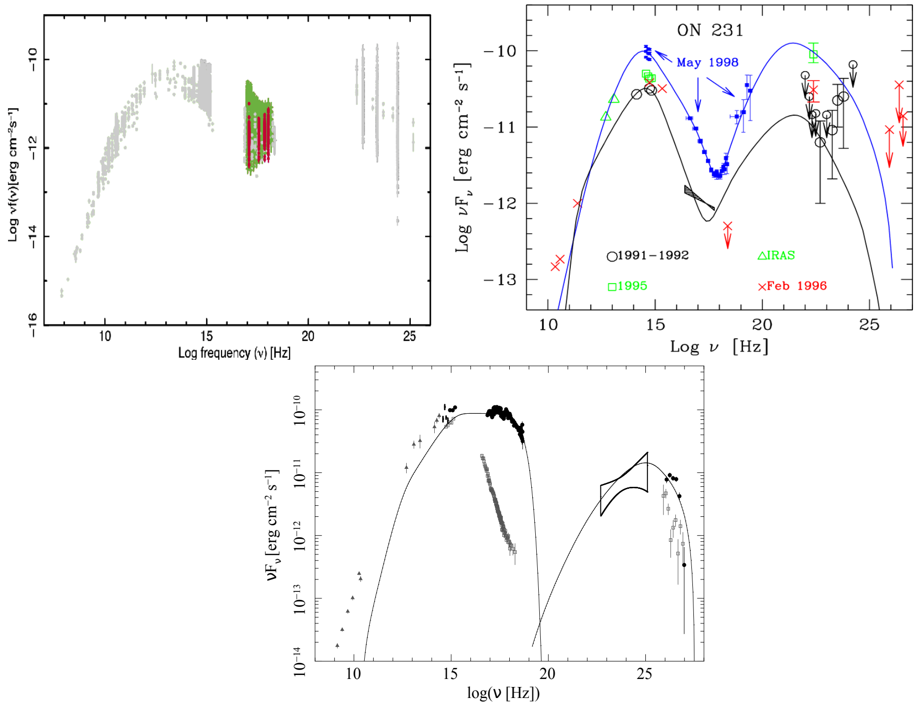

Figure 1.5: Multi-wavelength SEDs of LBL (OJ 287) at the top left panel (Giommi [76]), IBL (ON 231) at the top right panel (Tagliaferri [77]) and HBL (PKS 2005-489) at the bottom panel (Abramowski et al. [78]).

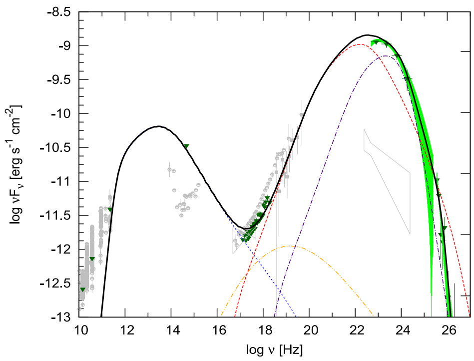

Figure 1.6: Multi-wavelength SED of FSRQ (PKS 1510-089). Image is taken from Barnacka et al. [79].

that emitting region will move faster than the speed of light. This phenomenon is known as 'Superluminal motion'. To visualize this, let us consider Figure-1.7.

Let us assume, a relativistically moving (from A to B with velocity v) emitting blob emits a photon from position A at time t_{e1}. After time Δt_e ($t_{e2} = t_{e1} + \Delta t_e$) from point

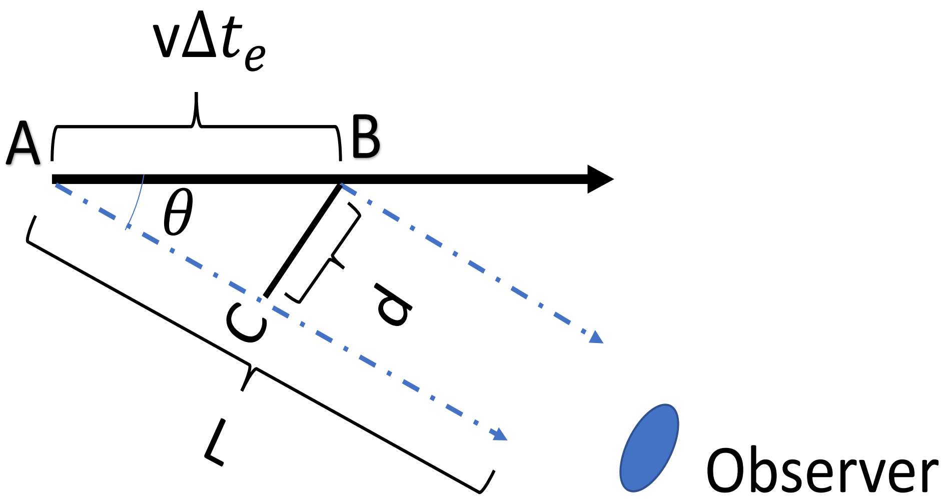

Figure 1.7: Illustration of superluminal motion

B, it emits a second photon in the direction of the observer. Now in the observer's frame, the time gap between these two emitted photons are-

$$\Delta t_{obs} = \frac{L - AC}{c} - \frac{L}{c} + \Delta t_e$$

or

$$\Delta t_{obs} = \Delta t_e \big(1 - \frac{v}{c}\cos\theta\big) \tag{1.1}$$

where, AC $= v\Delta t_e \cos\theta$. Observer measure the projected distance of the emitting blob, $d = v\Delta t_e \sin\theta$. So the apparent velocity measured by the observer -

$$v_{app} = \frac{d}{\Delta t_{obs}} = \frac{v\Delta t_e \sin\theta}{\Delta t_e(1 - \frac{v}{c}\cos\theta)}$$

or

$$\beta_{app} = \frac{\beta \sin\theta}{1 - \beta\cos\theta} \tag{1.2}$$

From the equation-1.2, we can see that apparent speed of the emitting blob can be greater than the speed of light.

Variability

Blazars' light curves show rapid variability in all wavelengths, from radio to high energy γ-ray band ([80], [81], [82]). The time scale of variability is much diverse, from minutes to months and even in years (Abdo et al. [83], Raiteri et al. [84], Shukla et al. [85]). The strong variable nature of blazars still remains unclear. But it is believed that short-term variability is caused by turbulent flow in the jets, whereas long-term variability is caused by the change in energy flow in the jets or related to the precession of jets. Variability

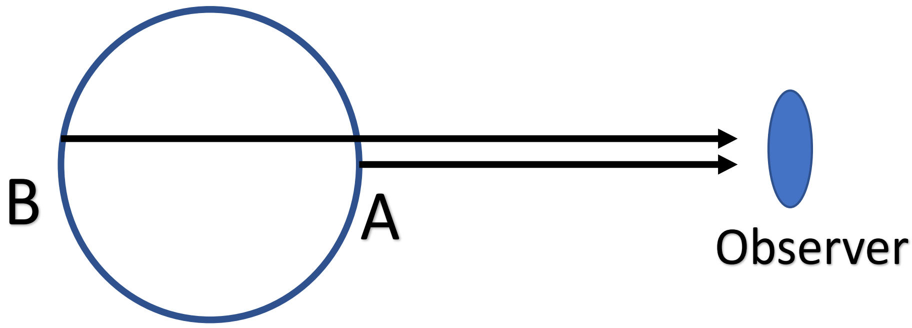

Figure 1.8: Illustration of variability time

time is used to constrain the size of the emission region for a particular wavelength. Let us assume that the computed variability time from the observed light curve is t_{var}^{obs}, which means the time difference (in observer's frame) between the emitted photons from point A and point B as illustrated in Figure-1.8. The upper limit of the emission region size in the jet frame can be given by the causality condition -

$$R' \leq \frac{c t_{obs}^{var} \delta}{1+z} \tag{1.3}$$

where, z and δ are the cosmological redshift and Doppler factor of the source respectively. These are correction factors for the jet frame.

Polarization

Polarization is another key feature of blazars. Observed radiation of blazars are polarized, especially in optical and radio band. The presence of synchrotron emission in the jets is evident from this phenomenon. It is also energy-dependent and varies adequately during flaring episodes. By measuring the polarization, we can understand more about the origin, confinement, and propagation of jets.

1.5.4 Emission mechanism

As we discussed earlier in section-1.5.2, blazars SED shows two hump kind of structure. There are two well-known models to explain this broadband SED, which will be briefly discussed in the next section.

Leptonic model

In the leptonic model, the low energy component is well described by the synchrotron emission of high energy electrons in the jets, while the high energy components are described by - i) Inverse Compton (IC) scattering of external seed photons (e.g., accretion disk, BLR, DT photons) by the relativistic electron populations, also called External Compton (EC) emission ii) Sychrotron Self Compton (SSC) Process. Various emission processes are described below. More details of these processes can be found in Rybicki and Lightman [86].

- **Synchroton emission:** When a charged particle moves relativistically in a magnetic field, it will produce synchrotron radiation. Due to the relativistic aberration, radiation is highly beamed (lies in a cone with a half angle of $\sim \frac{1}{\gamma}$) with respect to the observer's frame. Total emitted power ($P(\alpha)$) of a single charge q moving in a magnetic field B is given by -

$$P(\alpha) = \frac{2q^4}{3m^2c^4}\gamma^2 B^2 \beta^2 \sin^2 \alpha \tag{1.4}$$

where, β and m are velocity and rest mass of the particle respectively. α is the pitch angle of the helical trajectory. Lorentz factor is represented by $\gamma = \frac{1}{\sqrt{1-\beta^2}}$. For isotropic distribution of velocities, we can average this equation over solid angle, which gives -

$$P = \frac{1}{4\pi} \iint P(\alpha) d\Omega = \frac{1}{2} \int P(\alpha) \sin\alpha d\alpha$$

From equation-1.4, we get -

$$P_{syn} = \frac{4q^4}{9m^2c^4}\gamma^2\beta^2B^2 = \frac{4}{3}c\sigma_T\beta^2\gamma^2U_B \tag{1.5}$$

σ_T $(= \frac{8\pi}{3}\frac{q^4}{m^2c^4})$ and U_B $(= \frac{B^2}{8\pi})$ are the Thomson cross section and magnetic energy density respectively.

It can be shown that if energy distribution of particles follows power-law with index p, for sufficiently broad energy range, the radiation spectrum also follows power-law distribution but with spectral index of $\frac{p-1}{2}$.

- **Inverse Compton emission:** When a low energy photon interacts with a sufficiently high energy electron, the energy of the outgoing photon will increase. This process is known as Inverse Compton process, as it is opposite to the Compton emission. It is easy to use the electron center of momentum (COM) frame to calculate the energy lost by the electron (IC power) by this process. In the COM frame, the total scattered power by electron is given by -

$$\frac{dE^e}{dt^e} = c\sigma_T U^e_{rad} \tag{1.6}$$

U^e_{rad} and σ_T are the energy density of incoming photons (in COM frame) and Thomson cross section respectively. Here, we assume that the incoming photon energy (ν^e) in COM frame is much less than the rest mass energy of electron (Thomson limit; $\nu^e << m_e c^2$) and also the energy transfer in the electron is negligible. $\frac{dE}{dt}$ is Lorentz invariant quantity ($\frac{dE^e}{dt^e} = \frac{dE^L}{dt^L}$). Energy density in the lab frame (U^L_{rad}) and COM frame are related as -

$$U^e_{rad} = \gamma^2 U^L_{rad}(1 - \beta\cos\theta)^2 \tag{1.7}$$

Put equation-1.7 into equation-1.6 and averaged out over solid angle (isotropic distribution of photons) -

$$\frac{dE^L}{dt^L} = c\sigma_T\gamma^2 U^L_{rad} < (1 - \beta\cos\theta)^2 >= c\sigma_T\gamma^2 U^L_{rad}(1 + \frac{1}{3}\beta^2) \tag{1.8}$$

so the total energy lost by the electron or IC power (P_{IC}) is -

$$P_{IC} = \text{scattered power of electrons} - \text{incoming power of electrons}$$

or,

$$P_{IC} = c\sigma_T\gamma^2 U^L_{rad}(1 + \frac{1}{3}\beta^2) - c\sigma_T U^L_{rad} = \frac{4}{3}c\sigma_T\beta^2\gamma^2 U^L_{rad} \tag{1.9}$$

By using, $\gamma^2 - 1 = \gamma^2\beta^2$. We get the same expression as equation-1.5 but here magnetic energy density is replaced by incoming photon energy density.

If the incoming photon energy in COM frame is comparable to, or greater than the rest mass energy of electron ($\nu^e \sim m_e c^2$), then the scattering cross section is described by Klein-Nishina (KN) cross section. The total cross section (σ_{KN}) in this case is given by -

$$\sigma_{KN} = \frac{3}{4}\sigma_T\Big[\frac{1+x}{x^3}\Big\{\frac{2x(1+x)}{1+2x} - \ln(1+2x)\Big\} + \frac{1}{2x}\ln(1+2x) - \frac{1+3x}{(1+2x)^2}\Big] \tag{1.10}$$

where, $x = \frac{h\nu^e}{m_e c^2}$. In the extreme KN regime ($x >> 1$) electron loses greater amount of energy to the photon than Thomson regime ($x << 1$). The energy of the scattered photon (ϵ_f) is in this two limit - $\epsilon_f \sim \gamma^2 \epsilon_i$ for $x << 1$ and $\epsilon_f >> \gamma m_e c^2$ for $x >> 1$.

From the fundamental point of view (Quantum Electrodynamics), IC and synchrotron emissions, both processes are actually same. In case of IC emission, real photons are involved, and for the other case of synchrotron emission, virtual photons are involved.

Hadronic models

According to the hadronic model, the lower energy part of the SED is described by the same as the leptonic scenario (synchrotron emission of relativistic electrons). The high energy component is described by different hadronic processes, such as proton-proton, proton-photon interactions, and proton synchrotron emission.

In proton-proton interaction, high energy proton interacts with another proton inelastically and produced γ-rays and neutrinos via following channels -

$$p + p \longrightarrow p + p + \pi^0$$

$$p + p \longrightarrow p + n + \pi^+$$

$$p + p \longrightarrow p + p + \pi^+ + \pi^-$$

$$\pi^0 \longrightarrow 2\gamma$$

$$\pi^+ \longrightarrow \mu^+ + \nu_\mu$$

$$\pi^- \longrightarrow \mu^- + \bar{\nu_\mu}$$

$$\mu^+ \longrightarrow e^+ + \nu_e + \bar{\nu_\mu}$$

$$\mu^- \longrightarrow e^- + \bar{\nu_e} + \nu_\mu$$

In proton-photon interaction, high energy protons interacts with seed photons. Main channels of this interactions are (Mannheim [87]) -

$$p + \gamma \longrightarrow p + \pi^0$$

$$p + \gamma \longrightarrow n + \pi^+$$

π^0 and π^+ again decay into the same channels as above and produced γ-ray photons and different types of neutrinos. In this process, seed photon may come from the sychrotron emission of electrons (Mannheim [88]) or BLR, DT regions.

Apart from these, γ-ray can also be produced via synchrotron emission of protons, but for this process very high magnetic field ($\sim$ 100 G) is required (P_{syn} is inversely proportional to the mass of the particle).

Hadronic models are hotly debatable models in the blazars community. It can explain hard 'TeV' spectra, production of neutrinos in the jets. However, it can't explain the rapid variability observed in γ-ray and hard X-ray bands.

1.6 Motivation behind the study of Blazars

Blazars are one of the brightest and variable sources in the entire universe. Their extended jets are excellent extra-galactic laboratories to examine the radiative environment and underlying physical mechanisms. Blazars significantly emit non-thermal emissions and cover the whole electromagnetic spectrum from radio to very high energy γ-rays. Their multi-wavelength flux and spectral variability on different time scales are still not well understood to the blazar community. So, to understand this issue, a multi-wavelength study of blazars is necessary.

There are other several open issues on blazars physics -

i) The size and location of the emission regions in the jets.

ii) What is the compositions of jets? electron-positron, electron-protons or both?

iii) Physical origin behind Quasi Periodic Oscillations (QPO) in multi-wavelength light curves.

iv) Role of magnetic field in origin and propagation of the relativistic jets.

v) The distribution of particles in the emission regions and their acceleration mechanisms. How are these related to the observed spectra?

The understanding of these issues is only possible with good quality multi-wavelength temporal and spectral data. In this thesis, I have addressed some of these issues by analyzing and modelling the multi-wavelength data of blazars.

1.7 Overview of the thesis

The goal of this thesis is to understand the multi-wavelength properties of FSRQ type blazars. Temporal and spectral studies are done for two FSRQ sources in the multi-wavelength regime, from gamma-ray to optical and radio waveband. Leptonic model is used to describe the multi-wavelength SED of different flaring states. From this, we can know about the physical properties of the jets such as magnetic field, the maximum and minimum energy of electrons, etc. The chapters of the thesis are divided as follows -

Chapter-1 provides a brief introduction about the AGNs and blazars.

Chapter-2 describes the data reduction processes in multi-wavelength regime.

Chapter-3 discusses about the study of gamma-ray flaring states and results of leptonic modelling for the brightest flare in long-term light curve of 3C454.3.

Chapter-4 discusses about the multi-wavelength study of another FSRQ, 4C+28.07.

Chapter-5 concludes our findings from this thesis. Future directions are also mentioned.

Chapter 2

Multi-wavelength data reduction and analysis

Blazars are very bright sources in the universe and these are observed in multi-wavebands (from radio to very high energy gamma-ray). The data reduction process and analysis of various telescopes are briefly explained in this chapter.

2.1 Fermi Gamma-ray Space Telescope

This telescope (shown in Figure-2.1) was launched in 11th June, 2008, from Cape Canaveral by a Delta II 'Heavy' into an initial orbit of 565 km. It has orbital period of $\sim$ 96 minutes and cover the entire sky in survey mode with time period of $\sim$ 3.2 hour. This have two on-board instruments which are - i) Fermi-Large Area Telescope (Fermi-LAT) and ii) Gamma-ray Burst Monitor (GBM). Both have very large Field of View (FOV). The working goal of GBM is to detect the sudden change in the gamma-ray fluxes and alerts the LAT.

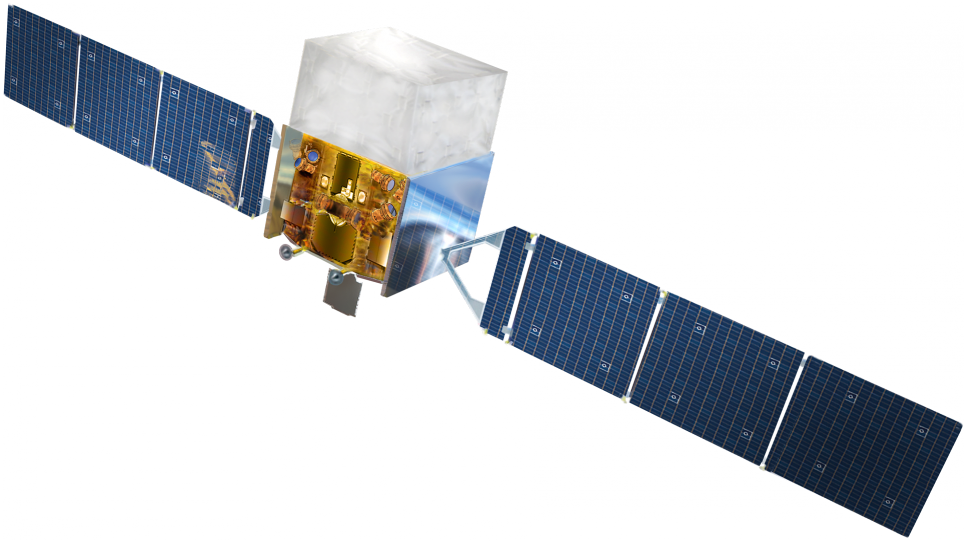

Figure 2.1: Fermi Gamma-ray Space Telescope. image is taken from Wikipedia.

2.1.1 Fermi-LAT

Fermi-LAT is an imaging pair conversion telescope, which covers a γ-ray energy range from 20 MeV to $>$ 300 GeV with energy resolution $<$15% at energy $>$100 Gev (Atwood et al. [89]). After penetrating into the detector, gamma-ray interact with one of the tungsten layer (tungsten has high Z value, pair production process dominates) and produced electron-positron pair. At the last layer of the LAT, there is a calorimeter, which is used to measure the energy of the pairs. These pairs are also tracked by series of silicon strip detectors. By this method LAT create a photon based (.PH) file which has reconstructed energy and directions. Structure of the LAT instrument has been illustrated in Figure-2.2

Fermi-LAT analysis

The Fermi-LAT data can be downloaded from the Fermi Science tools webpage[1]. Two kind of data files are available for particular time span. One is photon file which was already discussed above and another one is spacecraft file, which have information about the satellite (e.g. satellite's position and orientation at every 30 seconds time steps). The LAT is switched off when passes through the South Atlantic Anomaly to avoid the charge

[1]`https://fermi.gsfc.nasa.gov/cgi-bin/ssc/LAT/LATDataQuery.cgi`

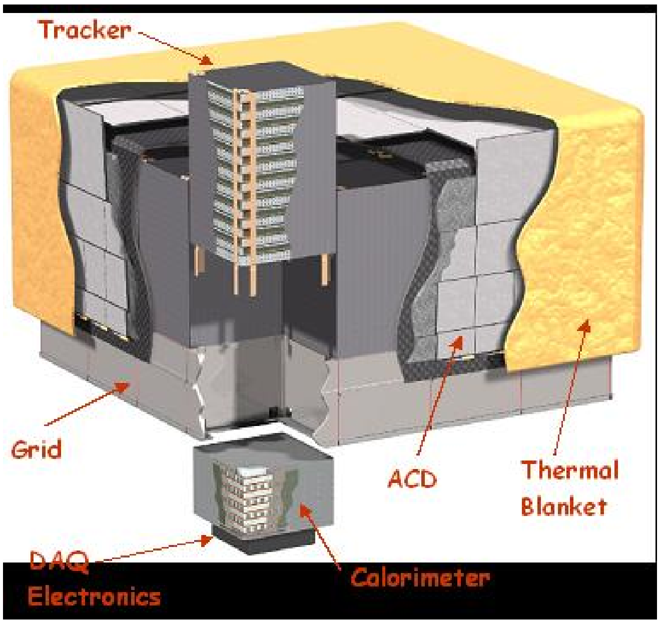

Figure 2.2: Structure of the Fermi-Large Area Telescope (Fermi-LAT). Image is downloaded from - `https://fermi.gsfc.nasa.gov/ssc/data/p7rep/analysis/documentation/Cicerone/Cicerone_Introduction/LAT_overview.html`

particles background.

The data is analyzed with the help of Fermi science tool software package, which includes a galactic diffuse emission model (gl_iem_v06.fits) and extra-galactic isotropic diffuse emission model (iso_P8R2_SOURCE_V6_v06.txt). The "unbinned likelihood analysis" (using python) method has been used to analyze the Fermi-LAT Pass8 data with appropriate selections and recommended cuts. "unbinned likelihood analysis" is preferred when the events number are low in each time bin. Whereas, the binned analysis is recommended for larger time bins and when the source is close to the bright background (e.g. the Galactic plane) region. The photon-like events are classified as "evclass = 128, evtype = 3" with energies ranging from 100 MeV to 300 GeV. Photons are extracted from the radius (region of interest or ROI) of 10° around the source and used a maximum zenith angle value of 90°, which is the standard value provided by the LAT instrument team, in order to avoid the γ-ray detection from Earth's limb. Filter expression "`DATA_QUAL`>0 && `LAT_CONFIG`==1" is implemented to select the good time interval data, which are recommended by the LAT team. Sometimes Filter expression "`DATA_QUAL`>0

&& `LAT_CONFIG`==1 && `ANGSEP(RA_SUN,DEC_SUN`,X,Y)>15" is also used to avoid time bins when the Sun could be close to the target (in this case less than 15°). Here, X & Y are the value of RA & DEC of the source respectively. The live time, exposure map, and diffuse response of the instrument have been computed subsequently for each event with the latest instrument response function (IRF) "`P8R2_SOURCE_V6`". To localize the source detection, a quantity called at "test statistic" (TS) is computed, which is defined as -

$$TS = -2\log\left(\frac{L_0}{L1}\right) \tag{2.1}$$

where L_0 and $L1$ are the maximum likelihood values for a given model without (null hypothesis) and with the point-like source at the position of the source. TS $\geq$ 25 is the standard selection criterion to choose the sources, which corresponds to $\sim$(TS)$^{\frac{1}{2}}$ or 5σ detection level.

2.2 Neil Gehrels Swift Observatory

Swift (shown in Figure-2.3) was launched on 20th November, 2004 by Delta 7320 rocket into low earth orbit. It is part of NASA's medium explorer (MIDEX) program. It has three on-board instrument- i) Burst Alert Telescope (BAT) ii) X-Ray Telescope (XRT) and iii) Ultraviolet and Optical Telescope (UVOT). The main goal of Swift is to monitor Gamma-ray Bursts (GRBs; Gehrels et al. [90]).

2.2.1 XRT-analysis

The working energy range of XRT is from 0.2 keV to 10 keV. It is operated in four different modes -

- **Imaging mode (IM)**: This mode has exposure time of 0.1 or 2.5 seconds and mainly used to dectect new GRB's position.

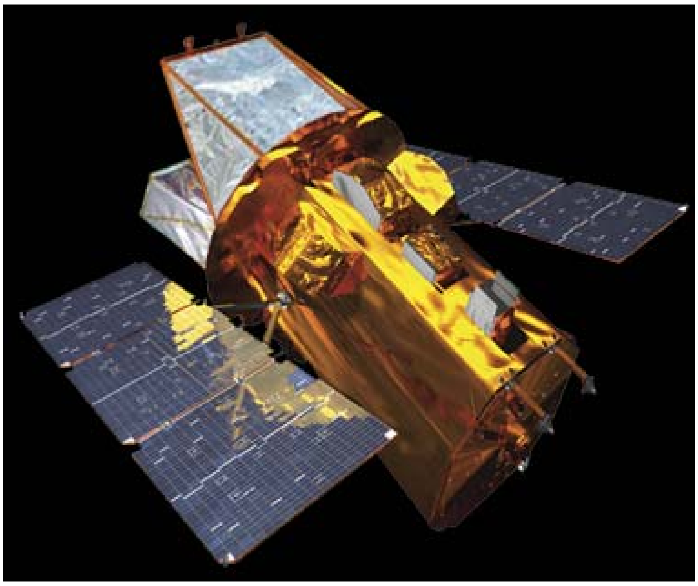

Figure 2.3: Neil Gehrels Swift Observatory. Image is downloaded from - `https://swift.gsfc.nasa.gov/`

- **Photo-Diode mode (PD)**: It has time resolution of 0.14 milliseconds and no spatial information. Currently this mode is disabled.
- **Windowed Timing mode (WT)**: It has time resolution of 1.8 millisecond's and used for bright sources. Image of WT mode data is 1-dimensional.
- **Photon Counting mode (PC)**: PC mode data is 2-dimensional (cover the region $\sim$ 24 arcmin) and used for low flux sources. It has time resolution of 2.5 milliseconds.

Other information about the instrument have been found in Burrows et al. [91].

The XRT data can be retrieved from the HEASARC website [2]. A task "xrtpipeline" (version 0.13.2) has been used to process the XRT data files for each observation set. The latest calibration files (CALDB version of 20160609) and standard screening criteria have been implemented in this process. A circular radius of 20" around the source and background region of 20" away from the source have been chosen to analyze the XRT data. A tool "xselect" has been used to extract the X-ray light curve and spectra. The tools called "xrtmkarf" and "grppha" have been used to create the redistribution matrix file (rmf)

[2] `https://heasarc.gsfc.nasa.gov/cgi-bin/W3Browse/swift.pl`

and ancillary response file (arf) and group the spectra of 30 counts bin^{-1} respectively. Subsequently, the grouped spectra have been modeled in XSPEC (version 12.10.0) with the "$tbabs * logparabola$" model.

2.2.2 UVOT-analysis

The UVOT (Ultra Violet and Optical Telescope) is a diffraction-limited with 12 arcsec (30 cm) aperture Ritchey-Chrétien reflector [3]. It covers wavelength range of 1700 - 6500 Å with a field of view of 17 × 17 arc-minutes.

Swift-UVOT (Roming et al. [92]) observed several blazars in all six filters: U, V, B, W1, M2, and W2 and the data can be obtained from HEASARC web-page [4]. The source region has been extracted from the 10" circular region around the source, and the background region has also been chosen with a radius of 25" away from the source. The source magnitudes have been extracted by the task "`uvotsource`" and corrected for galactic extinction (Schlafly and Finkbeiner [93]). Subsequently, these magnitudes have been converted into flux by using the zero-points (Breeveld et al. [94]) and conversion factors (Larionov et al. [95]).

2.3 Publicly available data

Below, we discuss about the publicly available data from different observatories which are used in this thesis.

2.3.1 Owens Valley Radio Observatory (OVRO)

OVRO is a 40 m radio telescope [5] which operates in 15 GHz waveband and part of a fermi support program since 2008. It has observed more than 1800 blazars till now and monitor them continuously twice per week. The detailed description of calibration & data

[3] `https://swift.gsfc.nasa.gov/about_swift/uvot_desc.html`
[4] `https://heasarc.gsfc.nasa.gov/docs/archive.html`
[5] `https://sites.astro.caltech.edu/ovroblazars/index.php?page=home`

reduction process have been discussed in Richards et al. [96]. 3C 286 source is used as primary calibrator.

2.3.2 Stewards Observatory

This observatory[6] is located in Tucson, Arizona (operated by university of Arizona) and also part of a fermi support program. It has three different telescopes: i) 2.3-m Bok reflector, ii) 0.9-m reflector and iii) 1.8-m reflector. It observes Fermi-LAT detected blazars in optical V and R band. Along with photometric observations it also provides V, R - band polarimetric data (Degree of polarization & Position angle). The details of the data reduction and calibration process are described in Smith et al. [97].

2.3.3 Catalina Surveys

Catalina surveys [7] are divided in two categories: i) Catalina Sky Survey (CSS), which searches for rapidly moving near earth objects (mainly comets and asteroids) and ii) Catalina Real-time Transient Survey (CRTS), which searches for stationary optical transients. CRTS provides optical V-band photometric data of several fermi detected blazars. The detailed process of data reduction can be found in Drake et al. [98].

[6] `http://james.as.arizona.edu/psmith/Fermi/`
[7] `http://nesssi.cacr.caltech.edu/DataRelease/`

Chapter 3

Gamma-Ray Flares in the Long-term Light Curve of 3C 454.3

3.1 Historical observation of 3C 454.3

The FSRQ (Flat Spectrum Radio Quasar) 3C 454.3, located at redshift 0.859, is frequently monitored due to its high flux variability. During an intense flare in 1992 it was observed by EGRET (Hartman et al. [99], Hartman et al. [100]), when its flux varied in the range of (0.4-1.4)$\times 10^{-6}$ photons cm^{-2} sec^{-1}. Subsequently, 3C 454.3 remained a source of interest for multi-wavelength observations due to its variable nature. This source was active in 2000 and even more in 2005. The 2005 outburst was recorded in optical and X-ray frequencies (Giommi [101]). The high activity of 3C 454.3 in autumn 2007 was observed by the Whole Earth Blazar Telescope (WEBT) in radio to optical frequencies. The gamma-ray satellite Astro-rivelatore Gamma a Immagini LEggero (AGILE) detected this source in late July and November-December of 2007 (Raiteri et al. [102]).

The AGILE 2007 November campaign was reported by Vercellone et al. [103]. AGILE, International Gamma-ray Astrophysics Laboratory (INTEGRAL), Swift, WEBT consortium, and the optical-NIR telescope Rapid Eye Mount (REM) observed 3C 454.3 during the campaign. During three weeks of the observation period, the average gamma-ray flux above 100 MeV was 1.7×10^{-6} photons cm^{-2} sec^{-1}. The source was extremely variable in the optical band. The gamma-ray emission was found to be correlated with optical emission. AGILE 2007 December campaign ([104]) observed this source with average flux 2.5×10^{-6} photons cm^{-2} sec^{-1} above 100 MeV, and the delay between gamma-ray and optical emissions was found to be 12 hours.

Fermi-LAT is regularly monitoring this source since July 2008. An intense flare was observed from July 7 to Oct 6, 2008, and the average flux above 100 MeV was found to be 3×10^{-6} photons cm^{-2} sec^{-1}. Strong, distinct, and symmetric flares were observed with increase in flux by several factors within 3 days (Abdo et al. [105]).

A multi-wavelength study was carried out to find out the correlation between emissions in different wavelengths (IR, optical, UV, X-ray, and gamma-ray) from August to December of 2008 (Bonning et al. [106]). They found a correlation of less than a day between light curves in different frequencies except in X-rays. The X-ray flux is not correlated with fluxes in gamma-ray or longer wavelengths.

Similar result was also reported for the high state in 2009, November-December (Gaur et al. [107]). They found a strong correlation between optical and gamma-ray emission with a time lag of four days, but the X-ray emission is not correlated to any of them.

The strong flare of 3C 454.3 in 2009 during December 3-12 in gamma-rays, X-rays, and optical/near-infrared bands was studied by Gupta et al. [108]. Optical polarization measurements showed dramatic changes during flare with a strong anti-correlation between optical flux and degree of polarisation during the decay phase of the flare. They used one zone model with variations in the magnetic field, spectral break energies, and normalization to fit the spectral energy distributions at different times.

Raiteri et al. [109] studied the multi-wavelength light curves in 18 bands to analyze the flux variability for the period April 2008 to March 2010. The X-ray flux variation appeared to follow the gamma-ray and optical ones by about 0.5 and 1 day, respectively. They speculated that there is a slight variable misalignment between the synchrotron and Comptonisation zones, which can explain the increases in gamma-ray and X-ray flux levels in 2009-2010, and also the change in gamma-ray to optical flux ratio at the peaks of the outbursts.

During high gamma-ray states of 3C 454.3 in December 2009, April 2010, and November 2010, the parsec-scale jet was highly active. Superluminal radio knots K09 and K10 were found to be associated with autumn 2009 and 2010 outbursts (Jorstad et al. [110]). It was argued that gamma-ray outbursts of as short as 3 hours duration could occur on parsec scales if flares take place in localised regions such as turbulent cells.

Multi-wavelength variations of 3C 454.3 during the 2010 November to 2011 January outburst were studied before (Wehrle et al. [111]). Their discrete correlation analysis of the milli-meter, far-infrared, and gamma-ray light curves showed simultaneous variations indicating their common origin. They located the site of outbursts in parsec scale “core". In their model, the turbulent plasma crosses a conical shock in the parsec scale region of the jet. The seed photons for inverse Compton emission are produced in nonthermal radiation by a Mach disk, thermal emission from hot dust, or synchrotron emission from moving plasma. Extremely high polarisation in the 2010 outbursts was reported by Sasada et al. [112].

Long-term and rapid radio variability of 3C 454.3 was studied on the RATAN-600 radio telescope of the Special Astrophysical Observatory at 4.6, 8.2, 11.2 and 21.7 GHz and on the 32-m Zelenchuk, and Badary radio telescopes (Gorshkov et al. [113]). Two flares were observed in the long-term light curve in 2010 and in 2015-2017. The delay in the maximum of the first flare at 4.85 GHz relative to the maximum at 21.7 GHz was six months. Intraday variability was detected at 8.57 GHz on the 32-m telescopes in 30 of 61 successful observations, and it was found to be correlated with the maxima of the flares. The characteristic time scale for this variability was found to be two to ten hours.

Multi-wavelength temporal variability of 3C 454.3 for the high gamma-ray state during May to December 2014 was studied by Kushwaha et al. [114]. Their correlation study showed that no lag between infrared (IR) and gamma-ray, optical and gamma-ray, optical and IR, the source went to a state where gamma-ray lags the optical/IR by 3 days.

Fermi-LAT observations of the 2014 May-July outburst were studied by Britto et al. [115]. The average flux during the highest state from 7-29 June 2014 was found to be 7.2×10^{-6} photons cm^{-2} sec^{-1}. Several photons above 20 GeV were detected, including one above 45 GeV on MJD 56827. The emission region was speculated to be near the outer boundary of BLR. Temporal correlation between the optical, and gamma-ray flux variations in the blazar 3C 454.3 has been studied with 9 years of Fermi-LAT data (Rajput et al. [116]). Out of four epochs of intense optical flares, in two epochs, the gamma-ray and optical flares are found to be correlated. In the other two epochs, gamma-rays are weak or absent.

The long-term optical spectroscopic variations of blazar 3C 454.3 have recently been investigated with 10 years of data from the Steward Observatory (Nalewajko et al. [117]). The data revealed that the line flux from the broad-line region (BLR) changed dramatically with the blazar activity from a very high state in 2010 to a significantly low state in 2012. Inverse Compton emission of relativistic electrons by the seed photons from BLR is the well-established scenario for explaining gamma-ray emission from FSRQs. Due to this reason, the radius of the BLR is a crucial input parameter in modelling multi-wavelength emission from FSRQs. They have obtained the lower bound on the radius of the BLR to be 0.28 pc.

The long-term variability for the period between February 2008 and April 2016 in radio, IR, and optical bands has been analyzed recently by Sarkar [118]. This source showed significant multi-wavelength variability with the time scale of variability in the range of months to years. The variations in radio band have been observed to be lagging behind the variations in optical/IR bands by 15 to 100 days. A strong correlation in optical/IR bands indicates their co-spatial origin. They inferred from their analysis that the emission regions change their orientation with our line of sight as the time lag between radio and optical/IR emission varies over the years.

Recently, Weaver et al. [119] analyzed the uniquely structured multifrequency outburst of 2016 June. This outburst was monitored in optical R-band by several ground-based telescopes in photometric and polarimetric modes and also by the Fermi-LAT gamma-ray detector. Intra-day variability continued throughout the outburst. They constrained the Doppler factor and the size of the emission region from the observed minimum variability timescale.

Leptonic and lepto-hadronic models have been used previously to model the multi-wavelength spectral energy distributions. In MHD jet launching models a large scale poloidal magnetic field at the jet base extends to a helical magnetic field downstream along with the jet. A large-scale ordered helical magnetic field at a distance of hundreds of parsecs was used by Zamaninasab et al. [120] to explain the radio emission of 3C 454.3. Several theoretical models were proposed to explain the spectral energy distributions of 3C 454.3 (Finke and Dermer [121]; Cerruti et al. [122]; Hunger and Reimer [123]). The flare observed during Nov 2010 is well explained by one zone lepto-hadronic model by Diltz and Böttcher [124]. Another flare in August 2015 was observed with simultaneous data in optical, UV, X-ray, and gamma-ray energy (Shah et al. [125]). They suggested that X-ray, and gamma-ray emission of 3C 454.3 cannot be attributed to a single emission zone and both SSC (synchrotron self Compton) and EC (external Compton) mechanisms are required to explain the data. They further suggested that the flare region lies beyond this source's broad-line region (BLR).

Motivated by the earlier studies, we have analyzed the Fermi-LAT data from August 2008 to July 2017 to identify the flares of 3C 454.3 and study their characteristics. In section 3.2 we have discussed Fermi-LAT and Swift-XRT/UVOT data analysis. In section 3.3 the flaring states of 3C 454.3 are identified from the 9-year gamma-ray light curve. The flares are studied in section 3.4, their sub-structures and peaks are identified. The variability time in gamma-ray is calculated by scanning the light curves. The spectral energy distributions of the flares in gamma-rays are studied in section 3.5. In section 3.6 we have discussed about the multi-wavelength modelling of two flares. In section 3.7, we have discussed how time-dependent Doppler factor or injected luminosity in electrons can explain the flare peaks. Our results are discussed in section 3.8.

3.2 Data Analysis

3.2.1 Fermi-LAT Analysis

We have extracted the data of blazar 3C 454.3 source from FSSC's website data server[1] over the period of 9 years (August 2008 - July 2017) and analyzed it with the help of Fermi science tool software package version- 1.0.10, which includes galactic diffuse emission model (`gll_iem_v06.fits`) and extragalactic isotropic diffuse emission model (`iso_P8R2_SOURCE_V6_v06.txt`). We have followed further analysis procedure as described in section-2.1.1.

To generate the light curve, we have fixed the model parameters of all the sources within the ROI, excluding our source of interest from the third fermi catalog (3FGL; Acero et al. [126]). In our work, we have studied the light curve of three different time bins: 7-day, 1-day & 6-hour. Apart from this, we have also generated the spectral data points for different periods of activity in the energy range 0.1⩽E⩽300 GeV.

3.2.2 Swift-XRT/UVOT

We have analyzed the archival data from the Swift-XRT/UVOT for the source 3C 454.3 during the time period of April 2009 - April 2011 ($\sim$ 2 years.), which has been retrieved from HEASARC webpage[2]. Total 203 observations were made in this time span. The fixed neutral hydrogen column density of $n_H = 1.34 \times 10^{21} cm^{-2}$ (Villata et al. [127]) is used.

The source 3C 454.3 was also observed by the Swift Ultraviolet/Optical telescope (UVOT, Roming et al. [92]) in all the six filters: U, V, B, W1, M2, & W2. We have used these UVOT data in our multi-wavelength modelling.

[1]https://fermi.gsfc.nasa.gov/cgi-bin/ssc/LAT/LATDataQuery.cgi
[2]https://heasarc.gsfc.nasa.gov/cgi-bin/W3Browse/swift.pl

3.3 Flaring State of 3C 454.3

Seven-day binning gamma-ray light curve of 3C 454.3 has been shown in Figure-3.1, which is observed by Fermi-LAT from MJD 54686 (August 2008) to MJD 57959 (July 2017). From this 9-year light curve history, we have clearly identified (shown by the broken green line) five major flaring states and one quiescent state. As alluded to previously (Prince et al. [128]), we have defined these states as Flare-1, Flare-2, Flare-3, Flare-4, and Flare-5 with a time span from MJD 54683-54928, MJD 54928-55650, MJD 56744-57169, MJD 57169-57508, and MJD 57508-57933 respectively. The quiescent state has a time duration of almost about 3 years (MJD 55650-56744). In our work, we are more interested in flaring states, and hence further analysis has been carried out on these states only. We have studied these flares in detail for one-day binning (where the sub-structures are not clearly visible) and then six-hour binning to identify the various sub-structures properly.

In the 6-hour binning study, we have found several sub-structures for each flaring state. Flare-1 has only one sub-structure; we labeled that as Flare-1A. Four sub-structures were noticed in Flare-2 , defined as Flare-2A, Flare-2B, Flare-2C & Flare-2D respectively. Flare-3A and Flare-3B are two sub-structures of Flare-3. Similarly, Flare-4 and Flare-5 have four (Flare-4A, Flare-4B, Flare-4C & Flare-4D) and two (Flare-5A & Flare-5B) sub-structures respectively. There are two sub-substructures (Flare-1A & Flare-2A) that are well observed in one-day binning, but we cannot study them in 6 hr binning due to large error in the photon flux.

3.4 Gamma-ray light curve history of Flares & Variability

We have studied each substructure separately and observed different states of activity (e.g., pre-flare, flare, post-flare) as shown in the 6 hr binning light curve. There are various ways in which one can define the different states of the source. One of these methods

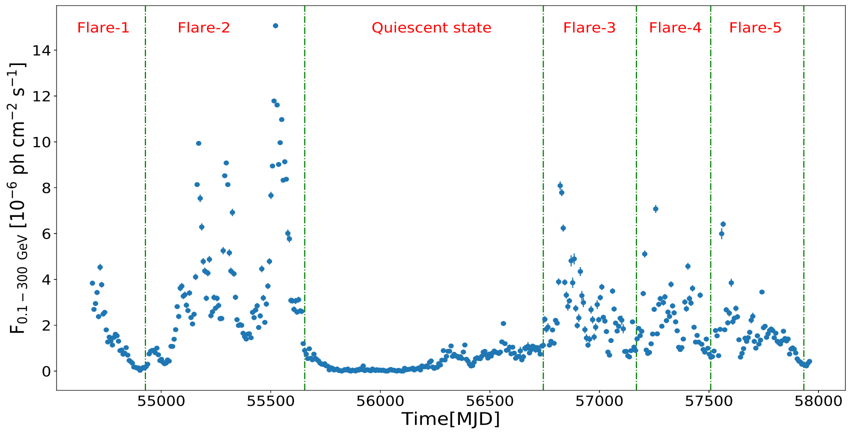

Figure 3.1: Seven-day binning light curve of 3C 454.3 (MJD 54686-57959). We have identified five major flares (shown by broken green line).

estimates the average flux for each time period (pre-flare, flare, etc.) and compares their values. The flare period can be defined as the period when the average flux is more than 3–4 times its average flux during the pre-flare period. The other way is to estimate the fractional variability in each period. The flux is high and more variable during the flaring period, while during pre-flare or post-flare the fractional variability is less, and, also the flux will be constant for a long period of time (e.g., Prince et al. [129]). In our case, we have used both these methods to identify the various states of the source, and our result is consistent with both these methods.

We have studied each sub-structure separately and observed different states of activity (Pre-flare, Flare, etc.) as shown in a 6-hour binning light curve. We have fitted only the flaring state of each sub-structure with the sum of an exponential function to show the temporal evolution. These fitted flares have characteristic rising and decay times for different peaks (P1, P2, etc.). The functional form of the sum of an exponential function is given by Abdo et al. [130]

$$F(t) = 2\sum_{i=1}^{n} F_{0,i}[\exp(\frac{t_{0,i}-t}{T_r}) + \exp(\frac{t-t_{0,i}}{T_d})]^{-1} \tag{3.1}$$

where t_0 is the peak time, and F_0 is the flux observed at time t_0. T_r and T_d represent the rising and decay time, respectively. n is the total number of major peaks. For few flares, we are able to show the constant state (shown by horizontal grey line). All reported gamma-ray fluxes throughout this chapter are mentioned in a unit of 10^{-6} ph cm^{-2} s^{-1}.

3.4.1 Flare-1

A 6 hour binning has been carried out for Flare-1 during MJD 54683-54928. We have found only one sub-structure (defined as Flare-1A) in this period. But we cannot identify the peaks in this binning due to rapid fluctuation and large error in photon counts. For this reason, we have shown the sub-structure in 1-day binning in Figure-3.2.

Flare-1A (MJD 54712-54783) has two distinct states of activity, and these are defined as Flare and Post-flare. There are several peaks in the Flare epoch (shown in Figure-3.3), but we have considered only three prominent major peaks, which are labeled as P1, P2 & P3 with the fluxes of 5.45±0.42, 4.31±0.35 & 3.66±0.28 at time MJD 54719.1, 54729.1 and 54738.1 respectively. The details of the modelling parameters (T_r & T_d) have been elucidated in Table-3.1. Post-flare epoch (MJD 54759 - 54783) follows immediately after Flare epoch with a time span of 24 days, which has small variations in flux, and the average flux is found to be 1.27±0.04.

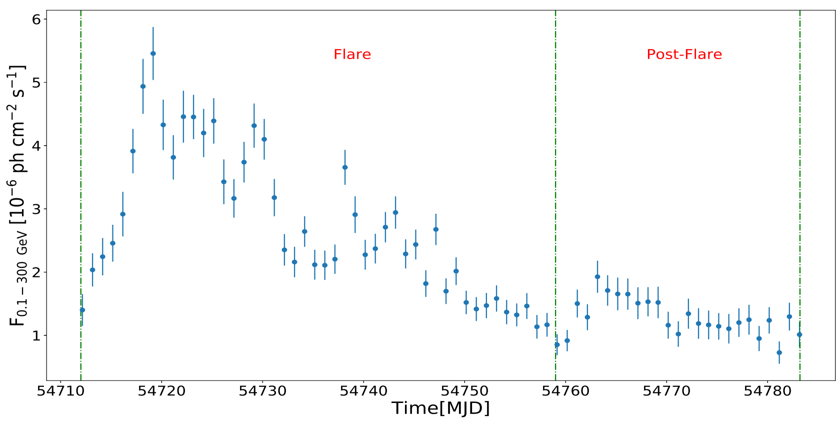

Figure 3.2: One day binning light curve for Flare-1A. Time durations of all the different periods of activities (shown by broken green line) are: MJD 54712-54759 (Flare), MJD 54759-54783 (Post-Flare).

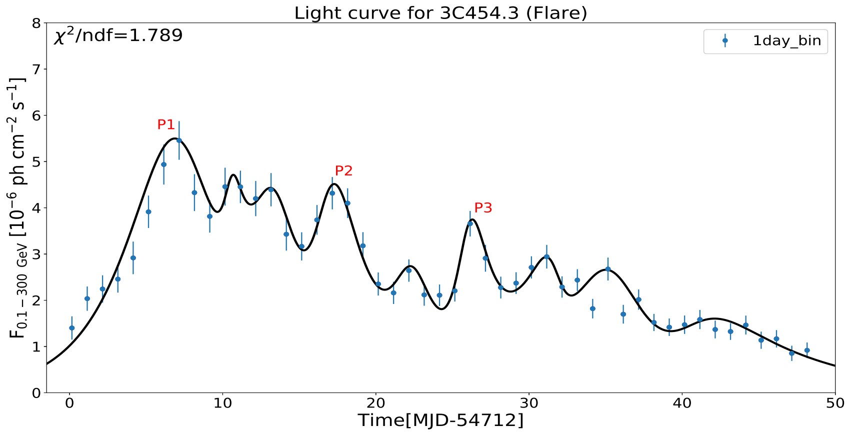

Figure 3.3: Fitted light curve (fitted by the sum of exponential function) of Flare-1A of Flare (MJD 54712-54759) epoch.

3.4.2 Flare-2

We have performed a 6-hour binning of the light curve of Flare-2 during MJD 54928-55650 and identified four sub-structures (Flare-2A, Flare-2B, Flare-2C & Flare-2D). As Flare-1A, we are unable to study the temporal evolution of Flare-2A in 6 hour binning due to significant error in flux. Here one day binning light curve of Flare-2A are considered for

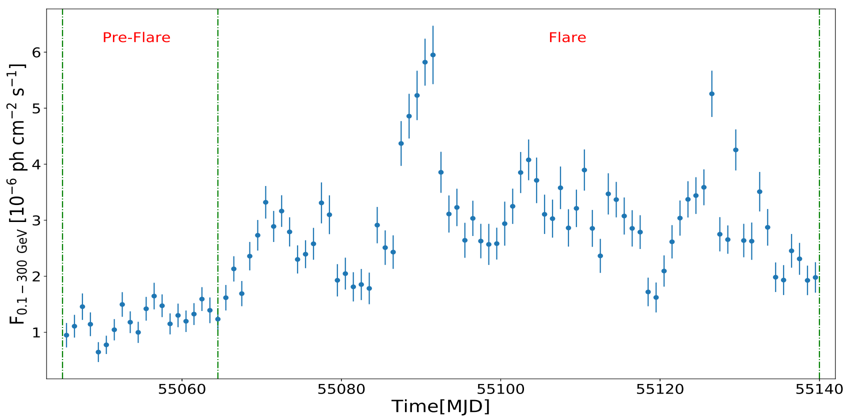

Figure 3.4: One day binning light curve for Flare-2A. Time durations of all the different periods of activities (shown by broken green line) are: MJD 55045-55064 (Pre-Flare), MJD 55064-55140 (Flare).

further study which is shown in Figure-3.4. The six hour binning light curve of Flare-2B, Flare-2C & Flare-2D are presented in Figure-3.6, Figure-3.9 and Figure-3.12 respectively.

Flare-2A shows two different phases during MJD 55045 - 55140, which are labeled as Pre-flare and Flare. The pre-flare epoch has a time span of 19 days (MJD 55045 - 55064) with an average flux of 1.22±0.04. After that source enters into flaring state with a time duration of MJD 55064 - 55140. Figure-3.5 shows the fitted light curve of a flaring state in 1 day binning, which has four prominent peaks (P1, P2, P3 & P4) with fluxes of 3.32±0.29, 3.31±0.36, 5.95±0.52, 4.08±0.36 at MJD 55070.5, 55077.5, 55091.5 and 55103.5 respectively. The details of the parameters have been described in Table-3.2.

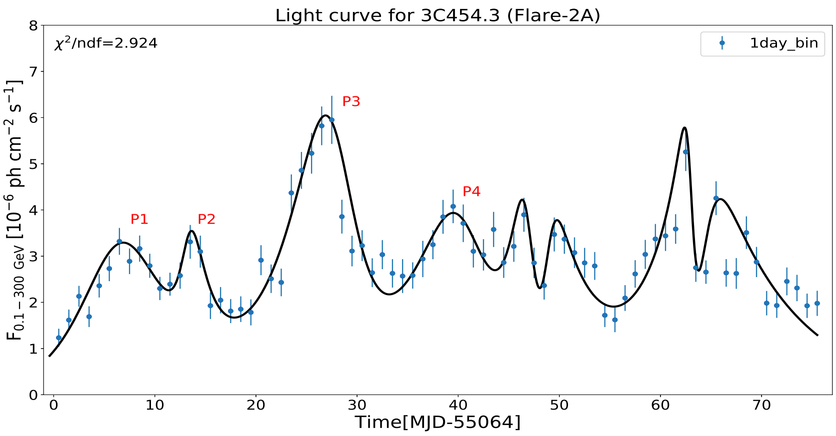

Figure 3.5: Fitted light curve (fitted by the sum of exponential function) of Flare-2A of Flare (MJD 55064-55140) epoch.

Flare-2B (MJD 55140-55201) also shows two different states of activity regions: Pre-flare and Flare. Pre-flare has been considered from MJD 55140-55152, during which flux does not vary much. The rest of the region of the light curve is considered as Flare (MJD 55152-55201). Figure-3.7 and Figure-3.8 represent the fitted light curve of the Flaring state in two different parts, as we are unable to fit the entire Flare in a single plot. In the 1st part of the Flare (Figure-3.7, MJD 55152-55177), six major peaks (P1, P2, P3, P4, P5 and P6) are observed at MJD 55154.9, 55163.1, 55165.1 55167.9, 55170.4, 55172.1 with fluxes(F_0) of 7.48±1.24, 9.69±1.41, 9.69±0.99, 22.86±1.48, 18.70±1.24 and 14.56±1.21

respectively. A small hump kind of structure has been observed at the beginning of the light curve during MJD 55152.0-55153.9 (Figure-3.7), but we have not considered it as a distinct peak due to low flux value. Similarly, five different peaks (P1, P2, P3, P4, and

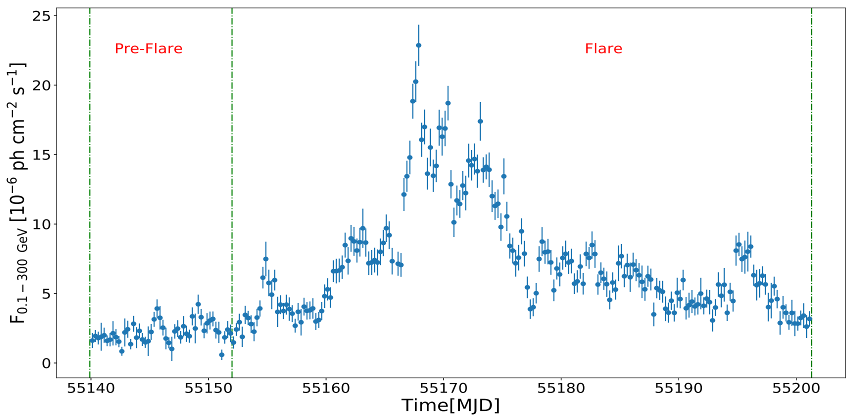

Figure 3.6: Six-hour binning light curve for Flare-2B. Time durations of all the different periods of activities (shown by broken green line) are: MJD 55140-55152 (Pre-flare), MJD 55152-55201 (Flare).

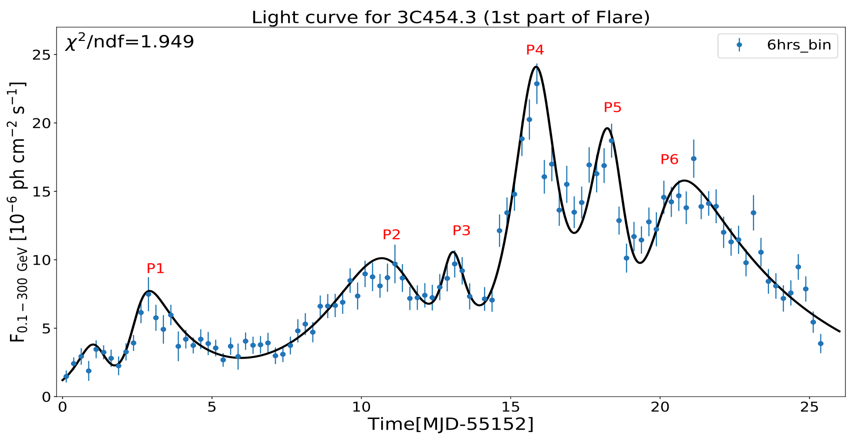

Figure 3.7: Fitted light curve (fitted by the sum of exponential function) of Flare-2B for 1st part of Flare (MJD 55152-55177) epoch.

P5) have been noticed in the 2nd part of Flare (Figure-3.8, MJD 55177-55201). The Flux values (F_0) of these peaks are: 8.73±1.04, 7.85±0.95, 8.48±0.98, 7.68±0.87 and 8.52±0.83 at MJD 55178.4, 55180.4, 55182.6, 55185.1 and 55195.1 respectively. The values of the fitted parameters are given in Table-3.3.

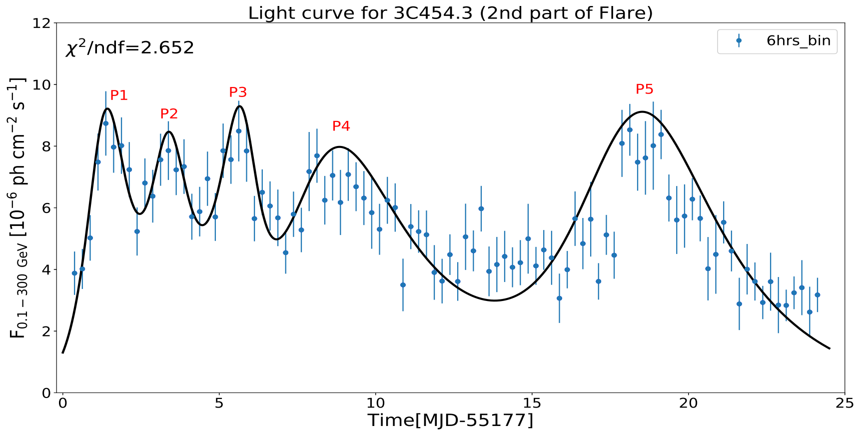

Figure 3.8: Fitted light curve (fitted by the sum of exponential function) of Flare-2B for 2nd part of Flare (MJD 55177-55201) epoch.

There are four different phases of activity (Pre-flare, Flare-I, Flare-II, and Post-flare) in Flare-2C during MJD 55250-55356, which are shown in Figure-3.9. The pre-flare phase has a small variation in counts with an average flux of 2.68±0.06, and then the source goes to Flare-I and Flare-II state with the time span of 36 days & 18 days, respectively. The fitted light curve of the Flare-I phase (shown in Figure-3.10) shows five distinguishable major peaks, which are labeled as P1, P2, P3, P4 & P5, respectively.

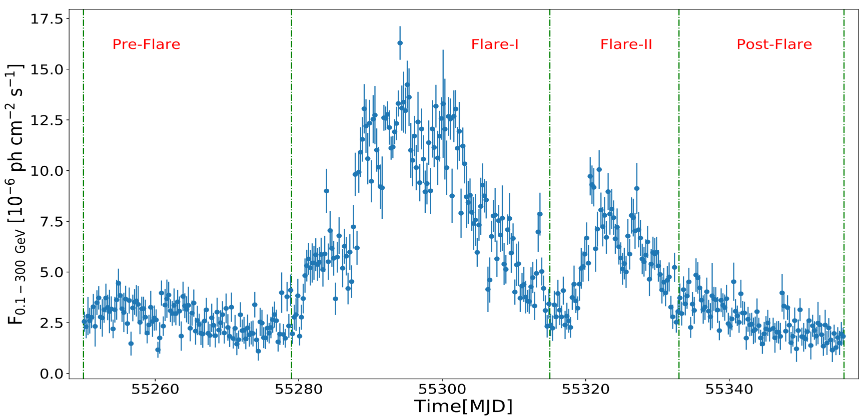

Figure 3.9: Six-hour binning light curve for Flare-2C. Time durations of all the different periods of activities (shown by broken green line) are: MJD 55250-55279 (Pre-flare), MJD 55279-55315 (Flare-I),MJD 55315-55333 (Flare-II) and MJD 55333-55356 (Post-flare).

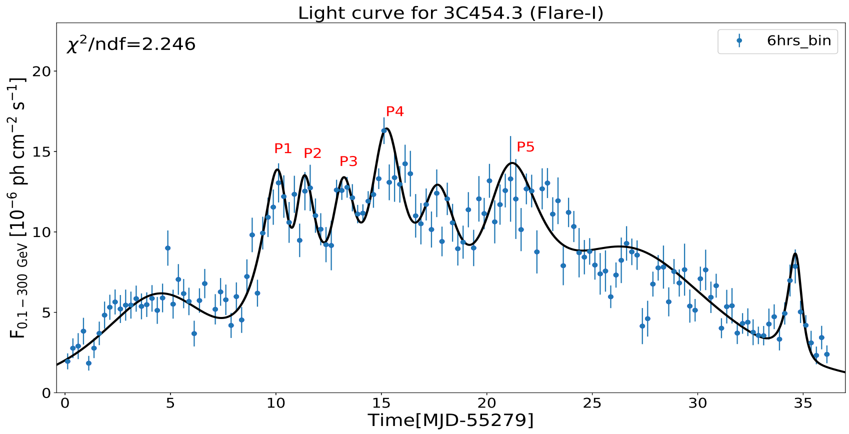

Figure 3.10: Fitted light curve (fitted by the sum of exponential function) of Flare-2C for Flare-I (MJD 55279-55315) epoch.

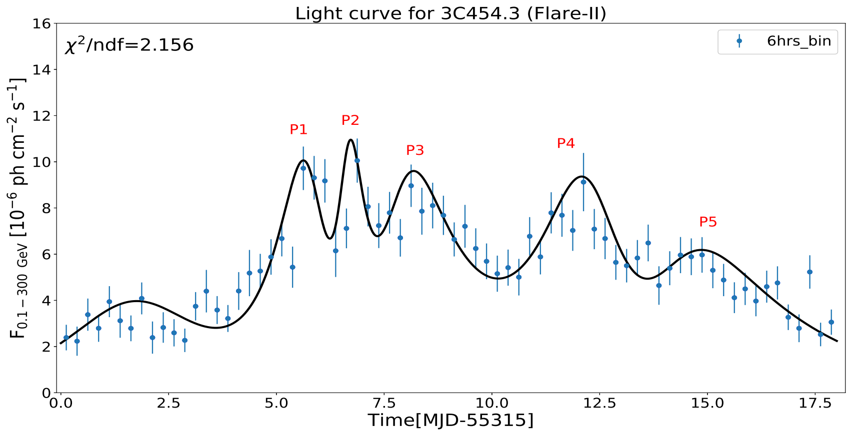

Figure 3.11: Fitted light curve (fitted by the sum of exponential function) of Flare-2C for Flare-II (MJD 55315-55333) epoch.

After peak P5 flux counts gradually decrease with small variation, and at the end of Flare-I epoch (During MJD 55312.2-55314.7), a sudden increase in flux has been observed, although we have not considered it as a distinct peak since it is far away from the main peaks. Flare-II (shown in Figure-3.11) phase also shows 5 distinctive major peaks (defined as P1, P2, P3, P4 & P5) with fluxes of 9.71±0.94, 10.05±0.95, 7.79±0.90, 9.12±1.26 and 5.96±0.78 at MJD 55320.6, 55321.6, 55322.6, 55327.1 & 55329.4 respectively. After Flare-II, photon flux starts to decay slowly, and the source comes back to its quiescent state, which we have identified as the Post-flare phase in Figure-3.9. The detailed description of the modelling parameters have been elucidated in Table-3.4.

Flare-2D (MJD 55467-55600) is observed to be the most violent sub-structure in the whole 9-years of light curve history with six different phases (shown in Figure-3.12) of activity: Pre-flare, Plateau-I, Flare-I, Flare-II, Plateau-II, and Post-flare. There is no rapid fluctuation in flux during MJD 55467-55480. This phase is considered as the Pre-flare phase. After that (MJD 55467), the flux starts to rise slowly up to MJD 55511, which

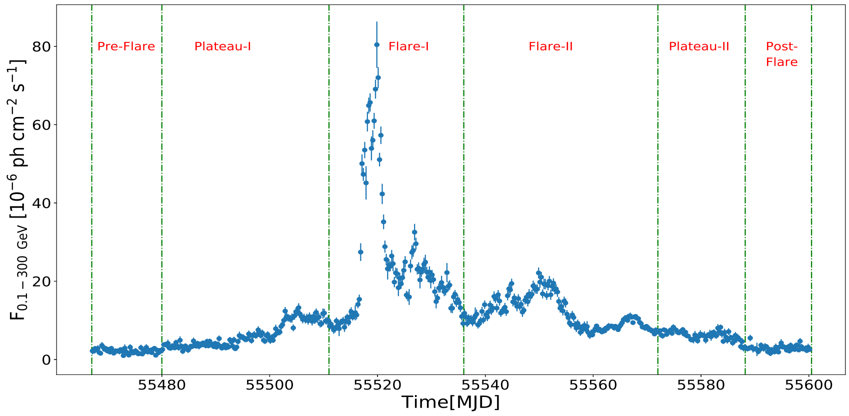

Figure 3.12: Six-hour binning light curve for Flare-2D. Time durations of all the different periods of activities (shown by broken green line) are: MJD 55467-55480 (Pre-flare), MJD 55480-55511 (Plateau-I), MJD 55511-55536 (Flare-I) and MJD 55536-55572 (Flare-II), 55572-55588 (Plateau-II), 55590-55600 (Post-flare).

is labeled as the Plateau-I phase, with an average flux of 6.26±0.07. We have identified three major peaks (P1, P2, P3) from the fitted light curve (see Figure-3.13) of Flare-I phase with a time duration of 25 days, which has peak fluxes(F_0) 53.51±2.08, 65.66±2.34, 80.41±5.92 at MJD 55517.6, 55518.6 and 55519.9 respectively. Peak P3 corresponds to the highest observed flux in our analysis. A small variation compared to peaks P1, P2, and P3 has been noticed in flux after peak P3 in the Flare-I phase, but no major peak has been identified. Flare-II state is observed immediately after Flare-I during MJD 55536 - 55572. Significant variation in flux is seen during this period, and six major peaks are observed (see Figure-3.14). After Flare-II (see Figure-3.12.), the source went into a state of steady diminution of flux defined as Plateau-II, which eventually ends up into a Post-flare state having almost constant temporal flux distribution. The details of the values of the parameter are displayed in Table-3.5.

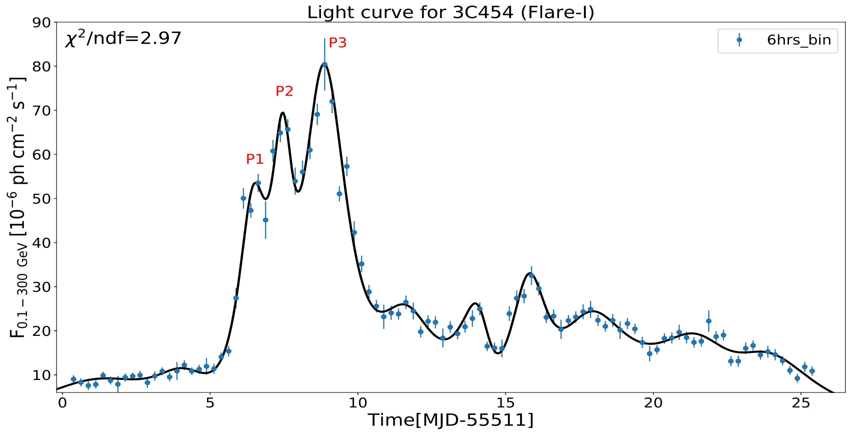

Figure 3.13: Fitted light curve (fitted by the sum of exponential function) of Flare-2D for Flare-I (MJD 55511-55536) epoch.

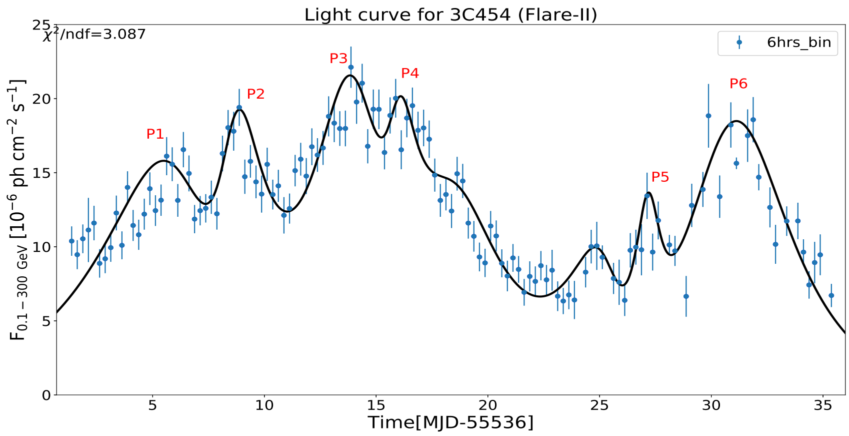

Figure 3.14: Fitted light curve (fitted by the sum of exponential function) of Flare-2D for Flare-II (MJD 55536-55572) epoch.

3.4.3 Flare-3

Following the similar procedure executed for Flare-2, a 6-hour binning light curve analysis has also been carried out for Flare-3 and two sub-structures (Flare-3A, and Flare-3B) of moderate time duration (51, & 30 days respectively) have been found in our study.

Four different epochs of flaring phases are identified in Flare-3A (shown in Figure-

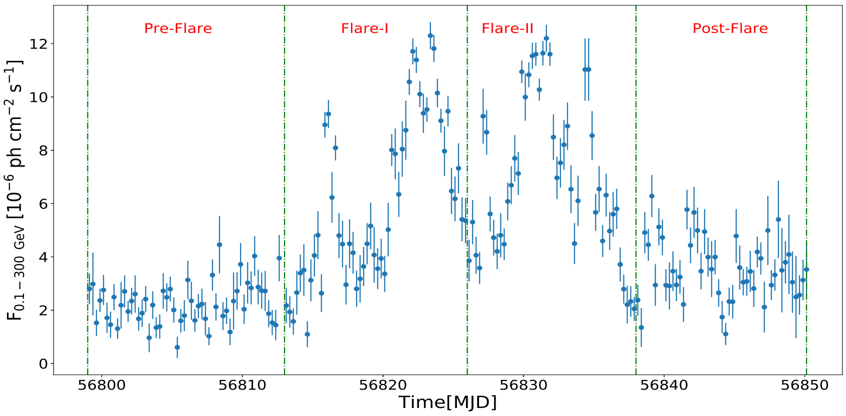

Figure 3.15: Six-hour binning light curve for Flare-3A. Time durations of all the different periods of activities (shown by broken green line) are: MJD 56799-56813 (Pre-flare), MJD 56813-56826 (Flare-I), MJD 56826-56838 (Flare-II) and MJD 56838-56850 (Post-flare).

3.15). The time span of pre-flare is about 14 days. After the pre-flare, two flaring states (Flare-I and Flare-II) of similar time durations have been identified, both of which have five prominent peaks are shown in Figure-3.16 and Figure-3.17 respectively.

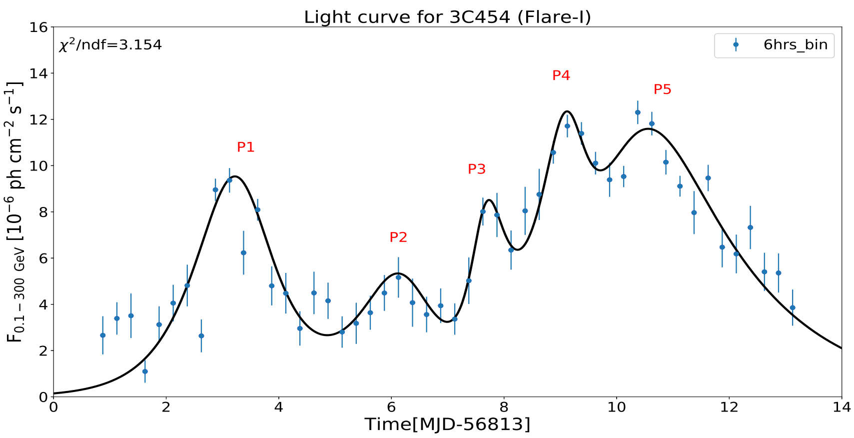

Figure 3.16: Fitted light curve (fitted by the sum of exponential function) of Flare-3A for Flare-I (MJD 56813-56826) epoch.

The values of the modelling parameters for these state has been elucidated in Table-3.6. Small fluctuations in photon flux are noticed during MJD 56838-56850 with the average flux of 3.56±0.12, which is defined as the post-flare phase (Figure-3.15).

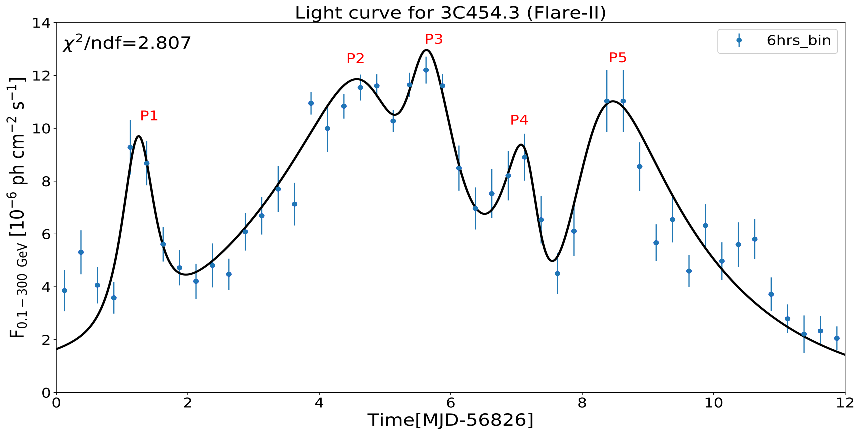

Figure 3.17: Fitted light curve (fitted by the sum of exponential function) of Flare-3A for Flare-II (MJD 56826-56838) epoch.

Flare-3B has the least complicated substructure with three clear states shown in Figure-3.18. A pre-flare phase has been identified from MJD 56799 - 57002. In the Flare region, the source shows only two significant peaks at MJD 57006.1, 57008.4 with fluxes of 4.95±0.69 and 7.90±0.90 respectively (Figure-3.19).

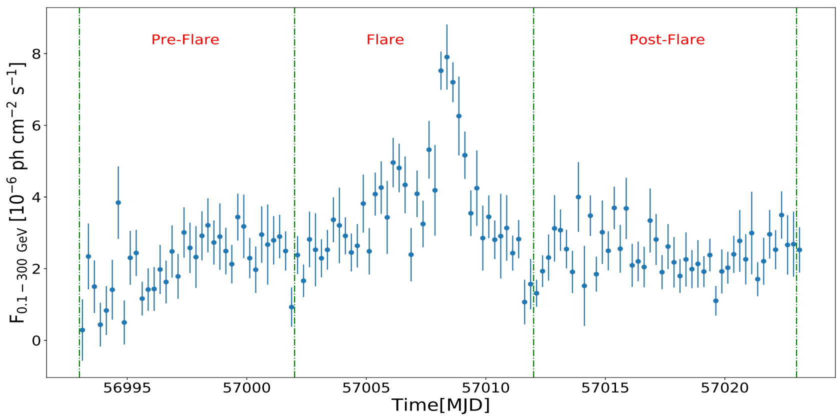

Figure 3.18: Six-hour binning light curve for Flare-3B. Time durations of all the different periods of activities (shown by broken green line) are: MJD 56993-57002 (Pre-flare), MJD 57002-57012 (Flare) and MJD 57012-57023 (Post-flare).

After spending around 10 days in flaring state, it comes back again to the constant flux state, which is labeled as Post-flare. The values of the fitted parameters have been

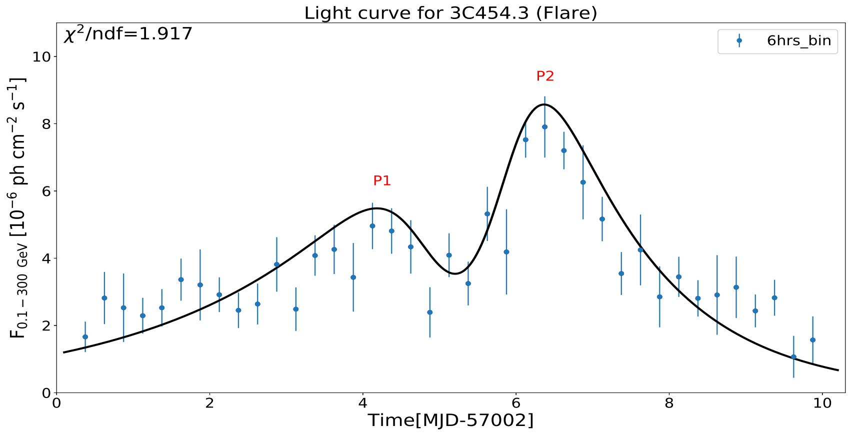

Figure 3.19: Fitted light curve (fitted by the sum of exponential function) of Flare-3B for Flare (MJD 57002-57012) epoch.

displayed in Table-3.7.

3.4.4 Flare-4

Six hour binning of the light curve of Flare-4 shows four distinct sub-structures, defined as Flare-4A, Flare-4B, Flare-4C and Flare-4D (Figure-3.20, Figure-3.22, Figure-3.24 and Figure-3.26). In this period, we are able to fit the light curve by showing the constant

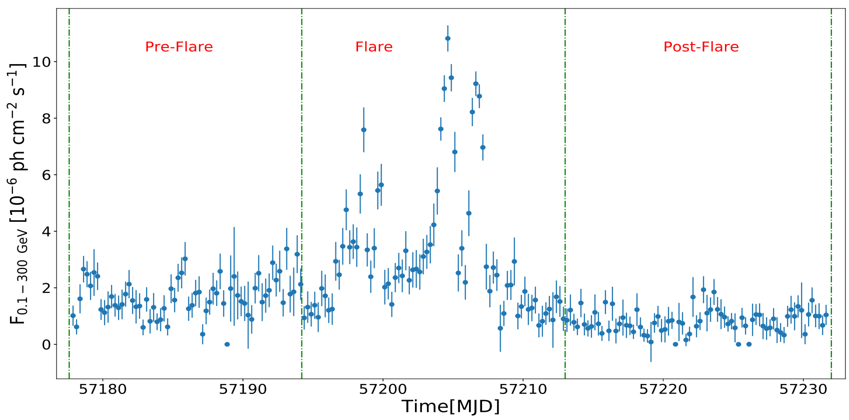

Figure 3.20: Six-hour binning light curve for Flare-4A. Time durations of all the different periods of activities (shown by broken green line)are: MJD 57178-57194 (Pre-flare),MJD 57194-57213 (Flare) and MJD 57213-57232 (Post-flare).

flux state (shown by horizontal grey line) for Flare-4A, Flare-4B and Flare-4D, which are shown in Figure-3.21, Figure-3.23 and Figure-3.27 respectively.

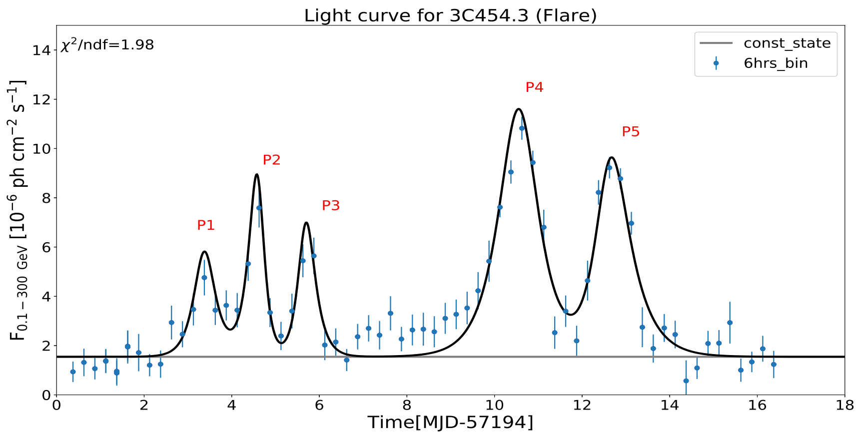

Figure 3.21: Fitted light curve (fitted by the sum of exponential function) of Flare-4A for Flare (MJD 57194-57213) epoch.

A Pre-flare phase has been noticed in Flare-4A during MJD 57178 to MJD 57194 with small-scale variation in photon flux and the average flux is observed to be 1.57±0.08. After that, the source enters into the Flaring state (shown in Figure-3.21) with time span of 19 days (MJD 57194 - 57213), which has 5 well defined peaks (labeled as P1, P2, P3, P4 and P5). The values of the peak fluxes (F_0) at time t_0 and the fitted parameters have been given in Table-3.8. The Post-flare region promptly follows after this with a duration of 19 days and having an almost constant flux throughout this period.

Similarly, Flare-4B also shows three phases (see Figure-3.22): Pre-flare, Flare and Post-flare.Pre-flare and Post-flare epochs have almost constant flux with the average fluxes of 2.50±0.12 and 1.91±0.10, respectively. Two distinct major peaks (P1, and P2) are observed during the Flare phase (see Figure-3.23), which have peak fluxes of 11.43±0.48 and 12.00±0.49 at MJD 57254.1 & 57256.1 respectively. The details of the fitted parameters are given in Table-3.9.

Flare-4C (Figure-3.24) has much more error in flux compared to other sub-structures, and three different phases (pre-flare, flare, and post-flare) are observed.

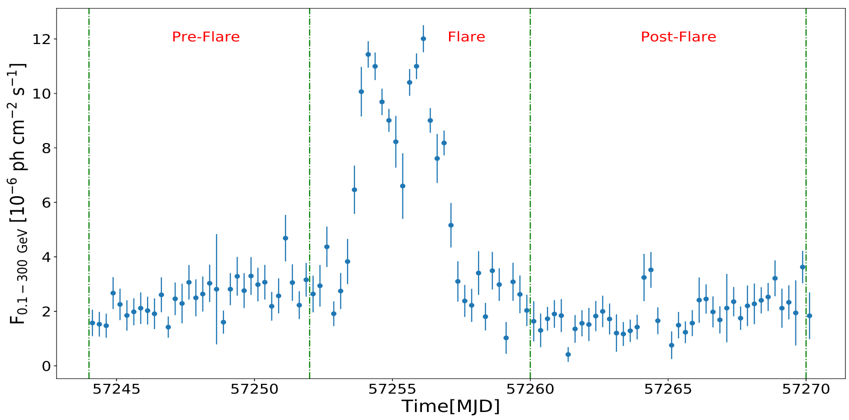

Figure 3.22: Six-hour binning light curve for Flare-4B. Time durations of all the different periods of activities (shown by broken green line) are: MJD 57244-57252 (Pre-flare), MJD 57251-57260 (Flare) and MJD 57260-57270 (Post-flare).

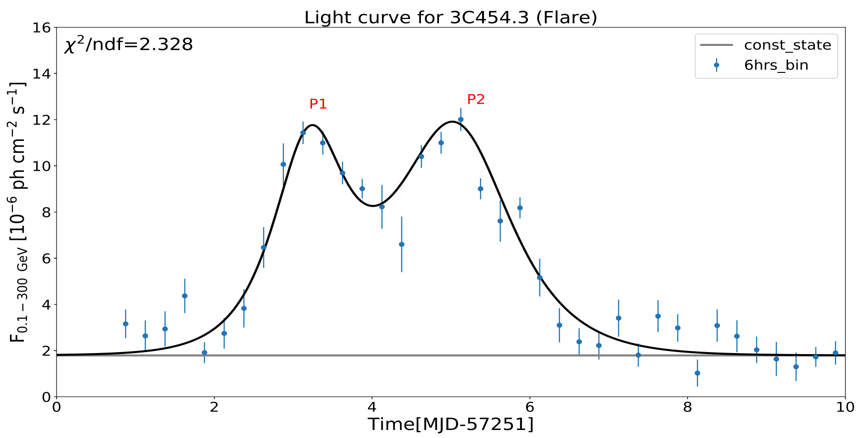

Figure 3.23: Fitted light curve (fitted by the sum of exponential function) of Flare-4B for Flare (MJD 57251-57260) epoch.

Pre-flare and Post-flare states have a time span of 8 days and 11 days before and after the flare phase, respectively. During the flare phase 4, major peaks have been clearly identified with fluxes of 5.15±0.83, 5.49±0.80, 7.44±0.94 & 5.44±0.83 at MJD 57401.4, 57402.9, 57407.1 and 57408.9 respectively, which are shown in Figure-3.25. The values of the fitted parameters are given in Table-3.10.

Flare-4D (shown in Figure-3.26) has three phases similar to Flare-4A & Flare-4B. The Pre-flare phase shows a small variation in the flux, and the average flux is observed

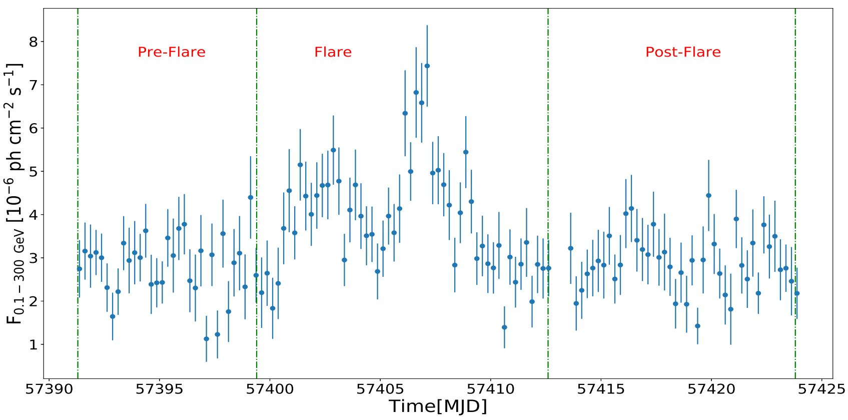

Figure 3.24: Six-hour binning light curve for Flare-4C. Time durations of all the different periods of activities (shown by broken green line) are: MJD 57391-57399 (Pre-flare), MJD 57399-57413 (Flare) and MJD 57413-57424 (Post-flare).

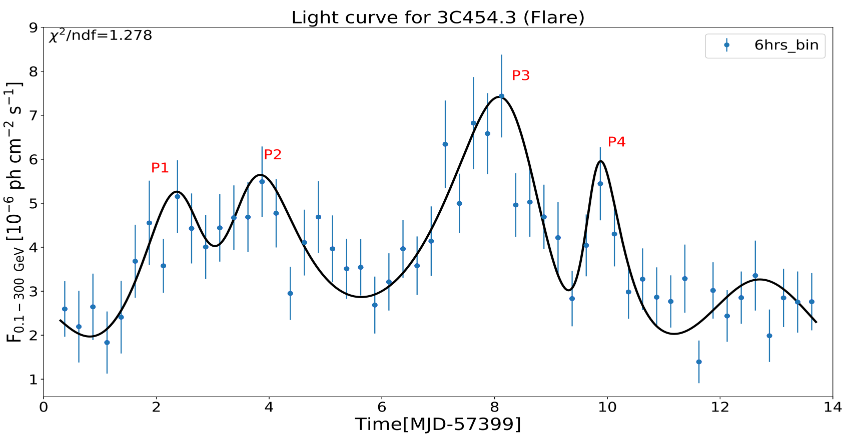

Figure 3.25: Fitted light curve (fitted by the sum of exponential function) of Flare-4C for Flare (MJD 57399-57413) epoch.

to be 1.31±0.11, which lasts from MJD 57450-57456. The Flare phase has two sharp peaks labeled as P1 & P2 with fluxes of 3.49±0.69, 9.99±0.45 at MJD 57457.4 & 57460.1 respectively, which are shown in Figure-3.27. We have identified the Post-flare region during MJD 57461-57468. Table-3.11 displays the values of the fitted parameters.

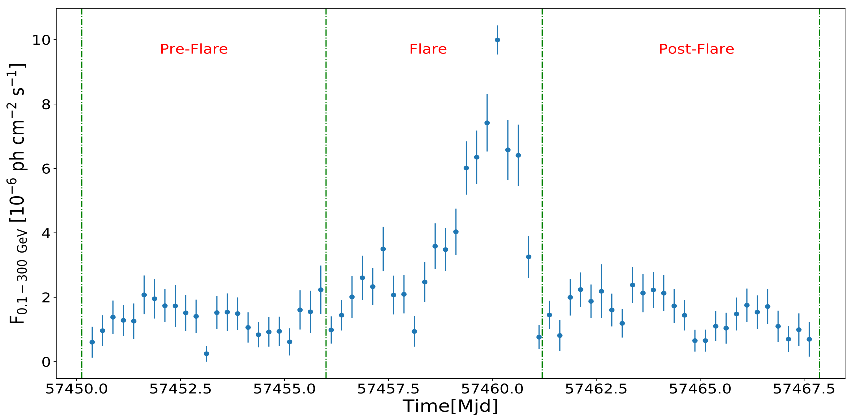

Figure 3.26: Six-hour binning light curve for Flare-4D. Time durations of all the different periods of activities (shown by broken green line)are: MJD 57450-57456 (Pre-flare), MJD 57454-57461 (Flare) and MJD 57461-57468 (Post-flare).

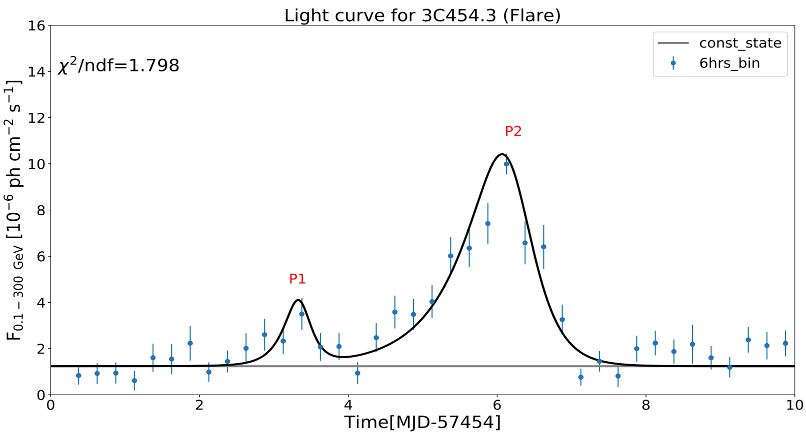

Figure 3.27: Fitted light curve (fitted by the sum of exponential function) of Flare-4D for Flare (MJD 57454-57461) epoch.

3.4.5 Flare-5

Similarly, a 6 hour binning of Flare-5 has also been carried out, and two sub-structures have been found. One during June-July, 2016 (MJD 57542 - 57576) and another in December 2016 (MJD 57727 - 57752) with time span of 34 days and 25 days, respectively. Both the sub-structures (defined as Flare-5A and Flare-5B) have the simplest time profile, where the three phases Pre-flare, Flare & Post-flare can be clearly identified.

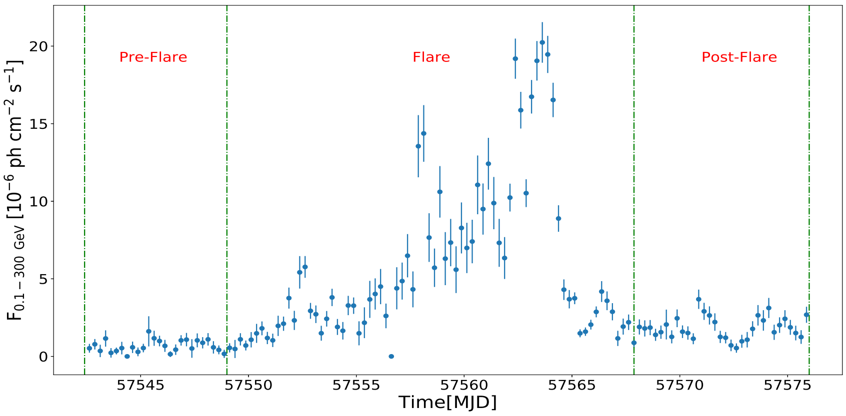

Figure 3.28: Six-hour binning light curve for Flare-5A. Time durations of all the different periods of activities (shown by broken green line) are: MJD 57542-57549 (Pre-flare), MJD 57549-57568 (Flare) and MJD 57568-57576 (Post-flare).

The Pre-flare phase of Flare-5A has almost constant flux during MJD 57542-57549 (see Figure-3.28). Figure-3.29 shows the fitted light curve of the Flare phase with a time duration (MJD 57549 - 57568) of 19 days, and five major peaks have been identified. A slight fluctuation is noticed in flux during the Post-flare phase (MJD 57568 - 57576), and the average flux is estimated to be 1.84±0.09. The values of the modelling parameters have been given in Table-3.12. Figure-3.30 shows the three different states of Flare-5B.

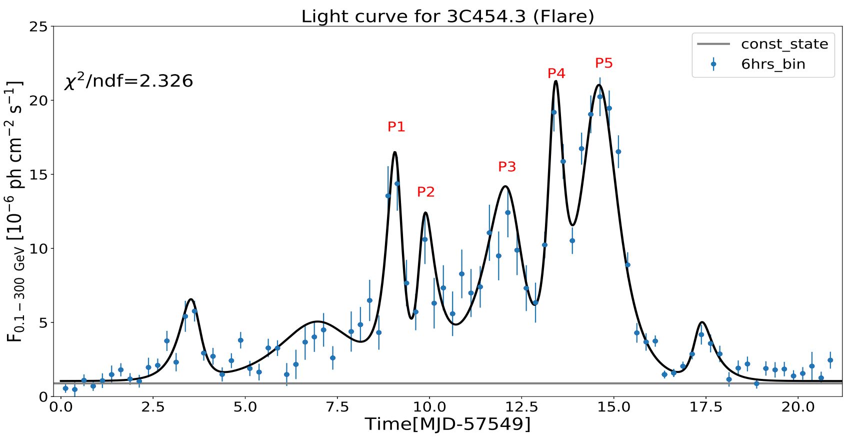

Figure 3.29: Fitted light curve (fitted by the sum of exponential function) of Flare-5A for Flare (MJD 57549-57568) epoch.

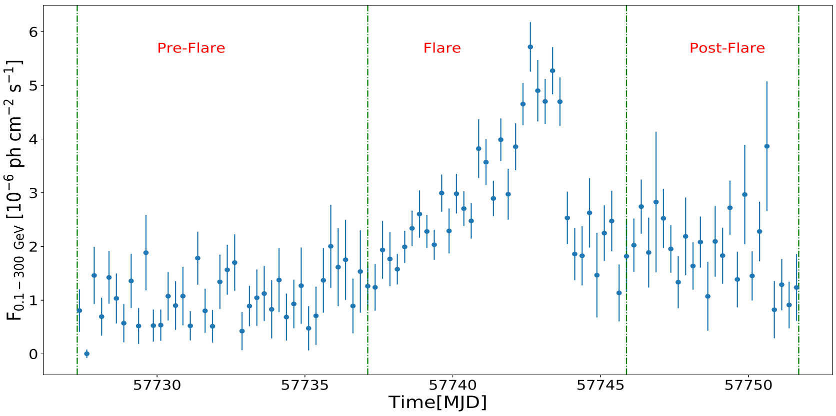

Figure 3.30: Six-hour binning light curve for Flare-5B.Time durations of all the different periods of activities (shown by broken green line)are: MJD 57727-57737 (Pre-flare),MJD 57737-57746 (Flare) and MJD 57746-57752 (Post-flare).

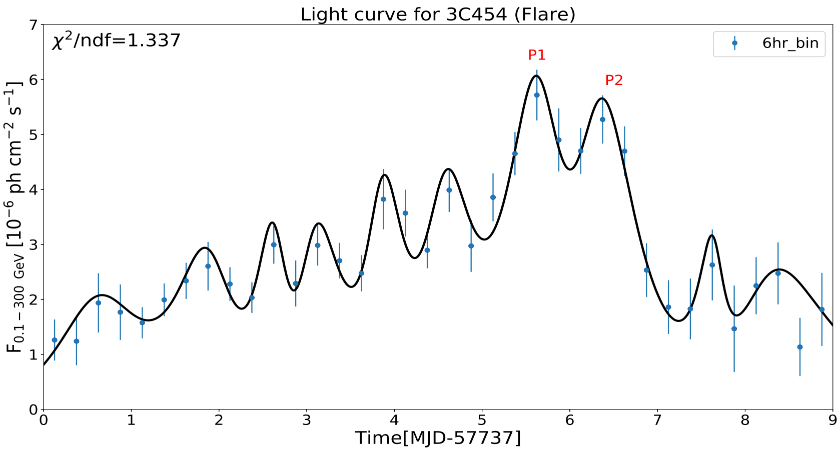

Figure 3.31: Fitted light curve (fitted by the sum of exponential function) of Flare-5B for Flare (MJD 57737-57746) epoch.

The Pre-flare phase of Flare-5B (shown in Figure-3.30) has been considered during MJD 57727-57737. After that, a Flare with two distinct major peaks has been identified, shown in Figure-3.31. Small variation in flux has been noticed in the flare phase during MJD 57737.1 to MJD 57741.9, which is also fitted with the sum of an exponential function (equation 3.1). However, we have not considered any peak in this time interval due to the low count of photons. The Post-flare region has a time duration of around six days with an average flux of 1.96±0.14. The fitted parameters values have been described in Table-3.13.

Constant flux value in the steady-state (shown by constant grey line) for Flare-4A, Flare-4B, Flare-4D, and Flare-5A have been shown in Table-3.14.

3.4.6 Variability study

Variability time (t_{var}) is the timescale of variation in flux during flare. This can be computed by scanning the 6 hours binned γ-ray light curve with the following equation -

$$F(t_2) = F(t_1) 2^{\frac{(t_2 - t_1)}{\tau_{d/h}}} \tag{3.2}$$

where, $F(t_1)$ & $F(t_2)$ are the fluxes at consecutive time instants t_1 & t_2 respectively. Doubling/Halving (indicated by '+' & '−' sign respectively) timescale is indicated by $\tau_{d/h}$. We have used the following two criteria while scanning the light curve (Prince et al. [128]). They are:

- Flux should be half or double between two successive instants of time.
- The condition TS > 25 (corresponds to $\sim 5\sigma$ detection) on flux must always be fulfilled for these two consecutive time instants.

The value of $\tau_{d/h}$ for each sub-structure has been shown in Table-3.15 - Table-3.17. The minimum value of $|\ \tau_{d/h}\ |$ is defined as the variability time (t_{var}) in our work.

In our 9-year light curve study we have found the shortest time as $\tau_{d/h}$ (or t_{var}) = 1.70 ± 0.38 hour during MJD 56815.625-56815.875 (Flare-3A), which is consistent with previously calculated hour scale variability time for other FSRQs e.g. PKS 1510-089 and CTA 102 (Prince et al. [128], Prince et al. [129]).

3.5 Gamma-ray spectral energy distribution (SED)

We have fitted the SEDs of different epochs with three different spectral models (Abdo et al. [131]). These are

1. A powerlaw model(PL), whose functional form is

$$\frac{dN}{dE} = N_0(\frac{E}{E_0})^{-\Gamma} \tag{3.3}$$

   where, N_0 and Γ are the prefactor & spectral index respectively. We have kept fixed the value of E_0 (Scaling factor) to 100 MeV for all the SEDs.

2. A log parabola model(LP), whose functional form is

$$\frac{dN}{dE} = N_0(\frac{E}{E_0})^{-(\alpha+\beta\log(E/E_0))} \tag{3.4}$$

   where, α & β are the photon index & curvature index respectively. Scaling factor (E_0) is kept fixed to 300 MeV, near the low energy part of the spectrum("ln" is the natural logarithm).

3. A broken-powerlaw model(BPL), whose functional form is

$$\frac{dN}{dE} = N_0 \begin{cases} (\frac{E}{E_b})^{-\Gamma_1}, & \text{for } E < E_b \\ (\frac{E}{E_b})^{-\Gamma_2}, & \text{otherwise} \end{cases} \tag{3.5}$$

   where E_b is the break energy.

The values of the fitted parameters for these spectral models (PL, LP & BPL) have been elucidated in Table-3.18 - Table-3.30. We have also mentioned the $\log(\mathcal{L})$ value for all the epochs and calculated $\Delta\log(\mathcal{L})$ value from that, which is defined by the difference between the $\log(\mathcal{L})$ value for logparabola/broken-powerlaw model and simple powerlaw model.

$$\Delta log(\mathcal{L}) = |log(\mathcal{L})_{LP/BPL}| - |log(\mathcal{L})_{PL}| \tag{3.6}$$

Figure-3.32 shows the SEDs of the sub-structure of Flare-1A for two different phases: Flare & Post-flare. Here cyan, black & magenta color indicate the fitting of spectral points with the Power-law (PL), Log-parabola (LP), and Broken-power law model (BPL), respectively. The values of the fitted parameters for the different periods of activity for these models (PL, LP, BPL) have been given in Table-3.18.

The SEDs of the flaring epochs for all the three sub-structures (Flare-2A, Flare-2B, Flare-2C & Flare-2D) of Flare-2 have been illustrated in Figure-3.33, Figure-3.34, Figure-3.35 and Figure-3.36 respectively. All of these sub-structure except Flare-2A show the spectral hardening with increasing flux. Spectral index (Γ) is nearly constant (for PL model) with changing flux in Flare-2A (shown in Table-3.18). For Flare-2D, in Pre-flare phase index Γ=2.41$\pm$0.01, then it changes to 2.33$\pm$0.01 for Plateau-I phase, to 2.27$\pm$0.00 and 2.29$\pm$0.00 for Flare-I & Flare-II phases respectively, which have been described in Table-3.21. The values of the fitted parameters for Flare-2B and Flare-2C have been displayed in Table-3.19 & Table-3.20 respectively.

A significant spectral hardening is observed during Flare-3A when the source transits from Pre-flare to Flare-I & Flare-II phase, whereas during Flare-3B, the spectral hardening is not much significant. The SEDs of these substructures have been shown in Figure-3.37 and Figure-3.38 and the corresponding values of the parameters have been given in Table-3.23 & Table-3.24 respectively.

Flare-4A shows the spectral softening when source travels from preflare to flare epoch and spectral index changes from Γ=2.27$\pm$0.01 to 2.32$\pm$0.00 which is described in Table-3.25. Two (Flare-4B & Flare-4D) out of four sub-structures show significant spectral hardening when the source transits from low flux state to high flux state which have been described in Table-3.26 & Table-3.28. The SEDs of different epoch of Flare-4A, Flare-4B, Flare-4C and Flare-4D have been illustrated in Figure-3.39, Figure-3.40, Figure-3.41 and Figure-3.42 respectively. Table-3.27 describe the modelling parameter values of SEDs of different period for Flare-4C.

A clear indication of spectral hardening is also seen in both sub-structures (Flare-5A & Flare-5B) of Flare-5. In Flare-5A, a significant change in Γ (2.60$\pm$0.01 to 2.11$\pm$0.00) has been noticed during Pre-flare to Flare epoch. The SEDs of different periods of activity of these sub-structures have been given in Figure-3.43 & Figure-3.44 respectively. The values of the fitted parameters have been elucidated in Table-3.29 & Table-3.30:.

From the above γ-ray SED analysis of the 3C 454.3 source, we find spectral hardening is an important feature. This has been noticed before by Britto et al. [115] during MJD 56570 - 56863. Only one sub-structure (Flare-4A) shows spectral softening during the change of state from Pre-flare to Flare. The values of the reduced χ^2 for the different spectral models (PL, LP, BPL) have been provided in Table-3.31, which shows that LP is the best-fitted model for most of the flaring states.

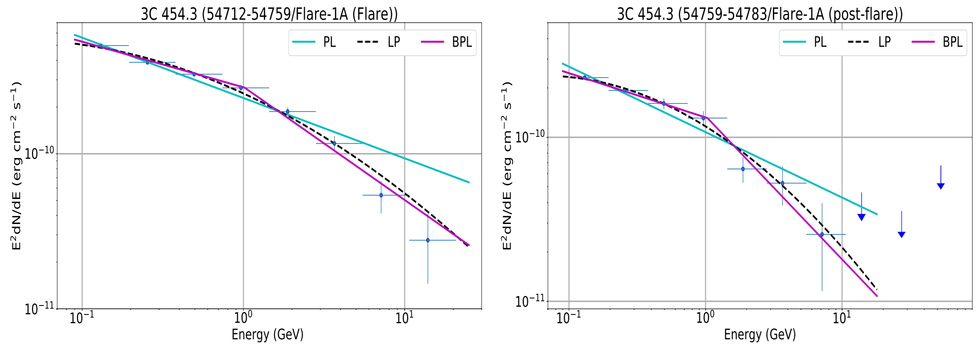

Figure 3.32: SED of different periods of Flare-1A as given in Figure-3.2. PL, LP & BPL describe the Powerlaw, Logparabola and Broken-powerlaw model respectively, which are fitted to data points.

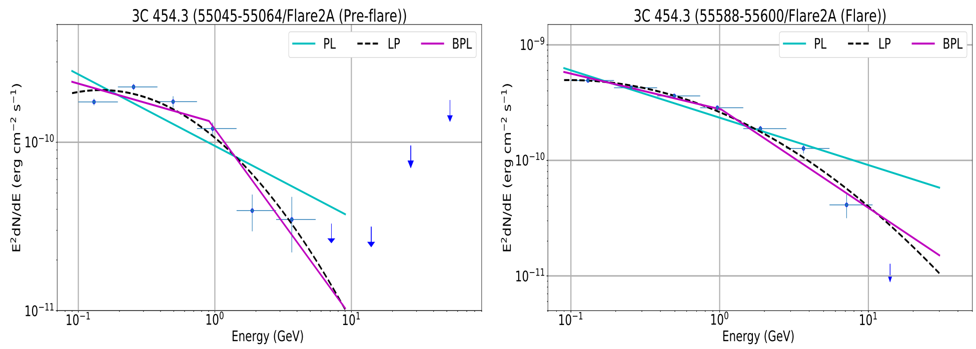

Figure 3.33: SED of different periods of Flare-2A as given in Figure-3.4. PL, LP & BPL describe the Powerlaw, Logparabola and Broken-powerlaw model respectively, which are fitted to data points.

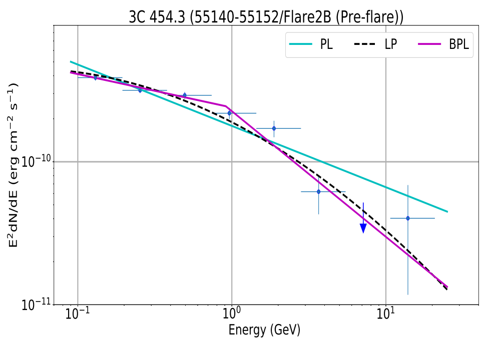

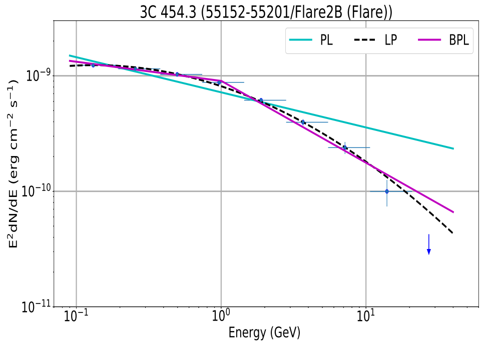

Figure 3.34: SED of different periods of Flare-2B as given in Figure-3.6. PL, LP & BPL describe the Powerlaw, Logparabola and Broken-powerlaw model respectively, which are fitted to data points.

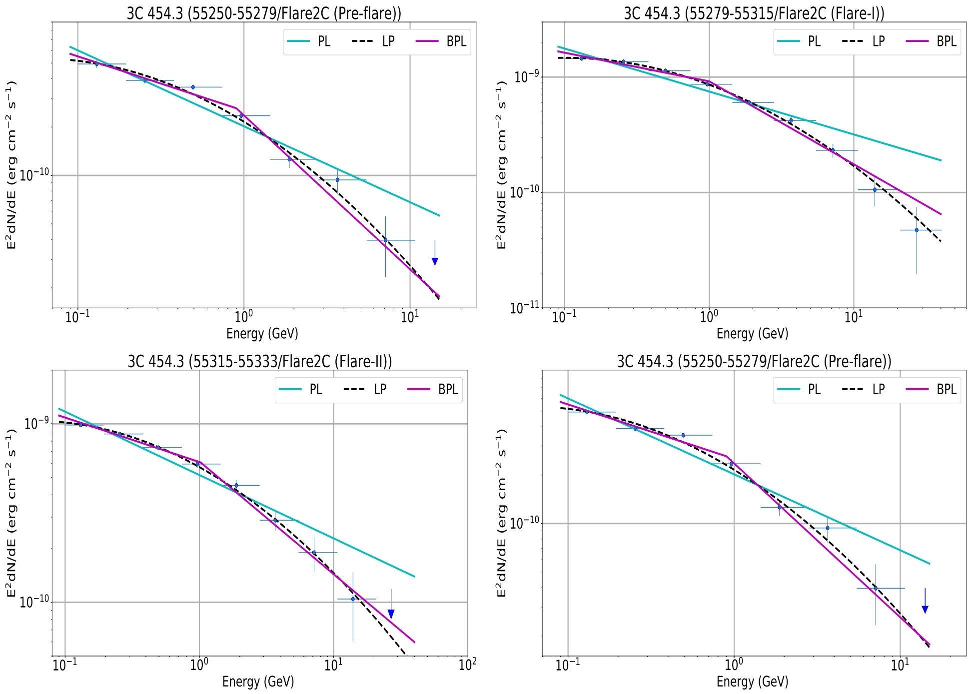

Figure 3.35: SED of different periods of Flare-2C as given in Figure-3.9. PL, LP & BPL describe the Powerlaw, Logparabola and Broken-powerlaw model respectively, which are fitted to data points.

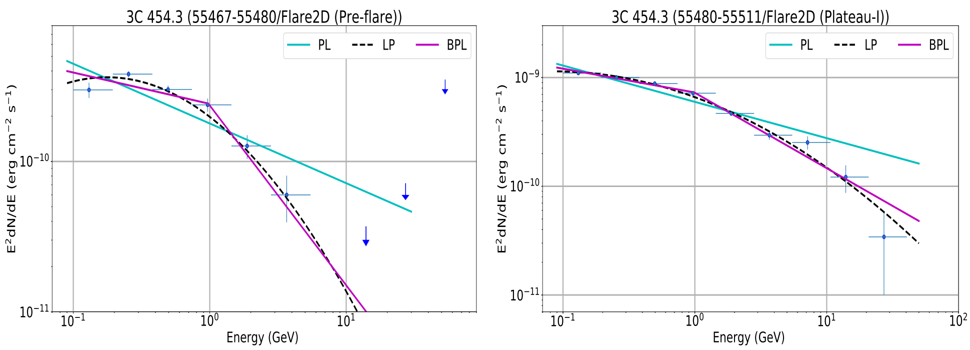

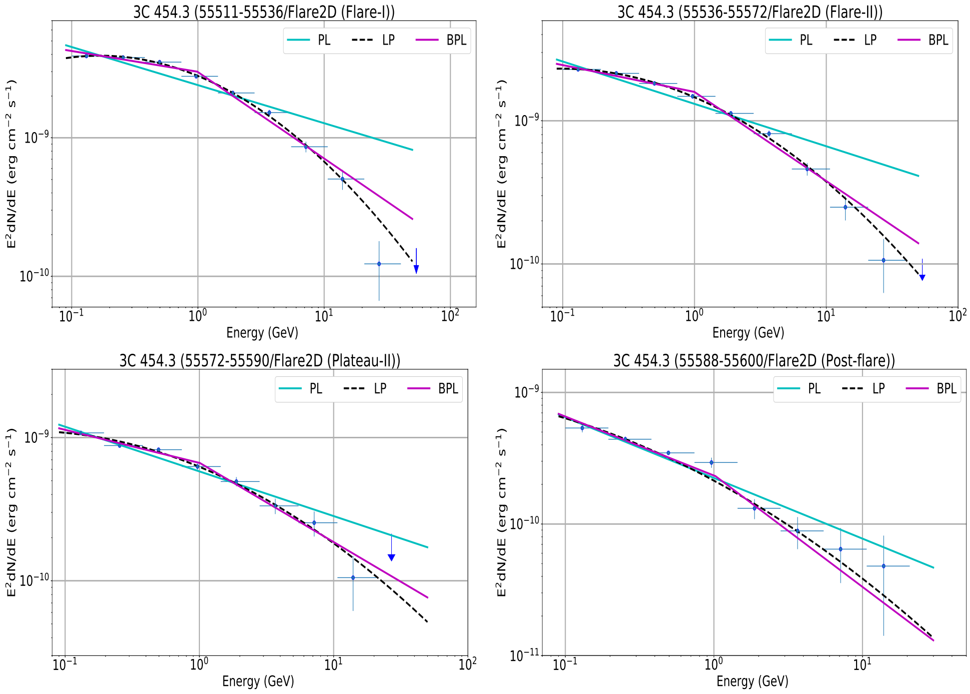

Figure 3.36: SED of different periods of Flare-2D as given in Figure-3.12. PL, LP & BPL describe the Powerlaw, Logparabola and Broken-powerlaw model respectively, which are fitted to data points.

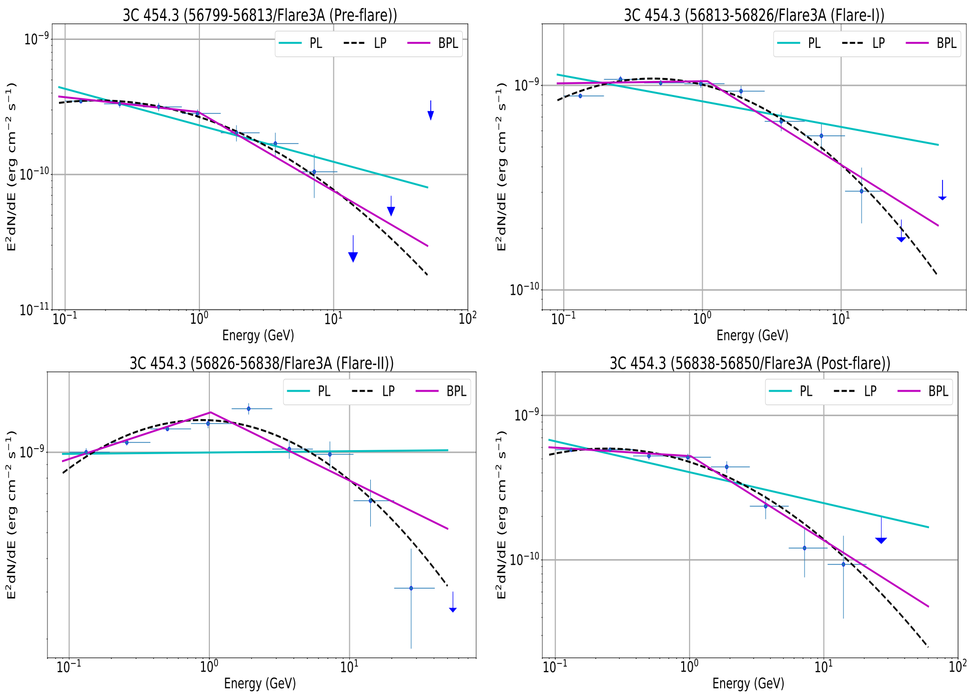

Figure 3.37: SED of different periods of Flare-3A as given in Figure-3.15. PL, LP & BPL describe the Powerlaw, Logparabola and Broken-powerlaw model respectively, which are fitted to data points.

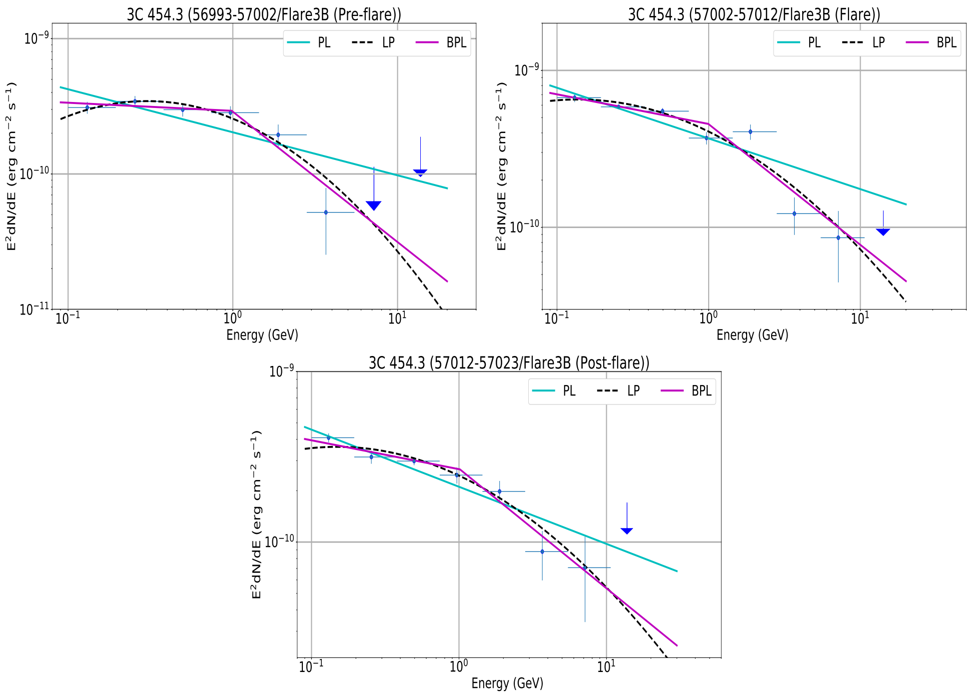

Figure 3.38: SED of different periods of Flare-3B as given in Figure-3.18. PL, LP & BPL describe the Powerlaw, Logparabola and Broken-powerlaw model respectively, which are fitted to data points.

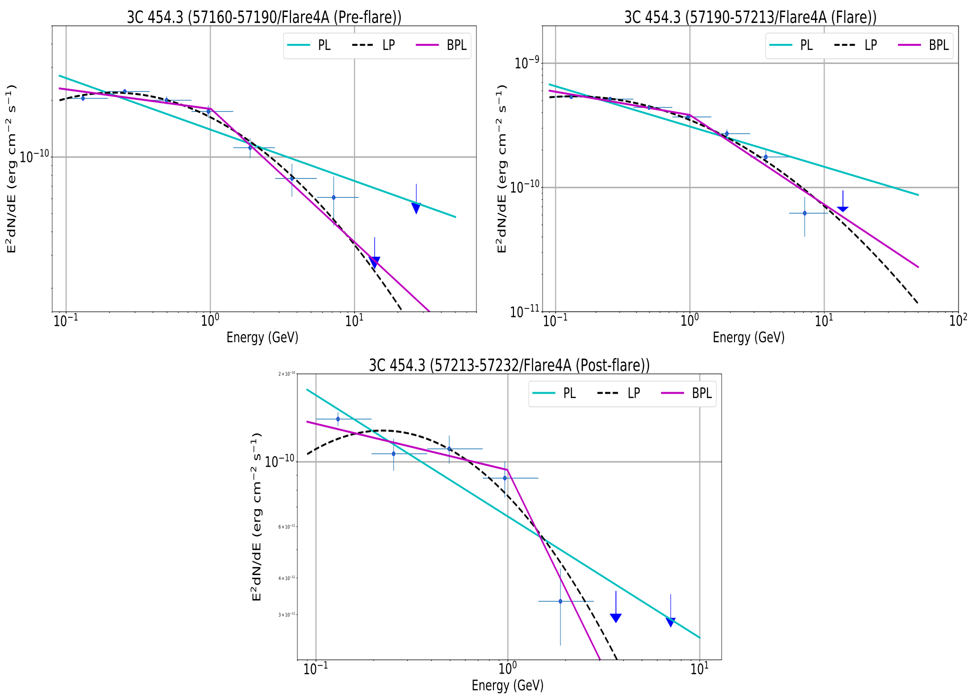

Figure 3.39: SED of different periods of Flare-4A as given in Figure-3.20. PL, LP & BPL describe the Powerlaw, Logparabola and Broken-powerlaw model respectively, which are fitted to data points.

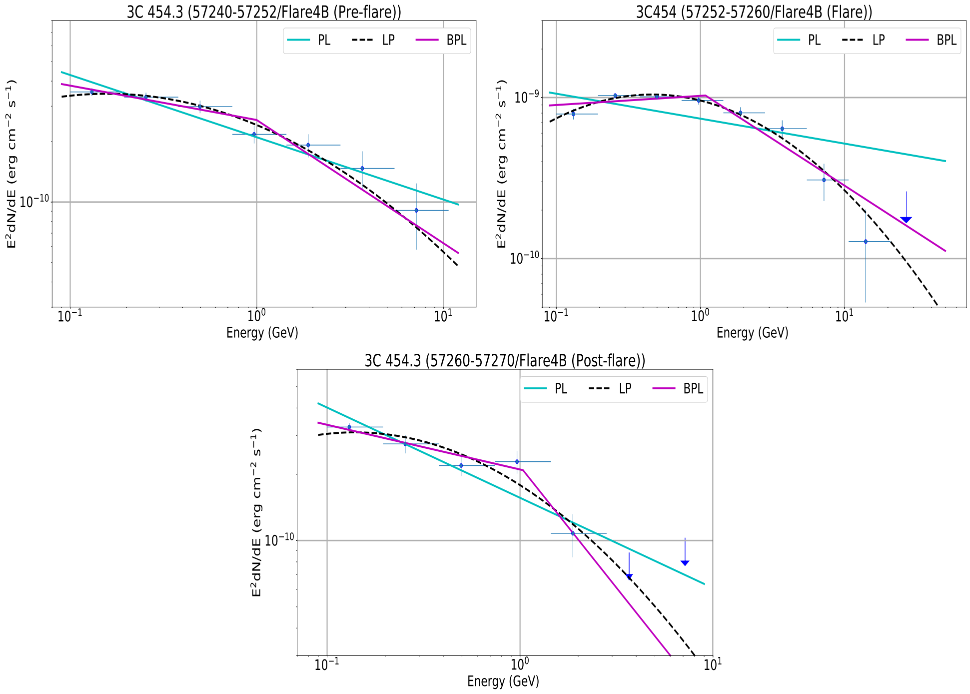

Figure 3.40: SED of different periods of Flare-4B as given in Figure-3.22. PL, LP & BPL describe the Powerlaw, Logparabola and Broken-powerlaw model respectively, which are fitted to data points.

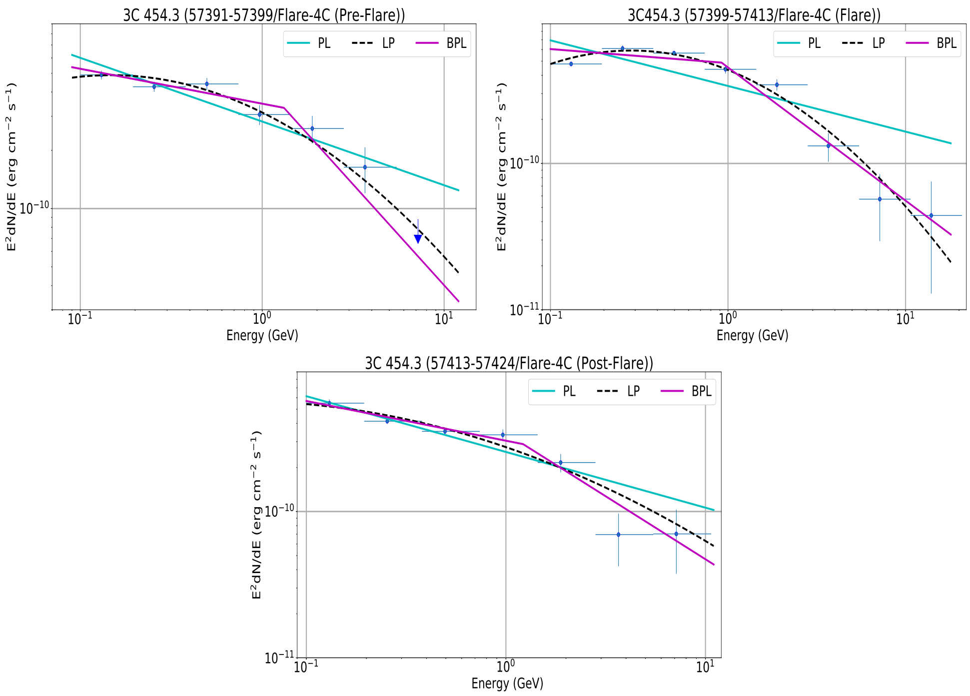

Figure 3.41: SED of different periods of Flare-4C as given in Figure-3.24. PL, LP & BPL describe the Powerlaw, Logparabola and Broken-powerlaw model respectively, which are fitted to data points.

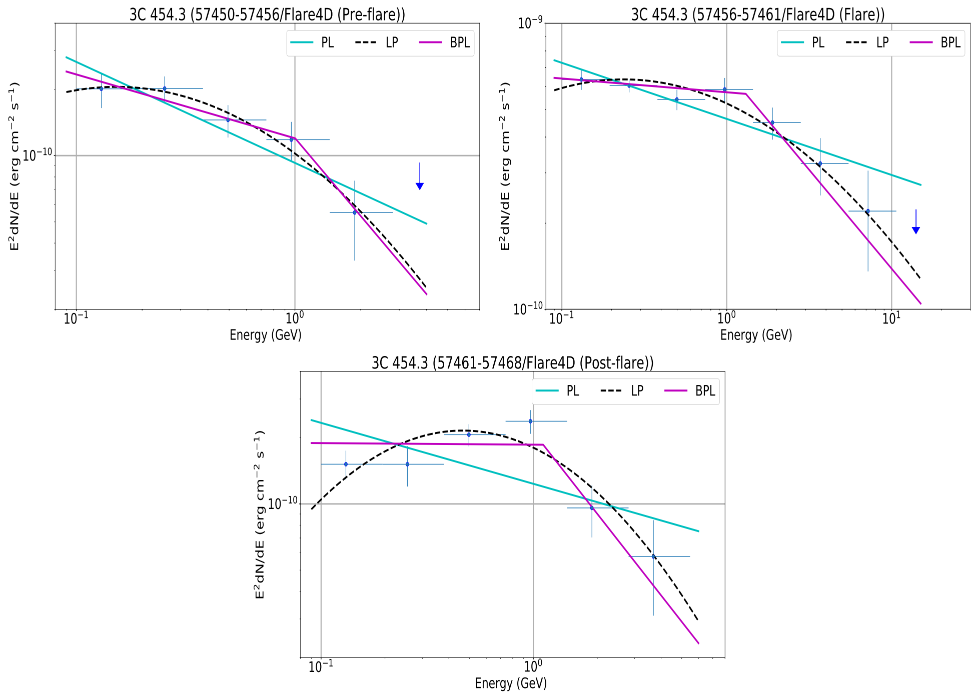

Figure 3.42: SED of different periods of Flare-4D as given in Figure-3.26. PL, LP & BPL describe the Powerlaw, Logparabola and Broken-powerlaw model respectively, which are fitted to data points.

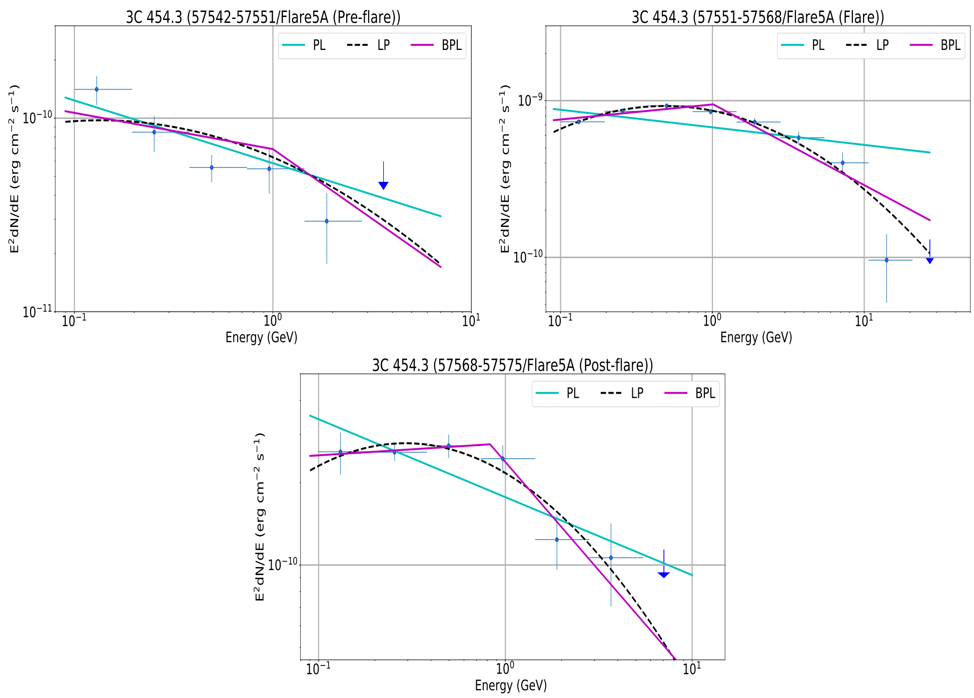

Figure 3.43: SED of different periods of Flare-5A as given in Figure-3.28. PL, LP & BPL describe the Powerlaw, Logparabola and Broken-powerlaw model respectively, which are fitted to data points.

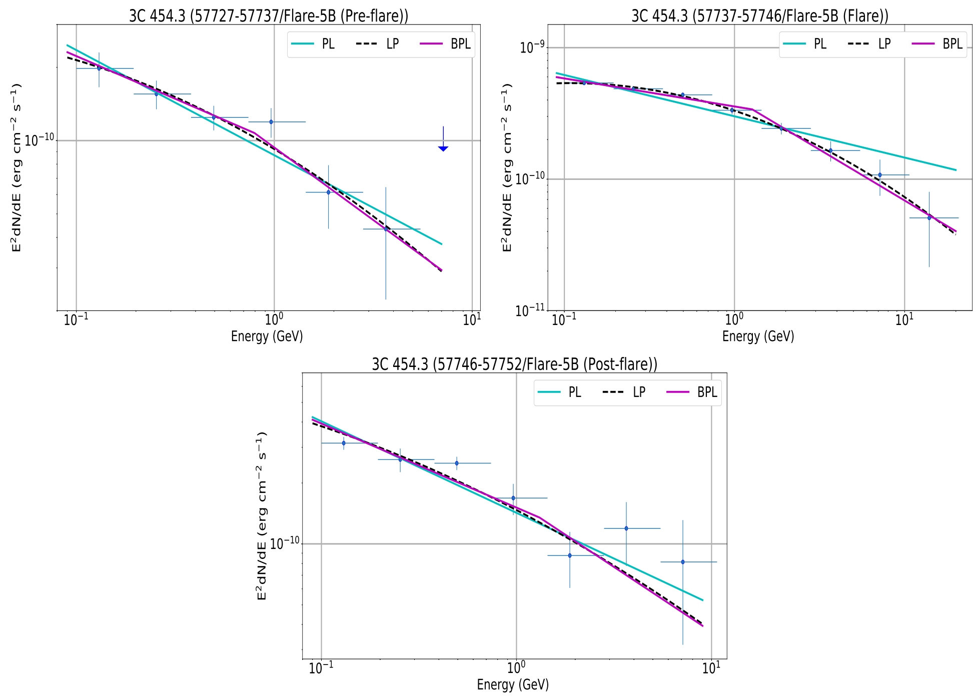

Figure 3.44: SED of different periods of Flare-5B as given in Figure-3.30. PL, LP & BPL describe the Powerlaw, Logparabola and Broken-powerlaw model respectively, which are fitted to data points.

3.6 Multi-wavelength study of 3C 454.3

This section is dedicated to the multi-wavelength study of blazar 3C 454.3. We have chosen the brightest flaring state (Flare-2) of 3C 454.3 from whole 9 year γ-ray light curve (shown in Figure-3.1). We have also collected the simultaneous multi-wavelength data from other instruments and analyzed it. The simultaneous data from other wavebands are X-ray, ultraviolet (UV) & optical from Swift-XRT and UVOT telescope. We have divided this Flare-2 state into four regions labeled as Flare-2A, Flare-2B, Flare-2C & Flare-2D with time duration of MJD 55045-55140, MJD 55140-55201, MJD 55250-55356 & MJD 55467-55600, respectively, which are shown in Figure-45 based on gamma-ray flux as mentioned in subsection-3.4.2. Flare-2A and Flare-2D have simultaneous observation in gamma-ray, X-ray, optical, and UV wavebands and hence for further study, we have concentrated on Flare-2A, and Flare-2D. The multi-wavelength light curve of Flare-2 has been shown in Figure-3.45.

3.6.1 Multi-wavelength Light Curve

Figure-3.46 shows the multi-wavelength light curve of Flare-2A with a time span of 95 days (MJD 55045 - 55140). In the uppermost panel, six-hour binning of γ-ray data and corresponding X-ray, Optical & UV data have been shown in the 2nd, 3rd & 4th rows, respectively. In the γ-ray light curve flux started rising slowly with small fluctuation. The maximum flux was recorded as 6.69$\pm$0.79 at MJD 55091.375, and then the flux decayed slowly with small variation. The average flux of decay period during MJD 55095.6 - 55140.125 is 2.94$\pm$0.05. It is also observed that when the flux was still increasing in gamma-ray, the source started flaring in X-ray, optical, and UV bands. In Swift-XRT dataset maximum peak was observed at MJD 55070.37 with flux of $(8.66\pm0.96)\times10^{-11}$ $erg\ cm^{-2}\ s^{-1}$. During MJD 55094 - 55140 data is not available in XRT photon counting (PC) mode. Similarly Optical & UV data have been also plotted and brightest peak was found at MJD 55069.91 with fluxes of 3.47$\pm$0.13, 3.07$\pm$0.08, 2.71$\pm$0.11, 2.03$\pm$0.09, 2.04±0.08 & 1.74±0.06 in V, B, U, W1, M2 & W2 band, respectively, which are in units of 10^{-11} $erg\ cm^{-2}\ s^{-1}$. In V, U, W1, M2, the second brightest peak was observed at MJD 55091.18, which coincided with the first γ-ray brightest peak with a time lag of $\sim$ 5 hours, while in the B band maximum peak was noticed at MJD 55090.92 with a time lag of $\sim$ 11 hours.

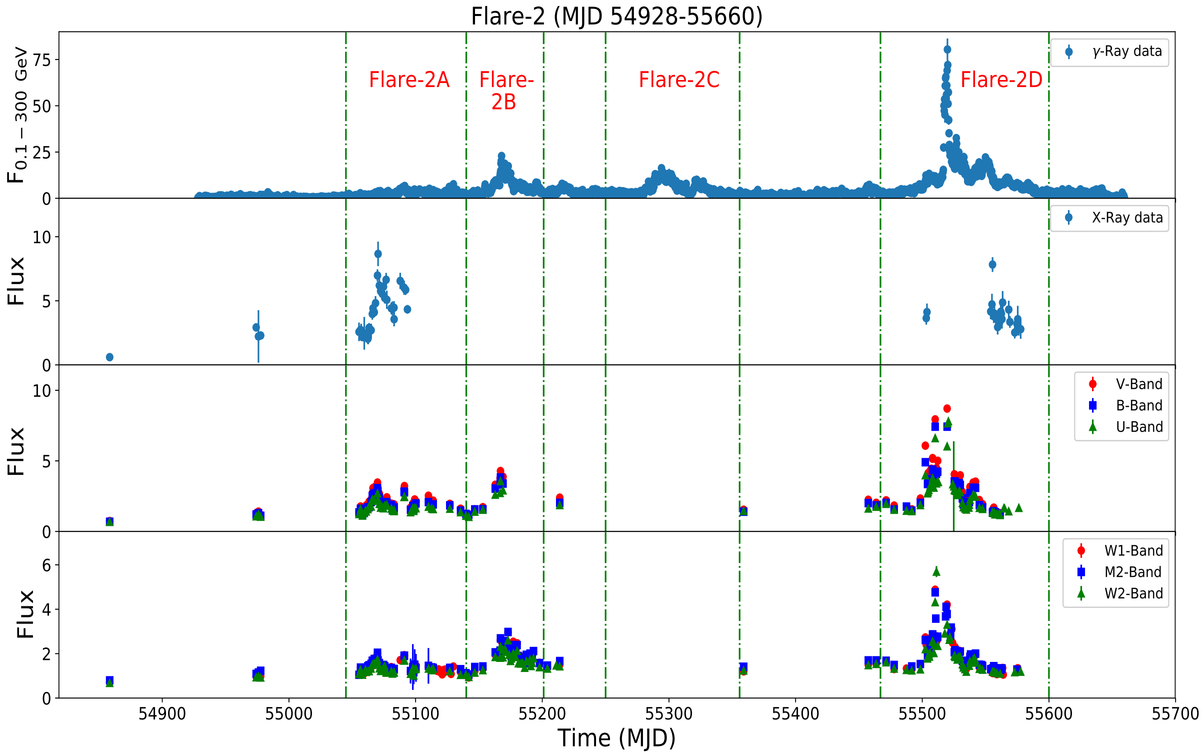

Figure 3.45: Multi-wavelength light curve of Flare-2. Four distinctive major Flare have been identified. γ-ray flux ($F_{0.1-300GeV}$) is in unit of 10^{-6} $ph\ cm^{-2}s^{-1}$. X-ray, optical (V, B & U-band) & Ultra-violet (W1, M2 & W2-band) fluxes are in unit of 10^{-11} $erg\ cm^{-2}$ s^{-1}

The multi-wavelength light curve of Flare-2D has been shown in Figure-3.47 which has a time duration of 133 days (MJD 55467.125 - 55600.125). The highest flux was recorded at MJD 55519.875 with flux of 80.41±5.93 in six hour bin γ-ray waveband. After this the flux started decreasing slowly with small variation during MJD 55536.6 - 55590.1 and the average flux was 9.80±0.06 . We are unable to observe any peak in XRT PC mode due to unavailability of the simultaneous data during MJD 55504 - 55554. All the peaks in optical & UV band nearly coincide with the peaks observed in γ-ray band. Interestingly, the peaks in optical & UV band during MJD 55510.1-55511.4, have no γ-ray counterpart which has been reported earlier in several cases (Vercellone et al. [132], Rajput et al. [116]).

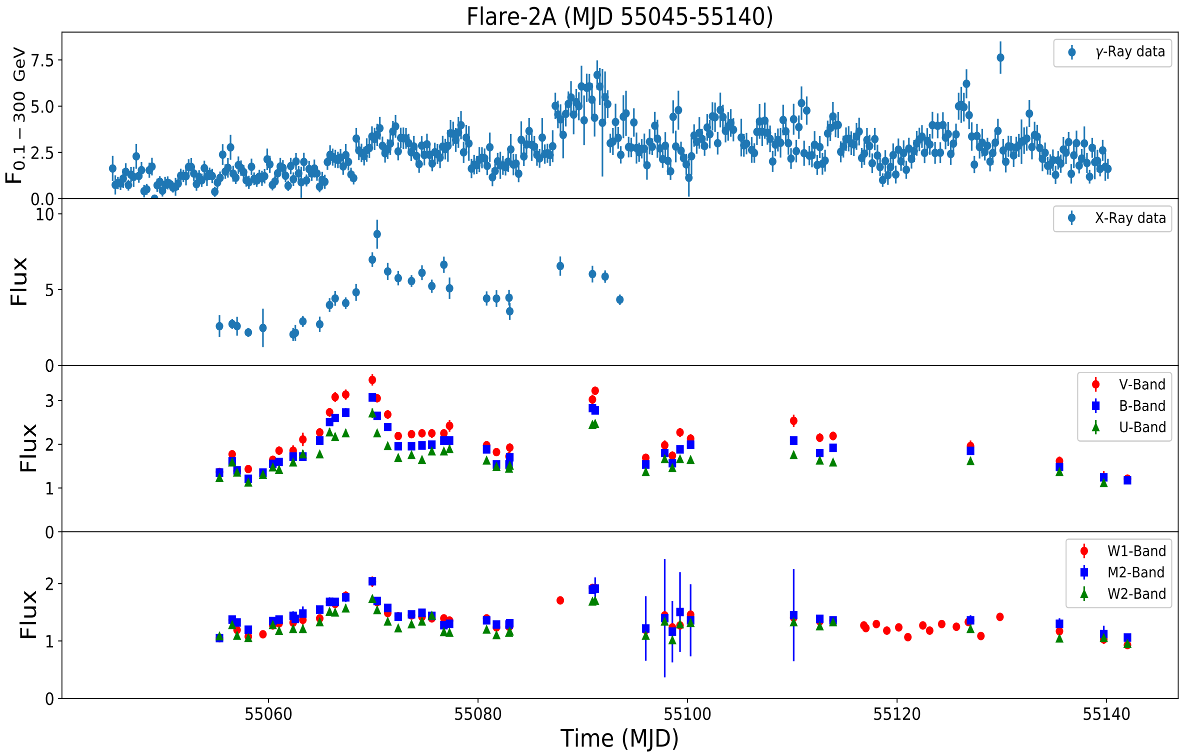

Figure 3.46: Multi-wavelength light curve of Flare-2A. γ-ray flux ($F_{0.1-300GeV}$) is in unit of 10^{-6} $ph\ cm^{-2}s^{-1}$.X-ray, optical (V, B & U-band) & ultra-violet (W1, M2 & W2-band) fluxes are in unit of 10^{-11} $erg\ cm^{-2}\ s^{-1}$.

3.6.2 Multi-wavelength SED modelling

We have Modelled the multi-wavelength SEDs with the time dependent 'GAMERA' (Hahn [133]) code, which is publicly available on github webpage[3]. This code solves the time dependent continuity equation, calculates the evolved electron spectrum N(E,t)

[3]https://github.com/libgamera/GAMERA

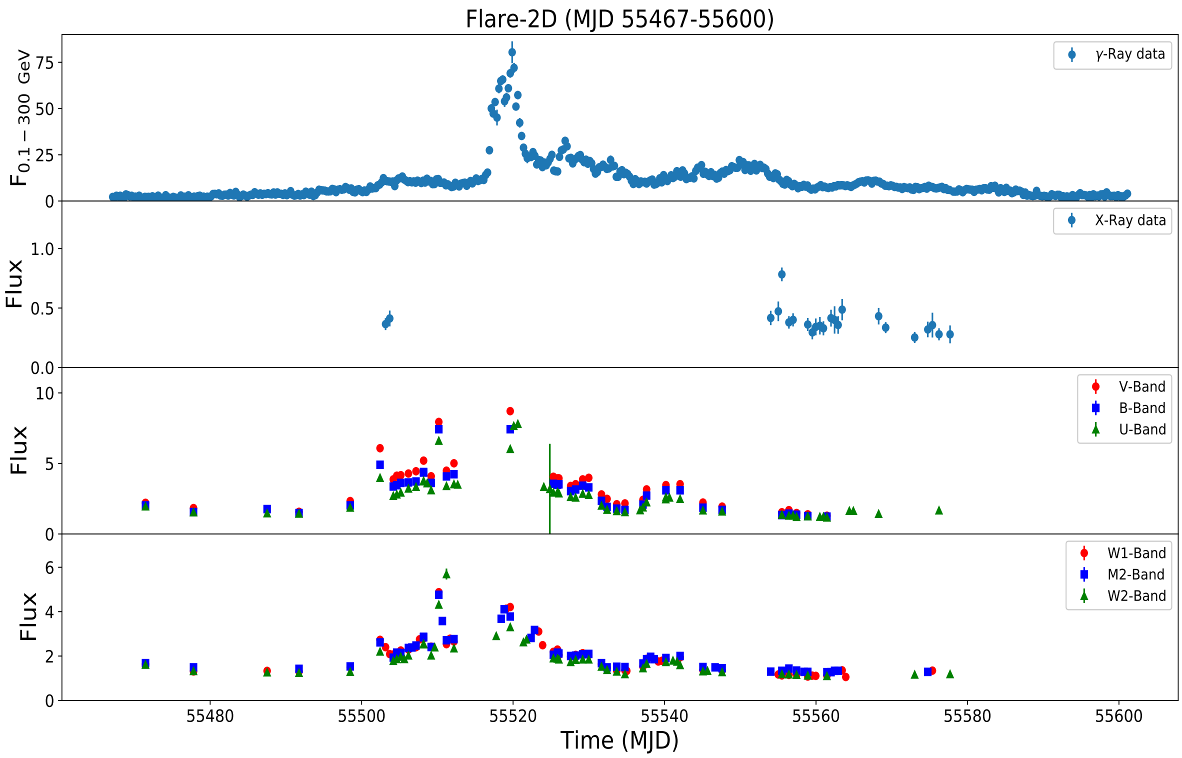

Figure 3.47: Multi-wavelength light curve of Flare-2D. γ-ray flux ($F_{0.1-300GeV}$) is in unit of 10^{-6} $ph\ cm^{-2}s^{-1}$. X-ray, optical (V, B & U-band) & ultra-violet (W1, M2 & W2-band) fluxes are in unit of 10^{-11} $erg\ cm^{-2}\ s^{-1}$.

and then computes the synchrotron & inverse Compton emission for that N(E,t). The continuity equation is given by -

$$\frac{\partial N(E,t)}{\partial t} = Q(E,t) - \frac{\partial}{\partial E}(b(E,t)N(E,t)) - \frac{N(E,t)}{\tau_{esc}(E,t)} \tag{3.7}$$

where Q(E,t) is the injected electrons spectrum. The energy loss rate is denoted by b(E) = $(\frac{dE}{dt})$ and $\tau_{esc}(E,t)$ represents the escape time. Log-Parabolic model gives the best fitted parameters for most of the sub-structures in the γ-ray SED, which have been described in Table-30. The radiative losses of LP electron spectrum produce LP photon spectrum. (Massaro et al. [134]) gave a general formalism to show that if the efficiency of acceleration decreases with increasing energy, the resulting shock electron spectrum follows LP distribution. Due to this reason we have assumed LP form of Q(E,t). Functional form of Q(E,t) is defined by -

$$Q(E) = l_0(\frac{E}{E_{ref}})^{-(\alpha+\beta\log(E/E_{ref}))} \tag{3.8}$$

where l_0 is normalization constant & E_{ref} is the reference energy which is set at 90.0 MeV. 'GAMERA' uses the full Klein-Nishina cross section to compute the inverse-Compton (IC) emission (Blumenthal and Gould [135]).

3.6.3 Physical constraints

Here we discuss about the constraints on the model parameters that we have used in our modelling -

1. To calculate the EC emission by the relativistic electrons the CMB (Cosmic Microwave Background) and BLR (Broad Line Region) photons are taken into account as target photons. The standard value of CMB photon density (0.25 eVcm^{-3}, Longair [136]) has been used. The energy density of BLR photons is computed (in the comoving frame) with the following equation

$$U'_{BLR} = \frac{\Gamma^2\zeta_{BLR}L_{Disk}}{4\pi c R^2_{BLR}} \tag{3.9}$$

   where Γ is the bulk Lorentz factor of the emitting blob whose value is assumed to be 20 (Vercellone et al. [132]). The BLR photon energy density is only a fraction of 10% ($\zeta_{BLR} \sim 0.1$) of the accretion disk photon energy density. The value of the disk luminosity $L_{Disk} = 6.75 \times 10^{46} erg/sec$ is taken from Bonnoli et al. 137. We have computed the radius of the BLR region by the scaling relation $R_{BLR} = 10^{17}L^{1/2}_{d,45}$ where $L_{d,45}$ [138] is the disk luminosity in units of $10^{45} erg/sec$.

2. We have also included emission from accretion disk component in the code to compute the EC emission. We constrain the disk energy density in the comoving jet

frame by the following equation (Dermer and Menon [139])

$$U'_{Disk} = \frac{0.207 R_g L_{Disk}}{\pi c Z^3 \Gamma^2} \tag{3.10}$$

We chose the mass of the central engine or Black Hole (M_{BH}) as $5 \times 10^8 M_\odot$ (Bonnoli et al. [137]) in order to estimate the gravitational radius $R_g = 1.48{\times}10^{14}$ cm. Distance of the emission region from the black hole is represented by 'Z'. The upper limit of this quantity is estimated by the given equation (Paliya [140]) -

$$Z \leqslant \frac{2\Gamma^2 c t_{var}}{1+z} \tag{3.11}$$

Where z is the redshift of the source. The variability time estimated during Flare-2 is found to be $t_{var} = 1.93$ hour during MJD 55068.125 - 55068.375, (corresponds to Flare-2A) which has been used to estimate 'Z'. The value of 'Z' is estimated as $Z \sim 1.0{\times}10^{17}$ cm.

3. We can estimate the upper limit on the size of the emission region R with the following relation -

$$R \leqslant \frac{c t_{var} \delta}{1+z}. \tag{3.12}$$

We have used $t_{var} = 1.93$ hour & Doppler factor $\delta = 27.5$ (comparable to Bonnoli et al. [137]) for Flare-2 which give the value of $R = 3.08 \times 10^{15}$ cm. But it is noted that equation (3.11) is just an approximation and there are several effects that may introduce large error in determining R (Protheroe [141]). Moreover the value of R calculated in this way for γ-ray wavelength does not give a good fit to the data in our SED modelling. In our work we have chosen $R = 3.0 \times 10^{16}$ cm which is comparable to the value $5{\times}10^{16}$ cm given by Gupta et al. 142.

4. We have used typical values of BLR temperature (T'_{BLR}) & Disk temperature (T'_{Disk}) in our model, which are 2.0×10^4 K and 1.0×10^6 K respectively.

3.6.4 Model the SEDs

After constraining the above model parameters we have simulated the multi-wavelength SED using the code 'GAMERA'. We have included the escape term ($-\frac{N(E,t)}{\tau_{esc}(E,t)}$) for electrons in the continuity equation (3.6) and considered two different cases -

- Case 1: In this case we have studied the model with constant escape time which is $\tau_{esc} \sim R/c$, where R is the size of the emission region.
- Case 2: Next we consider energy dependent escape time which is given by $\tau_{esc} = \eta E^{-0.5}$ (Sinha et al. [143]). We have chosen the following values $\eta \sim$ 387.0 & 155.0 sec MeV$^{1/2}$ for Flare-2A and Flare-2D respectively, so that at low energy the escape time is comparable to the cooling time of electrons.

SED modelling has been done for the above two cases for both the flares (Flare-2A & Flare-2D), which have been illustrated in Figure-3.48 and Figure-3.49. We have shown the non-simultaneous archival data for both the flares in cyan colour represented by plus symbol, which are taken from (Abdo et al. [144]). There are no simultaneous archival data available for Flare-2A. However, quasi-simultaneous data from MJD 55515 - 55524 (Vercellone et al. [132]) and for MJD 55519 (Jorstad et al. [145]) are available for Flare-2D and they are shown with black triangle and green star symbol in Figure-3.48 & Figure-3.49. In our work the SED is averaged over the whole flaring period, i.e. 133 days from MJD 55467 - 55600. However, the SED data points shown in black and green colour are for the peak of the flare, which lasted for very short period compared to our period (133 days) and hence our SED data points differ from them.

In our study, we have adjusted the values of the following parameters to obtain the best fitted model: Magnetic field in the emission region (B), minimum & maximum Lorentz

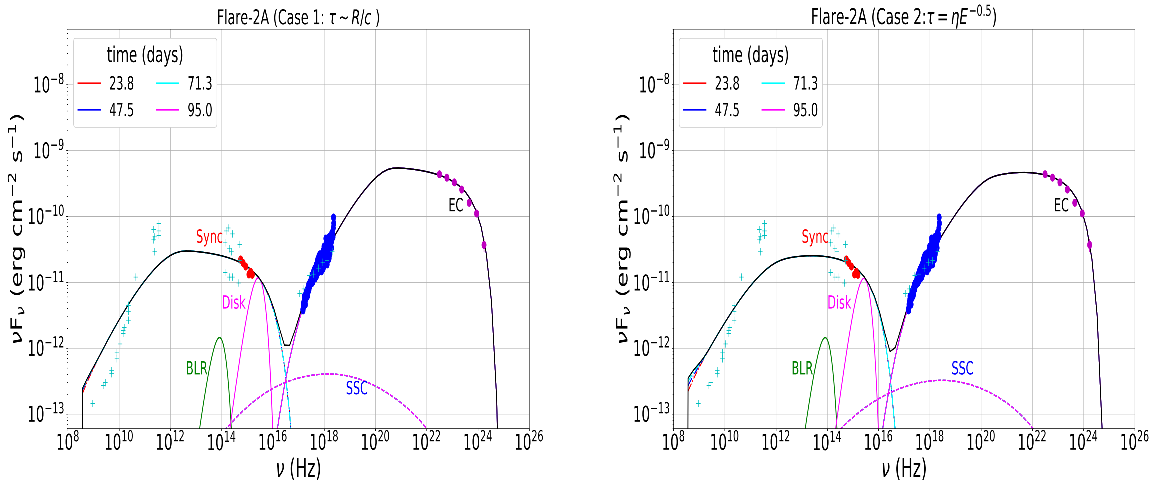

Figure 3.48: Multiwavelength SED of Flare-2A for two different cases of escape timescale. Our analyzed data is shown in Red, Blue & purple color. Non-simultaneous data (see text for more details) is shown in cyan plus point, which is taken from Abdo et al. [144].

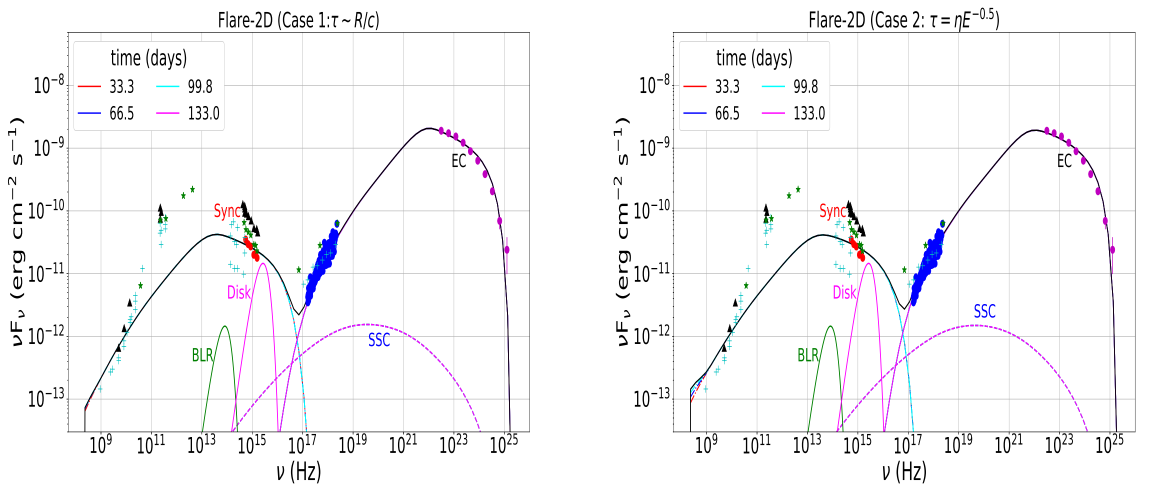

Figure 3.49: Multi-wavelength SED of Flare-2D for two different cases of escape timescale. Our analyzed data is shown in Red, Blue & purple color. Non-simultaneous data (see text for more details) is shown in cyan plus point, which is taken from Abdo et al. [144]. quasi-simultaneous data is also shown in black triangle ([132]) and green star point (Jorstad et al. [145]).

factor of the injected relativistic electrons (γ_{min}&γ_{max}) and their spectral index (α) & curvature index (β). We have obtained the values of B = 3.80 & 2.30 G for Flare-2A and Flare-2D respectively, by fitting the synchrotron emission of the relativistic electrons to the optical data. The value of spectral index (α) is 2.00 & 2.18 for Flare-2A and Flare-2D respectively. For Flare-2A the value of minimum Lorentz factor (γ_{min}) is 55 & 45 in case-1 and case-2 respectively. For Flare-2A & Flare-2D there is no significant difference in the values of the the maximum Lorentz factor of the injected electrons (γ_{max}), however curvature index (β) varies significantly for Flare-2D (β = 0.09 for case-1 and β = 0.14 for case-2) whereas it remains similar for Flare-2A. The detailed results of the multi-wavelength SED modelling have been described in Table-3.32.

We have also calculated the total required jet power by using the following equation -

$$P_{tot} = \pi R^2 \Gamma^2 c (U'_e + U'_B + U'_p) \tag{3.13}$$

where U'_e, U'_B & U'_p are the energy density of electrons (and positrons), magnetic field & cold protons respectively in the comoving jet frame. The power carries by the injected electrons in the jet is given by -

$$P_e = \frac{3\Gamma^2 c}{4R} \int_{E_{min}}^{E_{max}} EQ(E)dE \tag{3.14}$$

where $Q(E)$ is the injected electron spectrum as defined in equation (3.8). To compute U'_p we have assumed the ratio of electron-positron pair to proton number in the emission region is 10:1. From equation (3.13) we have calculated the maximum required jet power (P_{tot}) in our model which is found to be 3.04×10^{46} erg/sec. This value is lower than the estimated range of Eddington's luminosity (L_{Edd}) - $(0.6-5)\times10^{47}$ erg/sec (Bonnoli et al. [137], Gu et al. [146], Khangulyan et al. [147]).

3.7 Model the light curves

Our SEDs represent the time averaged flux over a very long time period. This is why the average values of the model parameters (Doppler factor, magnetic field, luminosity in injected electrons, blob size, viewing angle) are used in modelling the SEDs of Flare 2A and Flare 2D. Light curves represent the photon fluxes at different time epochs. The time variation of photon fluxes, representing complicated structures, reflects instantaneous perturbations in the emission zone. Time dependent modelling of blazars (Saito et al. [148]; Potter [149]) has been used earlier to simulate the photon fluxes with time. Simulated profiles of flares of PKS 1510-089 were analysed in optical, X-ray, high energy and very high energy gamma-ray for timescale of hours [148]. Simultaneous multi-wavelength data is not available at different frequencies to test their model predictions. The time variation of some of the parameters involved in modelling may generate time dependent photon flux to mimic the flare peaks in the light curves over short time intervals.

In this section, we discuss about the modelling of the γ-ray light curves using multi-wavelength SED parameters. We have chosen short duration flare peaks of the following three types, $T_r > T_d$, $T_r < T_d$, and $T_r \sim T_d$, since the long duration peaks have much more complex time dependent structures. These peaks are: Peak P5 ($T_r > T_d$), P1 ($T_r < T_d$) & P3 ($T_r \sim T_d$). Since Flare 2B (Figure-7, MJD 55152 - 55177) has many peaks which include all the three types of peaks $T_r = T_d$, $T_r > T_d$ and $T_r < T_d$, we have chosen three different types of peaks of this flare. We have modelled the light curves by varying separately the Doppler factor (δ) and the normalisation constant of the injected electron flux (l_0). While doing this we fixed the other SED model parameters (E_{min}, E_{max}, B, R, etc.) to their average values as used for SED modelling of Flare-2A since multi-wavelength data of Flare 2B is not available for SED modelling.

1. Case 1: In this case we calculate the light curve by varying the Doppler factor as a function of time which goes as broken-powerlaw

$$\delta = \begin{cases} kt^{a_1}, & \text{for } t < t_c \\ k{t_c}^{(a_1-a_2)}t^{a_2}, & \text{otherwise} \end{cases} \tag{3.15}$$

   where t_c is peak time, k is normalization constant and a_1, a_2 are the indices of the broken-powerlaw. The blob is boosted to a higher Doppler factor which causes the rise in photon flux and then slows down during the decay phase. Due to poor photon statistics a detailed modelling of the time variation of the Doppler factor is not possible at this stage. We have calculated the integrated γ-ray flux in the Fermi LAT energy range (0.1$\leqslant$E$\leqslant$300 GeV) in each time step from the multi-wavelength SED model and fitted to the light curve data points. Our results are shown in Figure-3.50, Figure-3.51 & Figure-3.52 for the three types of flare peaks. The best fitted model parameters in 3.15 along with the range of values of the Doppler factor (δ) have been displayed in Table-3.33

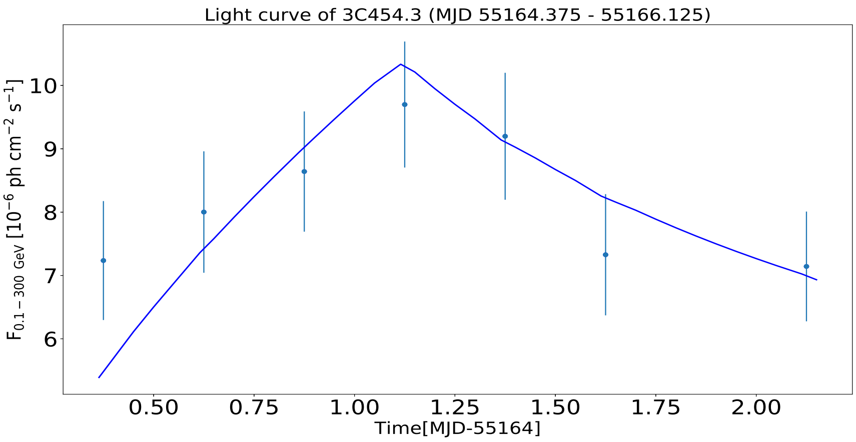

Figure 3.50: Modelled light curve (by varying Doppler factor) between the data of MJD 55164.375 - 55166.125, which corresponds to P3 peak of 1st part of Flare-2B.

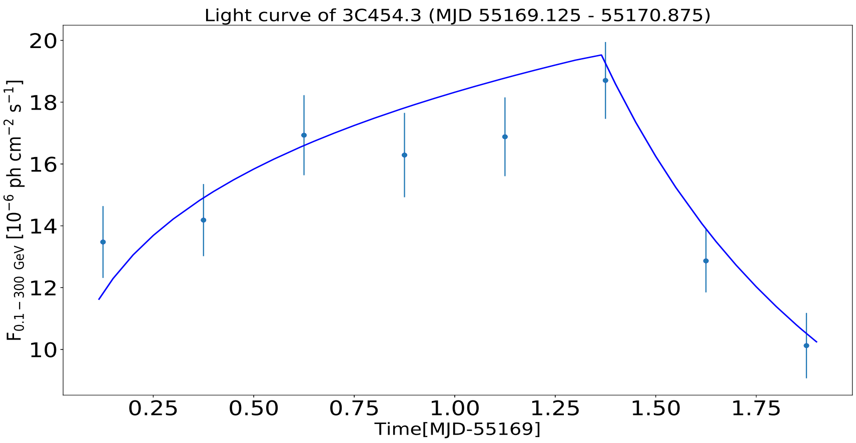

Figure 3.51: Modelled light curve (by varying Doppler factor) between the data of MJD 55169.125 - 55170.875, which corresponds to P5 peak of 1st part of Flare-2B.

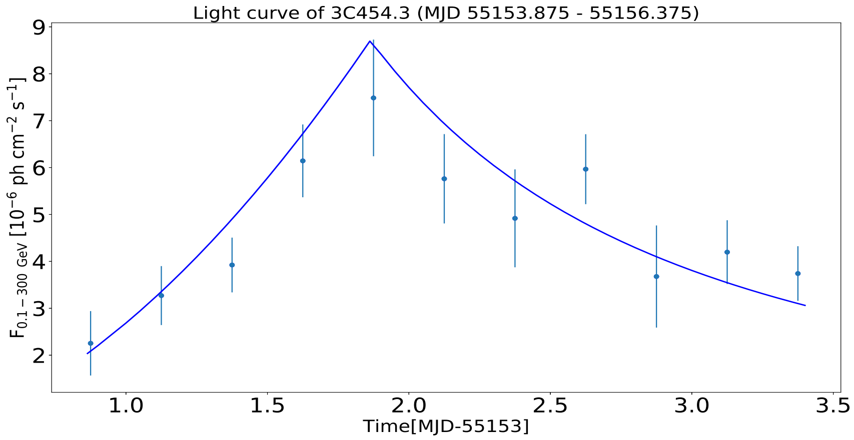

Figure 3.52: Modelled light curve (by varying Doppler factor) between the data of MJD 55153.875 - 55156.375, which corresponds to P1 peak of 1st part of Flare-2B.

2. Case 2: In this case we fix the Doppler factor to its average value of Flare-2A but vary the normalisation constant (l_0) of the injected electron flux (equation 3.8) with a functional form similar to δ, which is defined by-

$$l_0 = \begin{cases} kt^{a_3}, & \text{for } t < t_c \\ kt_c{}^{(a_3-a_4)}t^{a_4}, & \text{otherwise} \end{cases} \tag{3.16}$$

where t_c is peak time, k is normalization constant and a_3, a_4 are the indices of the broken-powerlaw.

The normalisation constant of the injected electron flux in the emission region increases which causes the peak in the light curve and subsequently it decreases when the photon flux diminishes. Similar to case 1, it is not possible to get more accurate result on time variation of normalisation constant l_0 due to poor photon statistics. We have calculated the integrated γ-ray flux from our SED model in each time step to obtain the simulated light curve as before. Our simulated light curves of these peaks have been shown in Figure-3.53, Figure-3.54 and Figure-3.55 respectively. The best fitted values of the parameters in equation 3.15 along with the ranges in the values of the normalisation constant (l_0) and injected power in electrons (P_e)

for each flare peak have been given in Table-3.34

Thus we show that the light curves can be approximately generated by varying the Doppler factor (δ) or the normalisation constant (l_0).

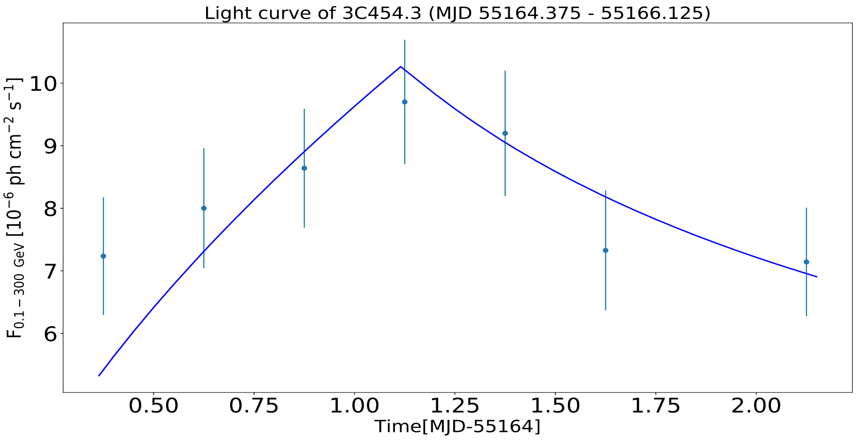

Figure 3.53: Modelled light curve (by varying normalisation constant of the flux of injected electrons) between the data of MJD 55164.375 - 55166.125, which corresponds to P3 peak of 1st part of Flare-2B.

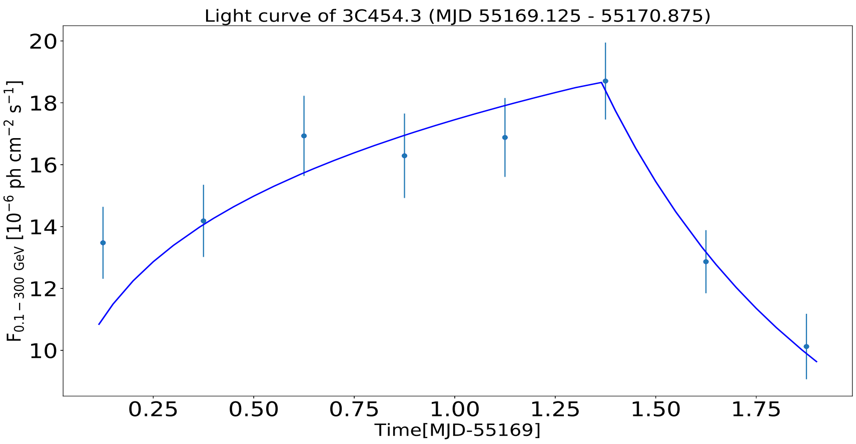

Figure 3.54: Modelled light curve (by varying normalisation constant of the flux of injected electrons) between the data of MJD 55169.125 - 55170.875, which corresponds to P5 peak of 1st part of Flare-2B.

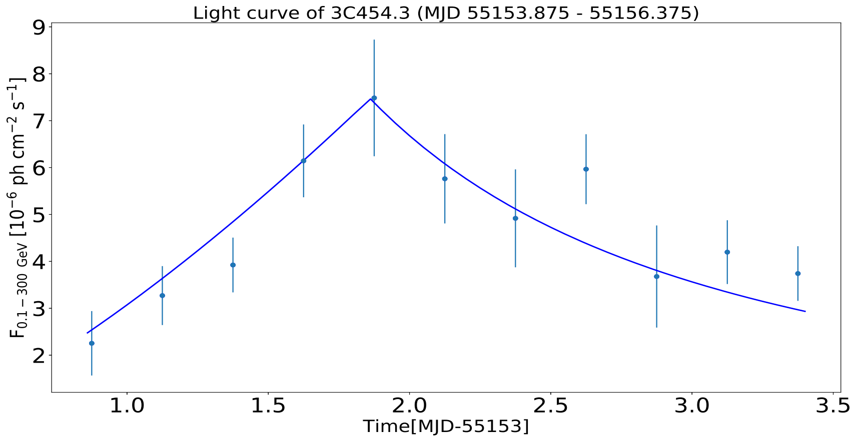

Figure 3.55: Modelled light curve (by varying normalisation constant of the flux of injected electrons) between the data of MJD 55153.875 - 55156.375, which corresponds to P1 peak of 1st part of Flare-2B.

3.8 Summary & Discussion

3C 454.3 is one of the most violent source in the Fermi 3FGL catalog. We have analyzed the light curve of this source in γ-ray for 7-day time bin during August 2008 - July 2017, which consists of five major flares as shown in Figure-3.1. Each major flare comprises several sub-structures (or sub-flares) identified in 1-day & 6-hour binning analysis. All the sub-structures show different phases of activity (e.g., Pre-flare, Flare, Plateau, Post-flare). Flare regions of each sub-structure consist of several distinctive peaks (labeled as P1, P2, etc.) of different photon counts. Only one sub-structure, Flare-1A has been identified in Flare-1. The light curve of Flare-1 is shown in Figure-3.2 for 1 day binning, which shows Flare and Post-flare phases. The peaks P1, P2, and, P3 are identified in Figure-3.3 for the flare phase of Flare-1A. The gamma-ray SED data points are fitted with log-parabola, broken-power law, and power-law functions to find which function gives the best fit to the data. The same procedure has been carried out for all the flares subsequently for 6 hours binning except Flare-2A, where we have used the same binning as Flare-1A. Table-30 shows that in most cases, the gamma-ray SEDs of flares are well represented by the log-parabola function. The scanning of 6 hours binning light curve is done to estimate the variability time scale in gamma-ray emission. The results are displayed in Table-3.15 & Table-3.16. The shortest variability time is found to be hour scale (1.70±0.38). The rise and decay timescales of flares are studied to see whether they follow any trend. Characteristic rising & decay timescales (T_r & T_d) have been computed for each peak which are shown in Table 3.1 - Table 3.13. We have found that the values of T_r and T_d vary between an hour to day scale for different peaks. To compare these two timescales (T_r & T_d) we define a quantity K, which is given by ([130]) -

$$K = \frac{T_d - T_r}{T_d + T_r} \tag{3.17}$$

- Rising timescale is greater than decay timescale ($T_r > T_d$) when $K < -0.3$. This may happen when injection rate is slower than the cooling rate of electrons into the emission region. The electrons can lose energy through IC & synchrotron cooling.

- Decay timescale is greater than rising timescale ($T_r < T_d$) when $K > 0.3$. This could be due to longer cooling timescale of electrons.

- Nearly equal rising and decay timescale ($T_r \sim T_d$) or symmetric temporal evolution when $-0.3 \leqslant K \leqslant 0.3$. This property can be explained by perturbation in the jet or a dense plasma blob passing through a standing shock front in the jet region (Blandford and Königl [150]).

In our study we have found that out of total 69 prominent peaks 16 peaks have $T_r > T_d$, 20 peaks have $T_r < T_d$ and 33 peaks have $T_r \sim T_d$.

The SED modelling has been done, for the two flares Flare-2A and Flare-2D for which multi-wavelength data are available. The modelling has been done with the time-dependent code GAMERA, which solves the transport equation for electrons, including their energy losses by synchrotron and inverse Compton emission (SSC and EC), and escape. We have considered two cases for the escape timescale (i) constant escape time $R/c = 10^6$ sec and (ii) energy-dependent escape time, which goes as $E^{-0.5}$. We note that the cooling timescale of the electrons in case (i) is much shorter than R/c in our case. In case (ii) the escape time is comparable to the cooling time for low energy electrons, but for high energy electrons, the cooling time decreases faster than the escape time as it goes as E^{-1}. Table-3.31 shows the results of our SED modelling. The results for the two cases are comparable for both the flares Flare-2A and Flare-2D. The magnetic field is slightly higher for Flare-2A. The jet power in relativistic electrons and positrons is higher for Flare-2D compared to Flare-2A. Figure-3.48 and Figure-3.49 show the results of our SED modelling. If we divide the duration of a flare into four equal time intervals, the SED calculated for each time interval overlaps with each other. The electron spectrum becomes steady in a short time compared to the duration of Flare-2A and Flare-2D; as a result, their radiated photon spectrum also becomes steady. Due to this reason, it is not possible to see the time evolution in Figure-3.48 and Figure-3.49.

3C 454.3, being highly variable in gamma-rays is often monitored. The data from July 7-October 6 of 2008 was analyzed to study the flaring activity during this period Abdo et al. [151]. They observed nearly symmetric flares with the rise and decay timescales of 3.5 days, and obtained a lower bound of 8 on the value of the Doppler factor. A broken power law best represents their gamma-ray SED with a break near 2 GeV. They suggested this break may be due to an intrinsic break in the electron spectrum.

Finke and Dermer [121] suggested a combination of the Compton scattered disk and BLR radiation to explain the spectral break and also fit the quasi-simultaneous radio, optical, X-ray, and gamma-ray data of 2008 flare. Hunger and Reimer [123] used a particle distribution with a break to model the flare emission with Compton-scattered BLR radiation alone and also in combination with Compton-scattered disc emission. Kohler and Nalewajko [152] studied many short bright flares of blazars, including 3C 454.3. They concluded that the average Fermi-LAT spectrum is a superposition of many short-lived components with different spectral curvatures. In our work in many cases (see Table-3.30) Log-parabola function well represents the gamma-ray SEDs of flares.

While modelling the two flares Flare-2A and Flare-2D, we assumed the emission region was in the BLR region, which is commonly assumed in single zone SED modelling. However, for many flares, a more complicated and realistic scenario may be required to explain the temporal and spectral features. Due to its variable nature, this source should be monitored for high energy neutrino emission during its flaring states. High energy neutrinos can escape from the jets even if they are produced in the inner regions of jets. In this case, high-energy neutrinos may be detected without counterparts in high energy gamma-rays. More simultaneous multi-wavelength data and constraint on neutrino flux from the IceCube detector would be helpful to model the flares, constrain their hadronic jet power and locate the emission regions of the flares.

Table 3.1: Rising and Decay time [T_r (column 4) and T_d (column 5)] for given peak time [t_0 (column 2)] and peak flux [F_0 (column 3)] which is calculated by temporal fitting of light curve (Flare-1A) with sum of exponential function. Column 1 represent peak number. Here results are shown for 1 day binning.

Flare-1A

Peak	t_0 [MJD]	F_0 [10^{-6} ph cm^{-2} s^{-1}]	T_r [hr]	T_d [hr]
P1	54719.1	5.45±0.42	73.35±4.21	54.79±14.38
P2	54729.1	4.31±0.35	19.95±5.78	57.03±9.96
P3	54738.1	3.66±0.28	15.55±4.91	30.52±9.86

Table 3.2: All the parameters represented here are similar to the parameters of Table-3.1. Results (1 day binning) are shown for Flare-2A

Flare-2A

Peak	t_0 [MJD]	F_0 [10^{-6} ph cm^{-2} s^{-1}]	T_r [hr]	T_d [hr]
P1	55070.5	3.32±0.29	80.87±8.40	100.13±17.21
P2	55077.5	3.31±0.36	16.46±9.12	39.40±13.49
P3	55091.5	5.95±0.52	100.14±8.79	45.80±7.77
P2	55103.5	4.08±0.36	114.94±16.77	56.86±17.67

Table 3.3: All the parameters represented here are similar to the parameters of Table-3.1. Results (6 hour binning) are shown for Flare-2B

1st part of Flare-2B

Peak	t_0 [MJD]	F_0 [10^{-6} ph cm^{-2} s^{-1}]	T_r [hr]	T_d [hr]
P1	55154.9	7.48±1.24	7.30±2.38	36.74±3.77
P2	55163.1	9.69±1.41	51.81±3.13	23.60±4.48
P3	55165.1	9.69±0.99	7.13±2.81	11.34±3.91
P4	55167.9	22.86±1.48	19.36±1.51	12.85±1.90
P5	55170.4	18.70±1.24	19.46±2.75	9.96±1.20
P6	55172.1	14.56±1.21	13.19±2.04	93.62±3.90

2nd part of Flare-2B

Peak	t_0 [MJD]	F_0 [10^{-6} ph cm^{-2} s^{-1}]	T_r [hr]	T_d [hr]
P1	55178.4	8.73±1.04	11.94±1.79	16.73±4.63
P2	55180.4	7.85±0.95	12.29±5.32	14.71±5.85
P3	55182.6	8.48±0.98	18.86±6.58	9.59±3.04
P4	55185.1	7.68±0.87	27.05±5.76	67.89±5.56
P5	55195.1	8.52±0.83	37.47±3.88	61.49±3.49

Table 3.4: All the parameters represented here are similar to the parameters of Table-3.1. Results (6 hour binning) are shown for Flare-2C

Flare-2C

Flare-I

Peak	t_0 [MJD]	F_0 [10^{-6} ph cm^{-2} s^{-1}]	T_r [hr]	T_d [hr]
P1	55289.1	13.04±1.21	23.45±3.83	8.09±1.97
P2	55290.6	12.73±1.43	7.37±1.98	18.13±4.33
P3	55292.4	12.77±0.64	12.70±3.49	13.10±3.04
P4	55294.1	16.29±0.82	17.06±2.98	18.77±2.99
P5	55300.1	13.29±2.66	26.06±7.01	32.56±4.66

Flare-II

Peak	t_0 [MJD]	F_0 [10^{-6} ph cm^{-2} s^{-1}]	T_r [hr]	T_d [hr]
P1	55320.6	9.71±0.94	17.61±2.88	7.93±2.57
P2	55321.9	10.05±0.95	4.71±1.92	8.90±2.18
P3	55322.6	7.79±0.90	9.92±3.28	31.44±5.41
P4	55327.1	9.12±1.26	26.26±4.90	14.72±2.59
P5	55329.4	5.96±0.78	16.87±4.40	59.31±5.26

Table 3.5: All the parameters represented here are similar to the parameters of Table-3.1 . Results (6 hour binning) are shown for Flare-2D

Flare-2D				
Flare-I				
Peak	t_0 [MJD]	F_0 [10^{-6} ph cm^{-2} s^{-1}]	T_r [hr]	T_d [hr]
P1	55517.6	53.51±2.08	11.52±1.45	8.46±1.67
P2	55518.6	65.66±2.34	8.92±1.15	6.19±1.40
P3	55519.9	80.41±5.92	13.82±1.57	17.51±1.34
Flare-II				
Peak	t_0 [MJD]	F_0 [10^{-6} ph cm^{-2} s^{-1}]	T_r [hr]	T_d [hr]
P1	55541.6	16.12±1.29	82.92±4.83	33.91±4.07
P2	55544.9	19.41±1.25	12.21±2.50	37.04±8.23
P3	55549.9	22.12±1.39	43.56±6.03	25.18±3.92
P4	55551.9	20.02±1.31	10.00±3.45	21.92±4.61
P5	55563.1	13.44±1.56	12.20±5.34	10.20±4.54
P6	55566.9	18.22±1.53	41.75±5.33	57.73±3.23

Table 3.6: All the parameters represented here are similar to the parameters of Table-3.1. Results (6 hour binning) are shown for Flare-3A

Flare-3A				
Flare-I				
Peak	t_0 [MJD]	F_0 [10^{-6} ph cm^{-2} s^{-1}]	T_r [hr]	T_d [hr]
P1	56816.1	9.36±0.52	16.04±1.64	14.23±2.39
P2	56819.1	5.16±0.87	16.23±4.78	13.15±5.48
P3	56820.6	8.01±0.60	5.30±2.87	8.45±4.11
P4	56822.1	11.71±0.48	12.35±4.02	6.51±1.19
P5	56823.4	12.30±0.50	16.33±1.82	40.02±2.63
Flare-II				
Peak	t_0 [MJD]	F_0 [10^{-6} ph cm^{-2} s^{-1}]	T_r [hr]	T_d [hr]
P1	56827.1	9.27±1.03	5.17±1.23	4.87±1.30
P2	56830.9	11.60±0.43	50.68±3.20	8.25±1.05
P3	56831.6	12.20±0.50	5.46±0.78	14.07±3.94
P4	56833.1	8.90±0.88	11.37±5.28	3.50±1.77
P5	56834.4	11.02±1.16	7.97±2.15	38.00±2.28

Table 3.7: All the parameters represented here are similar to the parameters of Table-3.1. Results (6 hour binning) are shown for Flare-3B

Flare-3B

Peak	t_0 [MJD]	F_0 [10^{-6} ph cm^{-2} s^{-1}]	T_r [hr]	T_d [hr]
P1	57006.1	4.95±0.69	58.87±5.01	9.22±2.72
P2	57008.4	7.90±0.90	8.96±1.54	33.04±2.12

Table 3.8: All the parameters represented here are similar to the parameters of Table-3.1. Results (6 hour binning) are shown for Flare-4A

Flare-4A

Peak	t_0 [MJD]	F_0 [10^{-6} ph cm^{-2} s^{-1}]	T_r [hr]	T_d [hr]
P1	57197.4	4.75±0.72	5.02±1.36	5.40±1.53
P2	57198.6	7.58±0.79	4.52±0.86	3.16±0.73
P3	57199.9	5.64±0.74	3.65±1.17	4.80±1.08
P4	57204.6	10.82±0.46	9.88±0.79	9.44±0.88
P5	57206.6	9.21±0.43	6.68±0.99	10.59±0.97

Table 3.9: All the parameters represented here are similar to the parameters of Table-3.1. Results (6 hour binning) are shown for Flare-4B

Flare-4B

Peak	t_0 [MJD]	F_0 [10^{-6} ph cm^{-2} s^{-1}]	T_r [hr]	T_d [hr]
P1	57254.1	11.43±0.48	9.83±1.58	9.55±1.89
P2	57256.1	12.00±0.49	17.35±2.58	14.33±1.40

Table 3.10: All the parameters represented here are similar to the parameters of Table-3.1. Results (6 hour binning) are shown for Flare-4C

Flare-4C

Peak	t_0 [MJD]	F_0 [10^{-6} ph cm^{-2} s^{-1}]	T_r [hr]	T_d [hr]
P1	57401.4	5.15±0.83	19.75±6.27	8.96±2.39
P2	57402.9	5.49±0.80	9.56±2.57	24.49±4.33
P3	57407.1	7.44±0.94	32.60±4.33	12.08±2.10
P4	57408.9	5.44±0.83	4.16±1.71	13.26±3.50

Table 3.11: All the parameters represented here are similar to the parameters of Table-3.1. Results (6 hour binning) are shown for Flare-4D

Flare-4D

Peak	t_0 [MJD]	F_0 [10^{-6} ph cm^{-2} s^{-1}]	T_r [hr]	T_d [hr]
P1	57457.4	3.49±0.69	4.53±1.78	3.26±1.85
P2	57460.1	9.99±0.45	13.64±1.28	6.60±0.91

Table 3.12: All the parameters represented here are similar to the parameters of Table-3.1. Results (6 hour binning) are shown for Flare-5A

Flare-5A

Peak	t_0 [MJD]	F_0 [10^{-6} ph cm^{-2} s^{-1}]	T_r [hr]	T_d [hr]
P1	57558.1	14.37±1.82	5.49±1.47	3.56±1.39
P2	57558.9	10.60±1.66	2.83±1.35	8.12±2.62
P3	57561.1	12.41±1.66	15.37±2.74	7.81±2.20
P4	57562.4	19.19±1.29	4.06±0.83	4.87±1.13
P5	57563.6	20.23±1.30	9.79±1.54	11.74±0.58

Table 3.13: All the parameters represented here are similar to the parameters of Table-3.1. Results (6 hour binning) are shown for Flare-5B

Flare-5B

Peak	t_0 [MJD]	F_0 [10^{-6} ph cm^{-2} s^{-1}]	T_r [hr]	T_d [hr]
P1	57742.6	5.72±0.46	7.85±1.91	5.49±1.05
P2	57743.4	5.27±0.44	5.10±1.18	10.39±1.45

Table 3.14: Constant flux value for four Sub-structures

Sub-structures	Constant-Flux $F_{0.1-300Gev}$ [10^{-6} ph cm^{-2} s^{-1}]
Flare-4A	1.54±0.13
Flare-4B	1.79±0.23
Flare-4D	1.24±0.13
Flare-5A	0.52±0.07

Table 3.15: Results of variability time [t_{var} (column 5)] which is calculated by scanning the 6 hour binning γ-ray light curve for each flare. $\Delta\ t_{d/h}$ (column 6) is the redshift corrected doubling/halving time. Rise/Decay (column 7) represent the behaviour of the flux in a given time interval[T_{start} (column 1) and T_{stop} (column 2)]. Results are shown here from MJD 54728 - 55479.

$T_{start}(t_1)$ [MJD]	$T_{stop}(t_2)$ [MJD]	$[F(t_1)]$ [10^{-6} ph cm^{-2} s^{-1}]	$[F(t_2)]$ [10^{-6} ph cm^{-2} s^{-1}]	$\tau_{d/h}$ [hr]	$\Delta\ t_{d/h}$ [hr]	Rise/Decay
			Flare-1A			
54728.125	54728.375	2.37±0.60	5.22±0.77	2.63±0.98	1.41±0.53	R
54744.625	54744.875	1.55±0.34	3.10±0.50	3.00±1.18	1.61±0.63	R
54749.125	54749.375	2.77±0.52	1.27±0.32	-2.67±1.07	-1.44±0.57	D
54756.625	54756.875	1.78±0.40	0.87±0.34	-2.90±1.83	-1.56±0.98	D
			Flare-2A			
55055.375	55055.625	1.12±0.34	2.38±0.56	2.77±1.43	1.49±0.77	R
55061.875	55062.125	0.70±0.28	1.76±0.44	2.24±1.14	1.20±0.61	R
55063.625	55063.875	1.99±0.49	0.99±0.32	-2.97±1.75	-1.60±0.94	D
55064.875	55065.125	1.36±0.38	0.65±0.30	-2.79±2.04	-1.50±1.10	D
55068.125	55068.375	1.11±0.34	3.25±0.57	1.93±0.64	1.04±0.34	R
55110.875	55111.125	5.16±0.90	2.46±0.68	-2.80±1.24	1.51±0.67	R
55111.375	55111.625	4.73±0.76	2.32±0.52	-2.90±1.11	1.56±0.60	R
55118.625	55118.875	1.00±0.36	2.03±0.58	2.94±1.93	1.58±1.04	R
55129.625	55129.875	3.66±0.65	7.62±0.88	2.84±0.82	1.53±0.44	R
55129.875	55130.125	7.62±0.88	2.60±0.62	-1.94±0.48	1.04±0.26	R
55138.375	55138.625	1.18±0.37	2.75±0.53	2.46±1.07	1.34±0.57	R
			Flare-2B			
55138.125	55138.375	1.19±0.37	2.75±0.54	2.48±1.09	1.33±0.59	R
55143.375	55143.625	1.36±0.37	2.82±0.57	2.85±1.32	1.53±0.71	R
			Flare-2C			
55256.375	55256.625	3.59±0.64	1.47±0.59	-2.33±1.14	-1.25±0.61	D
55256.625	55256.875	1.47±0.59	3.23±0.66	2.64±1.51	1.42±0.81	R
55260.125	55256.375	2.64±0.52	1.16±0.39	-2.53±1.20	-1.36±0.64	D
55277.375	55277.625	1.94±0.54	3.98±0.10	2.89±1.12	1.55±0.60	R
55277.625	55277.875	3.98±0.10	1.92±0.51	-2.85±1.04	-1.53±0.56	D
55278.125	55278.375	1.73±0.46	3.78±0.72	2.66±1.11	1.43±0.60	R
55279.875	55280.125	3.83±0.83	1.83±0.46	-2.81±1.26	-1.51±0.68	D
55306.125	55306.375	8.56±0.92	4.14±0.12	-2.86±0.43	-1.54±0.23	D
55332.375	55332.625	5.23±0.72	2.52±0.51	-2.85±0.95	-1.53±0.51	D
			Flare-2D			
55452.375	55452.625	1.35±0.47	2.70±0.57	3.00±1.76	1.61±1.95	R
55455.125	55455.375	2.65±0.92	5.30±0.73	3.00±1.62	1.61±0.87	R
55459.375	55459.625	6.04±0.78	2.80±0.51	-2.70±0.78	-1.45±0.42	D
55468.625	55468.875	1.57±0.48	3.59±0.87	2.51±1.18	1.35±0.63	R
55475.875	55476.125	1.51±0.50	3.01±0.77	3.01±1.83	1.62±0.98	R
55478.625	55478.875	2.87±0.57	1.09±0.42	-2.14±0.96	-1.15±0.52	D
55478.875	55479.125	1.09±0.42	2.38±0.62	2.66±1.58	1.43±0.85	R

Table 3.16: All the parameters represented here are similar to the parameters of Table-3.15, but result are shown here from MJD 56808 - 57264.

$T_{start}(t_1)$ [MJD]	$T_{stop}(t_2)$ [MJD]	$Fluxstart[F(t_1)]$ [10^{-6} ph cm^{-2} s^{-1}]	$Fluxstop[F(t_2)]$ [10^{-6} ph cm^{-2} s^{-1}]	$\tau_{d/h}$ [hr]	$\Delta\ t_{d/h}$ [hr]	Rise/Decay
			Flare-3A			
56807.625	56807.875	1.03±0.34	3.32±0.59	1.78±0.57	0.96±0.31	R
56808.125	56808.375	2.12±0.51	4.46±1.08	2.79±1.28	1.50±0.69	R
56808.375	56808.625	4.46±1.08	1.78±0.52	-2.26±0.93	-1.21±0.50	D
56812.375	56812.625	1.44±0.57	3.95±0.87	2.06±0.92	1.11±0.50	R
56815.625	56815.875	2.63±0.71	8.95±0.48	1.70±0.38	0.91±0.20	R
56826.875	56827.125	3.58±0.60	9.28±1.03	2.18±0.46	1.17±0.25	R
56839.125	56839.375	6.28±0.79	2.94±0.78	-2.74±1.06	-1.47±0.57	D
56841.375	56841.625	2.21±0.65	5.77±0.74	2.17±0.72	1.17±0.41	R
56844.375	56844.625	1.10±0.41	2.32±0.52	2.79±1.62	1.87±0.87	R
56844.875	56845.125	2.31±0.63	4.78±1.01	2.86±1.36	1.54±0.73	R
56847.125	56847.375	2.11±0.95	4.99±1.30	2.41±1.46	1.30±0.73	R
			Flare-3B			
57013.625	57013.875	1.91±0.59	4.00±0.97	2.81±1.49	1.51±0.80	R
57013.875	57014.125	4.00±0.97	1.52±1.11	-2.15±1.70	-1.16±0.91	D
57014.125	57014.375	1.52±1.11	3.48±0.56	2.51±2.27	1.35±1.22	R
57019.375	57019.625	2.38±0.45	1.10±0.41	-2.69±1.46	-1.45±0.78	D
			Flare-4A			
57163.875	57164.125	0.65±0.24	1.68±0.43	2.19±1.04	1.18±0.56	R
57165.625	57165.875	1.19±0.43	0.57±0.26	-2.82±2.23	-1.52±1.20	D
57171.375	57171.625	2.59±0.67	1.28±0.40	-2.95±1.70	-1.59±0.91	D
57174.375	57174.625	1.73±0.60	4.33±0.69	2.27±0.94	1.22±0.50	R
57178.125	57178.375	0.62±0.27	1.61±0.51	2.18±1.23	1.17±0.66	R
57182.625	57182.875	1.35±0.45	0.60±0.28	-2.56±1.81	-1.38±0.97	D
57182.875	57183.125	0.60±0.28	1.59±0.43	2.13±1.18	1.14±0.63	R
57185.875	57186.125	3.03±0.59	1.26±0.43	-2.37±1.06	-1.27±0.57	D
57192.875	57193.125	1.47±0.48	3.38±0.74	2.50±1.18	1.34±0.63	R
57194.125	57194.375	2.12±0.56	0.94±0.41	-2.56±1.60	-1.38±0.86	D
57196.375	57196.625	1.25±0.55	2.93±0.69	2.44±1.43	1.31±0.77	R
57198.625	57196.875	7.59±0.79	3.34±0.59	-2.53±0.63	-1.36±0.34	D
57199.875	57200.125	5.64±0.74	2.02±0.61	-2.02±0.65	-1.09±0.35	D
57205.125	57205.375	6.80±0.71	2.52±0.65	-2.09±0.59	-1.12±0.32	D
57205.875	57206.125	2.19±0.61	4.64±0.81	2.77±1.21	1.49±0.65	R
57207.125	57207.375	6.96±0.46	2.74±0.80	-2.23±0.72	-1.20±0.39	D
			Flare-4B			
57263.875	57264.125	1.42±0.45	3.24±0.87	2.52±1.27	1.35±0.68	R
57264.375	57264.625	3.52±0.66	1.65±0.49	-2.74±1.27	-1.47±0.68	D

Table 3.17: All the parameters represented here are similar to the parameters of Table-3.15, but result are shown here from MJD 57397 - 57576.

$T_{start}(t_1)$ [MJD]	$T_{stop}(t_2)$ [MJD]	$Fluxstart[F(t_1)]$ [10^{-6} ph cm^{-2} s^{-1}]	$Fluxstop[F(t_2)]$ [10^{-6} ph cm^{-2} s^{-1}]	$\tau_{d/h}$ [hr]	$\Delta\ t_{d/h}$ [hr]	Rise/Decay
			Flare-4C			
57396.875	57397.125	3.16±0.82	1.13±0.53	-2.02±1.05	-1.09±0.56	D
57397.125	57397.375	1.13±0.53	3.07±0.72	2.08±1.09	1.12±0.59	R
57397.375	57397.625	3.07±0.72	1.23±0.55	-2.27±1.25	-1.22±0.67	D
57397.625	57397.875	1.23±0.55	3.56±0.78	1.96±0.92	1.05±0.49	R
57397.875	57398.125	3.56±0.78	1.76±0.70	-2.95±1.90	-1.59±1.02	D
57410.625	57410.875	1.39±0.48	3.02±0.64	2.68±1.40	1.44±0.75	R
57419.125	57419.375	2.94±0.58	1.42±0.42	-2.86±1.39	-1.54±0.74	D
57419.375	57419.625	1.42±0.42	2.95±0.77	2.84±1.53	1.53±0.82	R
57430.125	57430.375	1.42±0.40	3.19±0.58	2.57±1.06	1.38±0.57	R
			Flare-4D			
57460.625	57460.375	6.40±0.95	3.25±0.65	-3.07±1.13	-1.65±0.61	D
57463.125	57463.375	1.19±0.44	2.38±0.56	3.00±1.90	1.61±1.02	R
57464.625	57464.875	1.44±0.47	0.65±0.34	-2.61±2.03	-1.40±1.09	D
			Flare-5A			
57552.125	57552.375	2.32±0.62	5.42±1.05	2.45±0.95	1.32±0.51	R
57552.625	57552.875	5.77±0.70	2.93±0.51	-3.07±0.96	-1.65±0.52	D
57553.875	57554.125	3.80±0.56	1.90±0.51	-3.00±1.32	-1.61±0.71	D
57554.875	57555.125	3.27±0.53	1.49±0.77	-2.64±1.82	-1.42±0.98	D
57557.625	57557.875	4.32±1.15	13.55±2.00	1.82±0.48	0.98±0.26	R
57565.125	57565.375	3.75±0.38	1.49±0.25	-2.25±0.48	-1.21±0.26	D
57567.625	57567.875	2.20±0.50	0.88±0.34	-2.27±1.11	-1.22±0.60	D
57567.875	57568.125	0.88±0.34	1.90±0.49	2.70±1.63	1.45±0.88	R
57570.625	57570.875	1.14±0.35	3.68±0.62	1.77±0.53	0.95±0.28	R
57574.125	57574.375	3.12±0.65	1.55±0.49	-2.97±1.60	-1.60±0.86	D
57575.625	57575.875	1.25±0.44	2.68±0.52	2.73±1.44	1.47±0.77	R

Table 3.18: Result of SED for Flare-1A fitted with different models (Powerlaw, Logparabola and Broken-powerlaw). Column 1 represents the different periods of activity, column 2 and column 3 to column 4 represent Flux value (F_0 in units of 10^{-6} ph cm^{-2} s^{-1}) and spectral indices for different models respectively. Break energy (E_{break} in units of Gev) for Broken-powerlaw model is given in column 5. The goodness of fit (log of Likelihood = log($\mathcal{L}$)) is mentioned in column 6. Column 7 represents the difference in the goodness of fit w.r.t. powerlaw model (equation-3.6).

			Powerlaw			
Activity	F_0	Γ			-log($\mathcal{L}$)	
Flare	2.60±0.03	2.39±0.01	-	-	162999.70	-
Post-Flare	1.30±0.04	2.40±0.03	-	-	57805.94	-
			Logparabola			
Activity	F_0	α	β	-	-log($\mathcal{L}$)	Δ log($\mathcal{L}$)
Flare	2.50±0.04	2.31±0.02	0.07±0.01	-	162979.78	-19.92
Post-Flare	1.30±0.05	2.29±0.05	0.09±0.03	-	57799.58	-6.36
			Broken-Powerlaw			
Activity	F_0	Γ_1	Γ_2	E_{break}	-log($\mathcal{L}$)	Δ log($\mathcal{L}$)
Flare	2.60±0.04	2.29±0.02	2.73±0.06	1.02±0.03	162960.52	-39.18
Post-Flare	1.30±0.06	2.27±0.09	2.87±0.20	1.03±0.18	57797.77	-8.17

Table 3.19: All the parameters represented here are similar to the parameters of Table-3.17. Results are shown for Flare-2A.

			Powerlaw			
Activity	F_0	Γ			-log($\mathcal{L}$)	
Pre-Flare	1.30±0.05	2.42±0.04	-	-	50345.11	-
Flare	2.90±0.006	2.41±0.001	-	-	231037.12	-
			Logparabola			
Activity	F_0	α	β	-	-log($\mathcal{L}$)	Δ log($\mathcal{L}$)
Pre-Flare	1.20±0.05	2.25±0.05	0.18±0.04	-	50368.45	23.34
Flare	2.70±0.05	2.26±0.02	0.12±0.01	-	230979.32	-57.80
			Broken-Powerlaw			
Activity	F_0	Γ_1	Γ_2	E_{break}	-log($\mathcal{L}$)	Δ log($\mathcal{L}$)
Pre-Flare	1.20±0.07	2.23±0.09	3.11±0.24	0.91±0.16	50368.09	22.98
Flare	2.90±0.04	2.31±0.02	2.86±0.05	1.03±0.02	231038.29	1.17

Table 3.20: All the parameters represented here are similar to the parameters of Table-3.17. Results are shown for Flare-2B.

			Powerlaw			
Activity	F_0	Γ			-log($\mathcal{L}$)	
Pre-Flare	2.36±0.067	2.42±0.03	-	-	43514.22	-
Flare	7.4±0.065	2.30±0.008	-	-	238878.89	-
			Logparabola			
Activity	F_0	α	β	-	-log($\mathcal{L}$)	Δ log($\mathcal{L}$)
Pre-Flare	2.20±0.06	2.34±0.04	0.08±0.02	-	43507.63	-6.59
Flare	7.00±0.08	2.16±0.01	0.10±0.007	-	238755.82	-123.07
			Broken-Powerlaw			
Activity	F_0	Γ_1	Γ_2	E_{break}	-log($\mathcal{L}$)	Δ log($\mathcal{L}$)
Pre-Flare	2.10±0.09	2.23±0.04	2.87±0.11	0.91±0.04	43493.02	-21.2
Flare	7.10±0.07	2.16±0.01	2.70±0.03	1.00±0.02	238745.81	-133.08

Table 3.21: All the parameters represented here are similar to the parameters of Table-3.17. Results are shown for Flare-2C.

			Powerlaw			
Activity	F_0	Γ			-log($\mathcal{L}$)	
Pre-Flare	2.70±0.05	2.47±0.02	-	-	79966.93	-
Flare-I	8.61±1.8e-4	2.37±1.38e-5	-	-	198341.69	-
Flare-II	5.66±0.09	2.35±0.01	-	-	74663.22	-
Post-Flare	2.70±0.06	2.40±0.02	-	-	69581.59	-
			Logparabola			
Activity	F_0	α	β	-	-log($\mathcal{L}$)	Δ log($\mathcal{L}$)
Pre-Flare	2.6±0.05	2.36±0.02	1.12±0.02	-	79949.72	-17.21
Flare-I	7.94±0.01	2.22±0.001	0.102±0.0009	-	198270.76	-70.93
Flare-II	5.35±0.004	2.24±0.0008	0.07±0.0004	-	74650.18	-13.04
Post-Flare	2.5±0.08	2.23±0.04	0.12±0.02	-	69564.56	-17.03
			Broken-Powerlaw			
Activity	F_0	Γ_1	Γ_2	E_{break}	-log($\mathcal{L}$)	Δ log($\mathcal{L}$)
Pre-Flare	2.6±0.05	2.33±0.03	2.95±0.12	0.89±0.16	79952.88	-14.05
Flare-I	8.20±0.008	2.24±0.0004	2.71±0.002	0.99±0.0002	198278.75	-62.94
Flare-II	5.43±0.002	2.24±0.0001	2.63±0.008	1.02±0.0001	74651.10	-12.12
Post-Flare	2.60±0.06	2.27±0.03	2.92±0.13	1.10±0.20	69563.80	-17.79

Table 3.22: All the parameters represented here are similar to the parameters of Table-3.17. Results are shown for Flare-2D.

			Powerlaw			
Activity	F_0	Γ			-log($\mathcal{L}$)	
Pre-Flare	2.98±0.04	2.41±0.01	-	-	85950.62	-
Platue-I	6.40±0.07	2.33±0.01	-	-	145909.56	-
Flare-I	24.0±0.16	2.27±0.006	-	-	250597.83	-
Flare-II	13.0±0.09	2.29±0.007	-	-	241670.99	-
Platue-II	5.90±0.09	2.31±0.01	-	-	70434.36	-
Post-Flare	2.52±0.0003	2.39±0.00008	-	-	195003.71	-
			Logparabola			
Activity	F_0 [10^{-6} ph cm^{-2} s^{-1}]	α	β	-	-log($\mathcal{L}$)	Δ log($\mathcal{L}$)
Pre-Flare	2.78±0.07	2.25±0.02	0.13±0.01	-	85899.15	-51.47
Platue-I	6.20±0.07	2.22±0.01	0.08±0.009	-	145858.64	-50.92
Flare-I	22.0±0.24	2.12±0.01	0.105±0.006	-	250390.52	-207.31
Flare-II	13.0±0.10	2.19±0.01	0.08±0.006	-	241554.87	-116.12
Platue-II	5.70±0.10	2.23±0.02	0.06±0.01	-	70420.27	-14.09
Post-Flare	2.36±0.05	2.24±0.02	0.11±0.01	-	194890.83	-112.88
			Broken-Powerlaw			
Activity	F_0 [10^{-6} ph cm^{-2} s^{-1}]	Γ_1	Γ_2	E_{break} [Gev]	-log($\mathcal{L}$)	Δ log($\mathcal{L}$)
Pre-Flare	2.84±0.03	2.25±0.005	2.95±0.03	0.97±0.003	85899.23	-51.39
Platue-I	6.30±0.07	2.21±0.01	2.69±0.05	0.98±0.11	145859.93	-49.63
Flare-I	23.0±0.20	2.15±0.01	2.62±0.02	0.99±0.02	250424.69	-173.14
Flare-II	13.0±0.10	2.18±0.007	2.62±0.02	0.99±0.006	241557.40	-113.59
Platue-II	5.80±0.10	2.23±0.02	2.55±0.07	-1.01±0.27	70422.59	-11.77
Post-Flare	2.41±0.003	2.25±0.0006	2.89±0.003	1.01±0.0003	194888.67	-115.04

Table 3.23: All the parameters represented here are similar to the parameters of Table-13.17. Results are shown for Flare-3A.

			Powerlaw			
Activity	F_0	Γ			-log($\mathcal{L}$)	
Pre-Flare	2.25±0.02	2.27±0.005	-	-	36569.38	-
Flare-I	6.80±0.13	2.12±0.01	-	-	54645.77	-
Flare-II	7.20±0.12	1.99±0.01	-	-	63621.22	-
Post-Flare	3.65±0.004	2.21±0.0006	-	-	36381.77	-
			Logparabola			
Activity	F_0	α	β	-	-log($\mathcal{L}$)	Δ log($\mathcal{L}$)
Pre-Flare	2.06±0.02	2.10±0.01	0.09±0.006	-	36565.30	-4.08
Flare-I	6.10±0.02	1.92±0.003	0.09±0.001	-	54599.47	-55.30
Flare-II	6.80±0.12	1.81±0.02	0.08±0.009	-	63569.28	-51.94
Post-Flare	3.44±0.001	2.04±0.0003	0.10±0.0001	-	36367.85	-13.92
			Broken-Powerlaw			
Activity	F_0	Γ_1	Γ_2	E_{break}	-log($\mathcal{L}$)	Δ log($\mathcal{L}$)
Pre-Flare	2.10±0.03	2.11±0.008	2.58±0.03	0.98±0.005	36565.02	-4.36
Flare-I	6.50±0.13	1.99±0.02	2.42±0.04	1.08±0.03	54619.72	-26.05
Flare-II	6.90±0.13	1.82±0.02	2.25±0.04	1.02±0.10	63578.84	-42.38
Post-Flare	3.49±0.01	2.05±0.002	2.58±0.009	1.02±0.001	36367.92	-13.85

Table 3.24: All the parameters represented here are similar to the parameters of Table-3.17. Results are shown for Flare-3B.

			Powerlaw			
Activity	F_0	Γ			-log($\mathcal{L}$)	
Pre-Flare	2.30±0.0006	2.31±0.0001	-	-	20940.21	-
Flare	3.81±0.08	2.32±0.01	-	-	34862.33	-
Post-Flare	2.32±0.01	2.33±0.005	-	-	32768.08	-
			Logparabola			
Activity	F_0	α	β	-	-log($\mathcal{L}$)	$\Delta\log(\mathcal{L})$
Pre-Flare	1.95±0.004	1.99±0.002	0.20±0.001	-	20930.24	-9.97
Flare	3.67±0.009	2.18±0.002	0.11±0.001	-	34849.17	-13.16
Post-Flare	2.08±0.02	2.15±0.01	0.10±0.007	-	32761.89	-6.19
			Broken-Powerlaw			
Activity	F_0	Γ_1	Γ_2	E_{break}	-log($\mathcal{L}$)	$\Delta\log(\mathcal{L})$
Pre-Flare	2.06±0.02	2.06±0.004	2.96±0.02	0.98±0.002	20931.05	-9.16
Flare	3.71±0.01	2.18±0.001	2.76±0.006	0.99±0.0007	34850.98	-11.35
Post-Flare	2.13±0.02	2.16±0.004	2.70±0.02	1.01±0.002	32761.75	-6.33

Table 3.25: All the parameters represented here are similar to the parameters of Table-3.17. Results are shown for Flare-4A.

			Powerlaw			
Activity	F_0	Γ			-log($\mathcal{L}$)	
Pre-Flare	1.38±0.01	2.27±0.006	-	-	75077.06	-
Flare	3.26±0.004	2.32±0.0009	-	-	81537.39	-
Post-Flare	0.78±0.01	2.41±0.01	-	-	40656.04	-
			Logparabola			
Activity	F_0	α	β	-	-log($\mathcal{L}$)	$\Delta\log(\mathcal{L})$
Pre-Flare	1.28±0.005	2.08±0.004	0.12±0.002	-	75031.97	-45.09
Flare	3.08±0.007	2.17±0.002	0.10±0.001	-	81476.70	-60.69
Post-Flare	0.69±0.005	2.13±0.008	0.22±0.005	-	40617.67	-38.37
			Broken-Powerlaw			
Activity	F_0	Γ_1	Γ_2	E_{break}	-log($\mathcal{L}$)	$\Delta\log(\mathcal{L})$
Pre-Flare	1.31±0.04	2.10±0.03	2.71±0.08	1.01±0.02	75033.75	-43.31
Flare	3.14±0.02	2.18±0.003	2.72±0.01	0.99±0.002	81479.48	-57.91
Post-Flare	0.72±0.006	2.15±0.003	3.34±0.02	0.99±0.002	40616.82	-39.22

Table 3.26: All the parameters represented here are similar to the parameters of Table-3.17. Results are shown for Flare-4B.

			Powerlaw			
Activity	F_0	Γ			-log($\mathcal{L}$)	
Pre-Flare	2.13±0.005	2.31±0.001	-	-	39002.40	-
Flare	6.51±0.01	2.15±0.001	-	-	41130.59	-
Post-Flare	1.87±0.01	2.41±0.004	-	-	25474.42	-
			Logparabola			
Activity	F_0	α	β	-	-log($\mathcal{L}$)	Δ log($\mathcal{L}$)
Pre-Flare	1.95±0.001	2.13±0.0009	0.10±0.0004	-	38982.23	-20.17
Flare	5.68±0.01	1.87±0.002	0.14±0.001	-	41075.71	-54.88
Post-Flare	1.70±0.03	2.21±0.02	0.14±0.01	-	25452.96	-21.46
			Broken-Powerlaw			
Activity	F_0	Γ_1	Γ_2	E_{break}	-log($\mathcal{L}$)	Δ log($\mathcal{L}$)
Pre-Flare	2.01±0.001	2.17±0.0003	2.61±0.001	0.99±0.0002	38987.98	-14.42
Flare	5.96±0.02	1.94±0.001	2.58±0.006	1.08±0.001	41080.72	-49.87
Post-Flare	1.73±0.01	2.20±0.003	3.10±0.02	1.03±0.002	25450.76	-23.66

Table 3.27: All the parameters represented here are similar to the parameters of Table-3.17. Results are shown for Flare-4C.

			Powerlaw			
Activity	F_0	Γ			-log($\mathcal{L}$)	
Pre-Flare	2.90±0.12	2.33±0.39	-	-	21642.13	-
Flare	3.90±0.10	2.31±0.02	-	-	54879.34	-
Post-Flare	2.90±0.10	2.38±0.03	-	-	40934.47	-
			Logparabola			
Activity	F_0	α	β	-	-log($\mathcal{L}$)	Δ log($\mathcal{L}$)
Pre-Flare	2.70±0.12	2.17±0.05	0.12±0.03	-	21649.23	7.1
Flare	3.30±0.11	2.02±0.06	0.19±0.03	-	54834.23	-45.11
Post-Flare	2.80±0.10	2.29±0.05	0.07±0.03	-	40930.23	-4.24
			Broken-Powerlaw			
Activity	F_0	Γ_1	Γ_2	E_{break}	-log($\mathcal{L}$)	Δ log($\mathcal{L}$)
Pre-Flare	2.80±0.15	2.18±0.08	3.04±0.33	1.32±0.28	21647.54	5.41
Flare	3.70±0.12	2.10±0.04	2.91±0.12	0.92±0.12	54846.84	-32.50
Post-Flare	2.80±0.13	2.27±0.76	2.86±0.23	1.22±0.21	40927.71	-6.76

Table 3.28: All the parameters represented here are similar to the parameters of Table-3.17. Results are shown for Flare-4D.

			Powerlaw			
Activity	F_0	Γ			-log($\mathcal{L}$)	
Pre-Flare	1.20±0.10	2.45±0.07	-	-	17622.70	-
Flare	4.00±0.16	2.19±0.03	-	-	19422.69	-
Post-Flare	1.40±0.09	2.27±0.05	-	-	23233.62	-
			Logparabola			
Activity	F_0	α	β	-	-log($\mathcal{L}$)	Δ log($\mathcal{L}$)
Pre-Flare	1.20±0.10	2.26±0.11	0.19±0.08	-	17619.23	-3.47
Flare	3.80±0.16	2.04±0.05	0.09±0.02	-	19415.80	-6.89
Post-Flare	1.00±0.12	1.73±0.15	0.30±0.07	-	23216.66	-16.96
			Broken-Powerlaw			
Activity	F_0	Γ_1	Γ_2	E_{break}	-log($\mathcal{L}$)	Δ log($\mathcal{L}$)
Pre-Flare	1.2±0.02	2.29±0.008	3.17±0.06	1.003±0.005	17611.85	-10.85
Flare	3.80±0.19	2.04±0.06	2.69±0.19	1.30±0.27	19413.59	-9.1
Post-Flare	1.30±0.15	2.00±0.14	3.23±0.54	1.11±0.36	23222.49	-11.13

Table 3.29: All the parameters represented here are similar to the parameters of Table-3.17. Results are shown for Flare-5A.

			Powerlaw			
Activity	F_0	Γ			-log($\mathcal{L}$)	
Pre-Flare	0.69±0.01	2.60±0.01	-	-	25761.05	-
Flare	5.49±0.006	2.11±0.0005	-	-	80606.46	-
Post-Flare	1.78±0.004	2.28±0.001	-	-	25145.68	-
			Logparabola			
Activity	F_0	α	β	-	-log($\mathcal{L}$)	Δ log($\mathcal{L}$)
Pre-Flare	0.64±0.0009	2.49±0.001	0.07±0.0009	-	25744.39	-16.66
Flare	5.02±0.008	1.87±0.001	0.134±0.0008	-	80508.03	-98.43
Post-Flare	1.55±0.001	2.00±0.001	0.165±0.0006	-	25138.02	-7.66
			Broken-Powerlaw			
Activity	F_0	Γ_1	Γ_2	E_{break}	-log($\mathcal{L}$)	Δ log($\mathcal{L}$)
Pre-Flare	0.65±0.01	2.47±0.005	3.45±0.09	1.50±0.006	25741.78	-19.27
Flare	5.14±0.02	1.904±0.002	2.518±0.008	1.014±0.001	80518.44	-88.02
Post-Flare	1.53±0.008	1.95±0.002	2.79±0.008	0.828±0.001	25136.59	-9.09

Table 3.30: All the parameters represented here are similar to the parameters of Table-3.17. Results are shown for Flare-5B.

			Powerlaw			
Activity	F_0	Γ			-log($\mathcal{L}$)	
Pre-Flare	1.10±0.08	2.43±0.06	-	-	42871.64	-
Flare	3.10±0.07	2.31±0.02	-	-	113517.61	-
Post-Flare	2.00±0.10	2.45±0.05	-	-	41430.56	-
			Logparabola			
Activity	F_0	α	β	-	-log($\mathcal{L}$)	$\Delta\log(\mathcal{L})$
Pre-Flare	1.90±0.10	2.41±0.07	0.04±0.04	-	42871.02	0.62
Flare	3.00±0.07	2.20±0.03	0.97±0.20	-	113502.15	-15.46
Post-Flare	1.10±0.08	2.36±0.09	0.05±0.05	-	41430.13	-0.43
			Broken-Powerlaw			
Activity	F_0	Γ_1	Γ_2	E_{break}	-log($\mathcal{L}$)	$\Delta\log(\mathcal{L})$
Pre-Flare	1.10±0.10	2.35±0.24	2.60±0.23	0.793±0.265	42871.10	-0.54
Flare	3.10±0.07	2.21±0.03	2.77±0.14	1.271±0.306	113503.80	-13.81
Post-Flare	2.00±0.11	2.41±0.07	2.64±0.25	1.309±0.344	41430.21	-0.35

Table 3.31: Results of reduced-χ^2 value (column 2) for different spectral models (Powerlaw, Logparabola, Broken-powerlaw). Column 1 represents different flares activity.

Activity	Reduced-χ^2		
Flare-1A	Powerlaw	Log-parabola	Broken-Powerlaw
Flare	12.38	3.98	1.72
Flare-2A			
Flare	49.06	4.53	12.19
Flare-2B			
Flare	41.92	1.64	2.00
Flare-2C			
Flare-I	1796.62	0.37	122.61
Flare-II	11.05	0.19	1.32
Flare-2D			
Flare-I	129.60	1.76	16.99
Flare-II	43.70	0.62	6.23
Flare-3A			
Flare-I	15.13	1.18	5.64
Flare-II	24.86	2.82	3.02
Flare-3B			
Flare	5.65	4.06	2.60
Flare-4A			
Flare	8.07	0.60	1.33
Flare-4B			
Flare	12.04	0.54	2.15
Flare-4C			
Flare	241.71	2.80	31.62
Flare-4D			
Flare	1.09	0.61	0.31
Flare-5A			
Flare	47.71	1.05	6.60
Flare-5B			
Flare	4.48	0.14	0.61

Table 3.32: Results of multi-wavelength SED modelling which is shown in Figure-3.48 & Figure-3.49. 1st column represents the study of different cases (see text for more details). Time duration of the Flares is given in last column.

Different Cases	Parameters	Symbol	values	Time (days)
	Flare-2A			
	Spectral index of electron spectrum (LP)	α	2.00	
	Magnetic field in emission region	B	3.80 G	
	Temperature of BLR region	T'_{BLR}	2.0×10^4 K	95
	Phonton density of BLR region	U'_{BLR}	5.63 erg/cm^3	
	Temperature of Disk	T'_{Disk}	1.0×10^6 K	
	Phonton density of Disk	U'_{Disk}	1.48×10^{-5} erg/cm^3	
	Size of the emission region	R	3.0×10^{16} cm	
	Doppler factor of emission region	δ	27.5	
	Lorentz factor of the emission region	Γ	20	
	Power in the magnetic field	P_B	1.95×10^{46} erg/sec	
	Curvature index of electron spectrum	β	0.09	
Case-1	Min value of Lorentz factor of electrons	γ_{min}	5.5×10^1	
($\tau \sim R/c$)	Max value of Lorentz factor of electrons	γ_{max}	5.7×10^3	
	Power in the injected electrons	P_e	5.64×10^{45} erg/sec	
	Curveture index of electron spectrum	β	0.08	
Case-2	Min value of Lorentz factor of electrons	γ_{min}	4.5×10^1	
($\tau \propto E^{-0.5}$)	Max value of Lorentz factor of electrons	γ_{max}	5.3×10^3	
	Power in the injected electrons	P_e	6.74×10^{45} erg/sec	
	Flare-2D			
	Spectral index of electron spectrum (LP)	α	2.18	
	Magnetic field in emission region	B	2.30 G	
	Temperature of BLR region	T'_{BLR}	2.0×10^4 K	133
	Phonton density of BLR region	U'_{BLR}	5.63 erg/cm^3	
	Temperature of Disk	T'_{Disk}	1.0×10^6 K	
	Phonton density of Disk	U'_{Disk}	1.48×10^{-5} erg/cm^3	
	Size of the emission region	R	3.0×10^{16} cm	
	Doppler factor of emission region	δ	27.5	
	Lorentz factor of the emission region	Γ	20	
	Power in the magnetic field	P_B	7.14×10^{45} erg/sec	
	Curvature index of electron spectrum	β	0.09	
Case-1	Min value of Lorentz factor of electrons	γ_{min}	3.0×10^2	
($\tau \sim R/c$)	Max value of Lorentz factor of electrons	γ_{max}	1.15×10^4	
	Power in the injected electrons	P_e	1.54×10^{46} erg/sec	
	Curvature index of electron spectrum	β	0.14	
Case-2	Min value of Lorentz factor of electrons	γ_{min}	2.8×10^2	
($\tau \propto E^{-0.5}$)	Max value of Lorentz factor of electrons	γ_{max}	1.2×10^4	
	Power in the injected electrons	P_e	2.09×10^{46} erg/sec	

Table 3.33: Best fitted values of the parameters when Doppler factor is varying according to equation 3.15 to model the light curve of different types of flare peaks. Last column represents the range of values of the Doppler factor (δ) for each peak.

Type of flare peak	parameters				
	t_c	a_1	a_2	k	Range of δ
$(T_r \sim T_d)$	1.116	0.195	-0.205	47.36	42.60 - 47.20
$(T_r > T_d)$	1.364	0.07	-0.65	58.48	48.50 - 57.65
$(T_r < T_d)$	1.864	0.63	-0.58	30.39	28.60 - 43.20

Table 3.34: Best fitted values of the parameters when normalisation constant (l_0) is varying according to equation 3.16 to model the light curve of different types of flare peaks. 5th & 6th column represent the range of values of the normalisation constant (l_0) and injected power in electrons (P_e) for each peak respectively.

Type of flare peak	parameters					
	t_c	a_3	a_4	k	Range of $l_0(\times 10^{50})$	Range of $P_e(\times 10^{46} erg/s)$
$(T_r \sim T_d)$	1.116	0.586	-0.605	20.23	14.83 - 20.25	2.39 - 3.27
$(T_r > T_d)$	1.364	0.22	-2.00	36.69	21.00 - 38.95	3.39 - 6.27
$(T_r < T_d)$	1.861	1.43	-1.55	6.18	4.30 - 14.90	0.693 - 2.4

3.9 Chapter conclusions

Below, the essential aspects of chapter-3 are briefly highlighted -

- Five major flares have been identified in the ∼ nine years (2008 - 2017) gamma-ray light curve history of 3C 454.3.
- After scanning the light curve, the shortest variability timescale is found to be of hour scale, which is similar to other flaring FSRQs e.g., PKS 1510-089.
- The gamma-ray spectral energy distributions of the flares are, in most cases, best fitted with the Log-parabola function. A similar result was also found earlier for other FSRQs.
- The rise and decay times of γ-ray flares do not follow any particular trend; in some cases, they are equal, but in others, they are not.
- Flare-2D (MJD 55467-55600) is the most violent sub-structure in this source's nine-year light curve history with six different phases of activity: Pre-flare, Plateau-I, Flare-I, Flare-II, Plateau-II, and Post-flare.
- Time-dependent leptonic modelling of Flare-2A and Flare-2D have been done with multi-wavelength data. The magnetic fields required to model these flares are 3.8 Gauss and 2.3 Gauss, respectively, comparable to the magnetic fields found from SED modelling of other blazars, e.g., PKS 1510-089 and CTA 102. The jet powers required to model these flares are below the Eddington's luminosity of the source (L_{Edd}) - $(0.6 - 5) \times 10^{47}$ erg/sec).
- Time variation of the Doppler factor or the injected luminosity in electrons over short time scales can explain their light curves.

Chapter 4

Multi-wavelength study of 4C+28.07

4.1 Observational history

4C+28.07 is a FSRQ (Flat Spectrum Radio Quasars) type and moderately variable extra-galactic source with RA: 2h37m52.406s, DEC: +28d48m8.990s (Fey et al. [153]), located at redshift 1.206 (Shaw et al. [154]) frequently monitored by Fermi Large Area Telescope (Fermi-LAT) since 2008. It was observed in radio with Effelsberg 100 m and the IRAM 30 m telescope since January and June 2007. It reached a high state in radio in mid-2008, subsequently, the flux was decreasing until 2010 when the source reached the minima in radio flux (Nestoras et al. [155]). The Energetic Gamma Ray Experiment Telescope (EGRET) detected this source for the first time in high energy band ($>$ 100 MeV) with maximum flux of $(0.31{\pm}0.12){\times}10^{-6}$ photons cm^{-2} s^{-1}. Schinzel and Ciprini [156] reported the high flux state of this source with flux of $(1.4{\pm}0.3) \times 10^{6}$ photons cm$^{-2}s^{-1}$ on 3rd October, 2011 in γ-ray bands. This was an increase by a factor of 14 over the average flux of this source observed by Fermi-LAT during the first two years of the Fermi mission.

Swift observations on Oct 6 and Oct 9 of 2011 revealed an elevated level of X-ray and optical activity (Sokolovsky et al. [157]). 4C+28.07 was also detected with the Einstein Observatory Image Proportional Counter (IPC; 0.2-3.5 keV) in 1980. However, this detection in IPC may not be reliable. This source was observed on Dec 23 in 2013, when it was flaring in NIR. The observations were carried out by a 2.1m telescope of the Guillermo Haro Observatory (Carrasco et al. [158]). This source has also been continuously monitored in the 15 GHz radio band by the MOJVAE survey (Lister et al. [159]) since 1994. The maximum flux density at 15 GHz and maximum jet-speed were obtained as 5.11 Jy and 409$\pm$24 μas yr^{-1} between 1994 to 2019. The Fermi-GST AGN Multi-frequency Monitoring Alliance (F-GAMMA) program (Angelakis et al. [160], Fuhrmann et al. [161], Angelakis et al. [162]) provided the multi-frequency radio light curve (2.64 GHz to 43 GHz) of 4C+28.07 between 2007 and 2015, which was released in the second part of the F-GAMMA data-set [163]. Candidate Gamma-Ray Blazar Survey Source Catalog (CGRABS) recorded R band magnitude of 16.99 [164].

4.2 Data Analysis

4.2.1 Fermi-LAT Analysis

The Fermi-LAT data are extracted of FSRQ 4C+28.07 from FSSC's website data server [1] over the period of $\sim$ 12 years (August, 2008 - May, 2020) and analyzed it with the help of Fermi science tool software package version- 1.0.10, which includes galactic diffuse emission model (`gll_iem_v07.fits`) and extra galactic isotropic diffuse emission model (`iso_P8R3_SOURCE_V2_v1.txt`). Filter expression "`DATA_QUAL`>0 && `LAT_CONFIG`==1 && `ANGSEP`(`RA_SUN`,`DEC_SUN`,39.4684,28.8025)>15" is implemented to select the good time interval data and to avoid time bins when the Sun could be close to the target (less than 15°), which is recommended by the LAT team. We have further followed the same procedure as described in section-2.1.1 but with the latest 4FGL catalog.

[1] https://fermi.gsfc.nasa.gov/cgi-bin/ssc/LAT/LATDataQuery.cgi

4.2.2 Swift-XRT/UVOT

The archival data from the Swift X-ray Telescope (Swift-XRT) and Ultraviolet-Optical Telescope (UVOT) have also been used for the analysis. The data have been retrieved from HEASARC webpage[2] during the time span of same as γ-ray period, and total 12 observations were made. We use the neutral hydrogen column density of $n_H = 7.75 \times 10^{20} cm^{-2}$, provided in HEASARC webpage [3].

This source was also observed by the Swift Ultraviolet/Optical telescope (UVOT, Roming et al. [92]) in all the six filters: U, V, B, W1, M2, & W2. We have used these UVOT data in our multi-wavelength study.

4.2.3 Optical data

We have made use of publicly available archival data of Catalina surveys[4] and Steward Optical Observatory, Arizona [5] (Smith et al. [97]), which are a part of *Fermi* monitoring program. Catalina provides V-band photometric data. Steward observatory provides V and R band photometric and polarimetric data (Degree of polarization & Position angle).

We have collected all the available data of this source 4C+28.07 during MJD 54406 - 56590. There is no V & R band light curve data available in the Steward observatory website.

4.2.4 OVRO

We have also collected (MJD 54473 - 59109) publicly available data from the 40-meter ground-based telescope of Owens Valley Radio Observatory [6](OVRO; Richards et al. [96]), which regularly observe several blazars in the 15-GHz radio band as a part of Fermi-monitoring program.

[2]https://heasarc.gsfc.nasa.gov/cgi-bin/W3Browse/swift.pl
[3]https://heasarc.gsfc.nasa.gov/cgi-bin/Tools/w3nh/w3nh.pl
[4]http://nesssi.cacr.caltech.edu/DataRelease/
[5]http://james.as.arizona.edu/ psmith/Fermi/
[6]http://www.astro.caltech.edu/ovroblazars/

4.3 Flaring state in γ-ray light curves

We have analyzed the Fermi-LAT data of 4C+28.07 during MJD 54682 - 59000 ($\sim$ 12 yr) in 10 days binning and found three distinctive flaring states: Flare-A, Flare-B & Flare-C. These flaring states have been further analyzed in 3 days binning to study the different activity phases extensively. Figure-4.1 shows the 12-year light curve of this source with flaring and quiescent states in s different colors.

We have fitted each Flare phase with the equation-3.1 to compute the rising (T_r) & decay time (T_d).

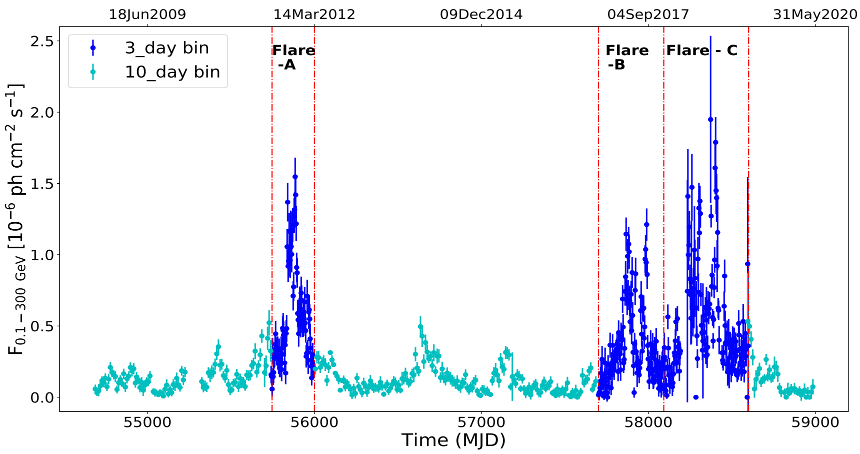

Figure 4.1: Fermi-LAT light curve of 4C+28.07 (MJD 54682 - 59000). Three major flaring states have been identified, which are shown by broken red line. Cyan and blue color represent the data in 10-day & 3-day binning respectively.

The Bayesian block representation to detect the different states of activity, which is based on Scargle et al. [165] algorithm and used before by several authors (e.g. Meyer et al. [166]).

4.3.1 Flare-A

A 3-day binning light curve of Flare-A is shown in Figure-4.2, which has three different phases, defined as Pre-flare, Flare & Post-flare.

The Pre-flare phase lasted for ∼ 80 days (MJD 55746-55835) with an average flux of 0.30±0.08. Subsequently, the source entered the flare phase with significant variation in flux, which lasted for ∼ 71 days (MJD 55835 - 55898). Figure-4.3 shows the fitted light curve of this Flare phase. We have identified two major peaks (P1 & P2) with fluxes of 1.37±0.13, 1.55±0.13 at MJD 55839.5 & 55884.5 respectively. The fitted parameters of the light curve have been described in Table-4.1.

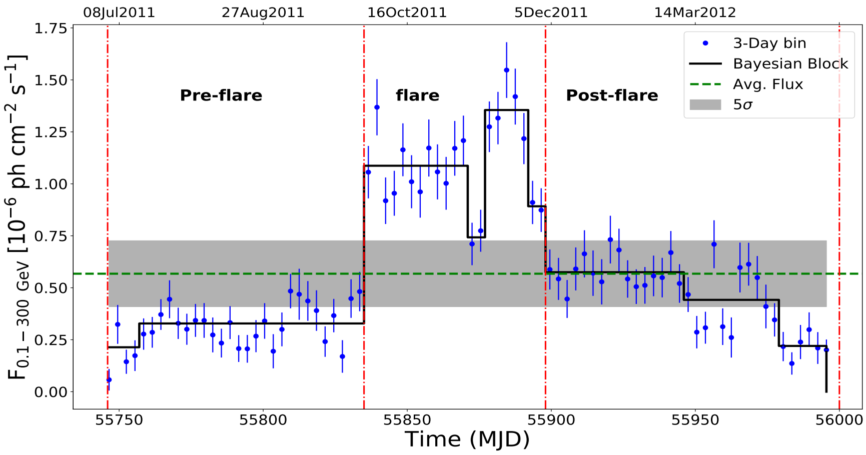

Figure 4.2: Three day binning light curve of Flare-A. Time duration of all the different periods of activities, which are shown by broken red line : MJD 55746-55835 (Pre-flare), MJD 55835-55898 (Flare) and MJD 55898-56000 (Post-flare).

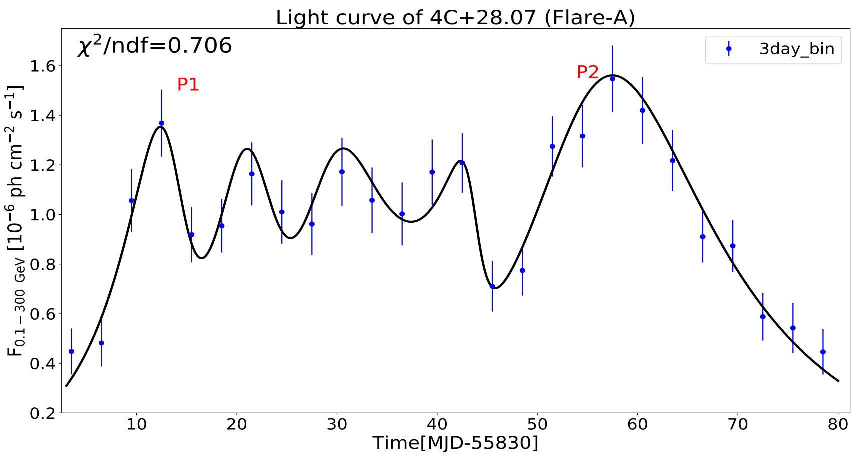

Figure 4.3: Fitted light curve of flare phase (Flare-A) with time span of 71 days (MJD 55835-55906).

4.3.2 Flare-B

Similar to Flare-A, a 3-day binning analysis has also been carried out for Flare-B, and four different phases have been observed. Figure-4.4 shows these phases, named as Pre-flare, Flare-B1, Flare-B2 & Post-flare.

The Pre-flare phase of Flare-B has a very small variation in flux with a time span of $\sim$ 132 days (MJD 57701 - 57859). Fitted light curve of flare-B1 & flare-B2 have been illustrated in Figure-4.5 & Figure-4.6 respectively. Flare-B1, consists of four major peaks (P1, P2, P3 & P4) at MJD 57866.5, 57881.5, 57902.5 & 57923.5 with fluxes of 1.14±0.12, 1.07±0.12, 0.84±0.11 & 0.87±0.11 respectively. After flare-B1 the source entered a low flux state which lasted around $\sim$ 27 days, and again rose to a high state, defined as flare-B2 (MJD 57952-57994). It has two distinctive peaks at MJD 57983.5, 57989.5. The Post-flare phase (MJD 57994-58092) has also been shown in Figure-4.4. The values of the fitted parameters have been elucidated in Table-4.2.

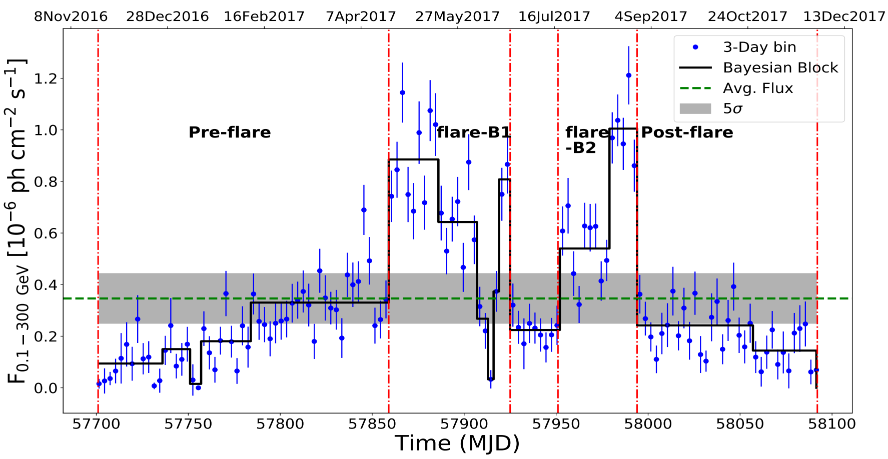

Figure 4.4: Three day binning light curve of Flare-B. Time duration of all the different periods of activities, which are shown by broken red line: MJD 57701-57859 (Pre-flare), MJD 57859-57925 (Flare-B1), MJD 57952-57994 (Flare-B2) and MJD 57994-58092 (Post-flare).

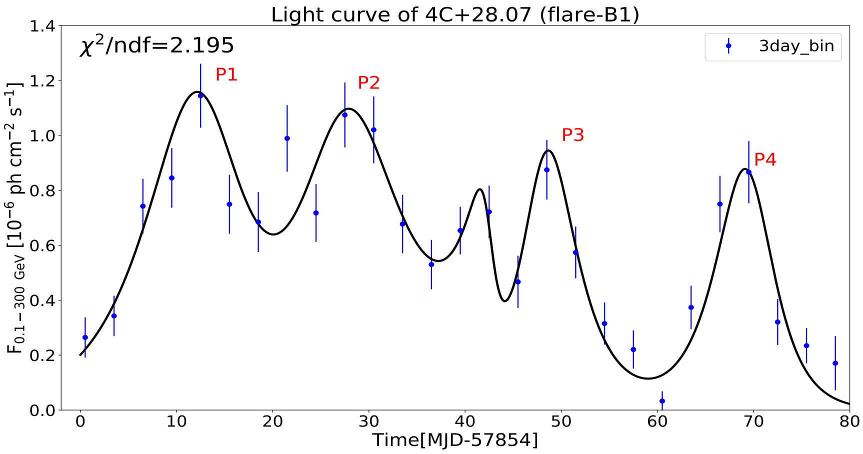

Figure 4.5: Fitted light curve of flare-B1 phase (Flare-B) with time span of 66 days (MJD 57859-57925).

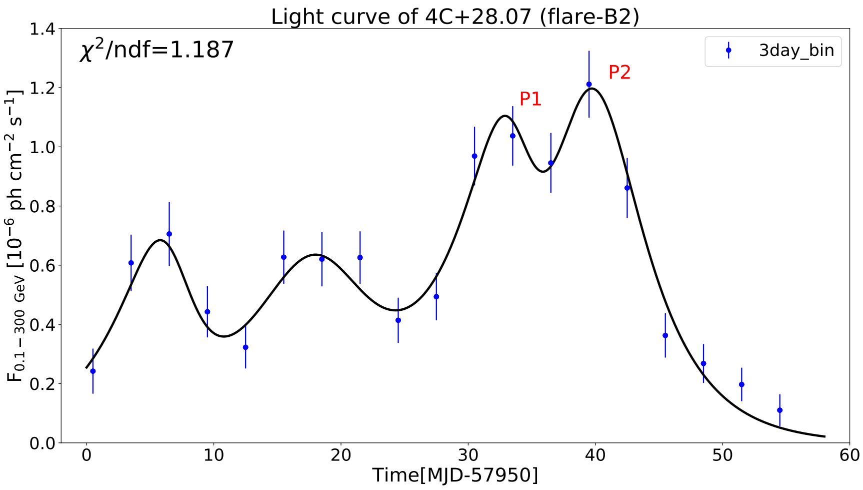

Figure 4.6: Fitted light curve of flare-B2 phase (Flare-B) with time span of 42 days (MJD 57925-57994).

4.3.3 Flare-C

Flare-C has only two phases: flare & Post-flare (shown in Figure-4.7). Due to irregularity and large error in the light curve data, we are unable to show the Pre-flare phase for this flaring state.

The fitted light curve of the Flare phase has been shown in Figure-4.8, which has two prominent peaks. One peak (P1) was observed at MJD 58372.5 with the flux of

1.95±0.57. This is the highest observed flux value over the 12 years period analyzed here. Another peak (P2) was found at MJD 58402.5. After this, the source came back to a low flux level and entered into the Post-flare phase (MJD 58422-58574) with an average flux of 0.33±0.08. The values of the fitted parameters are given in Table-4.3.

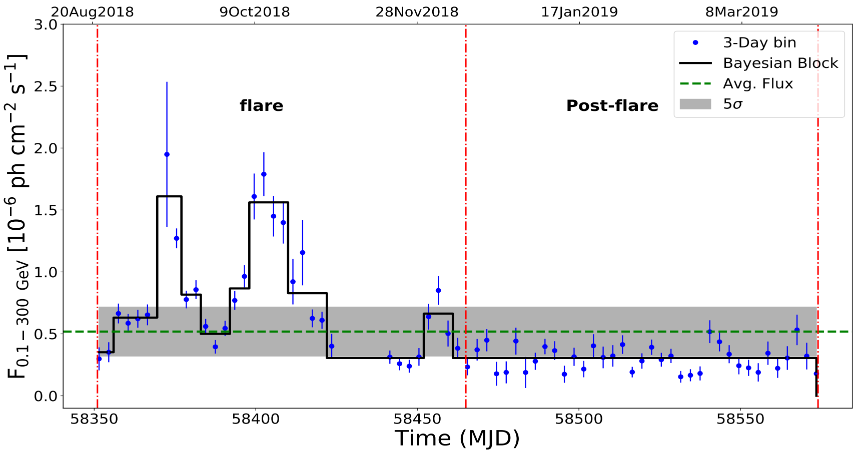

Figure 4.7: Three day binning light curve of Flare-C. Time duration of all the different periods of activities, which are shown by broken red line: MJD 58355-58422 (Flare) and MJD 58421-58574 (Post-flare).

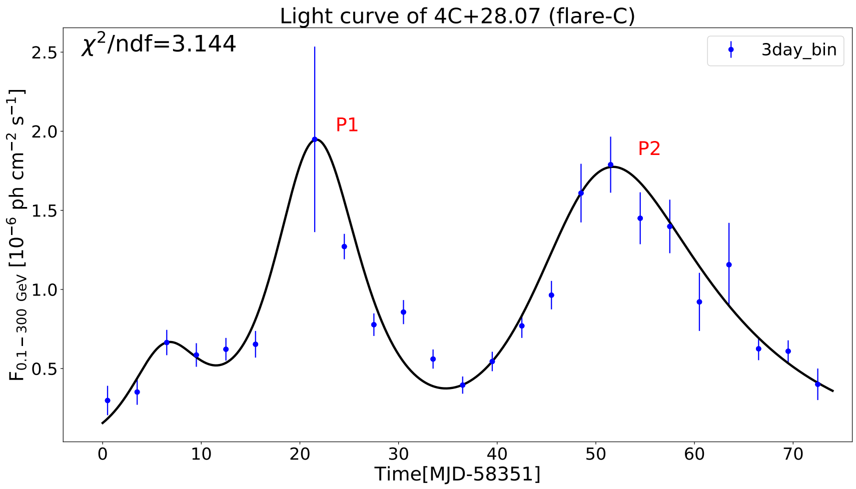

Figure 4.8: Fitted light curve of flare phase (Flare-C) with time span of 66 days (MJD 58355-58421).

4.4 γ-ray SED

The spectral analysis have been performed in γ-ray band for different phases (e.g. Pre-flare, Flare, Post-flare) of the flaring states and fitted these SED (Spectral Energy Distribution) with two different models [131]:

- A simple powerlaw model,

$$\frac{dN}{dE} = N_{PL}\left(\frac{E}{E_0}\right)^{-\Gamma_{PL}} \tag{4.1}$$

  In our study, we have fixed the value of scaling factor (E_0) at 100 Mev. N_{PL} & Γ_{PL} are the normalization and spectral index of the model respectively.

- A log-parabola model, given by,

$$\frac{dN}{dE} = N_{LP}\left(\frac{E}{E_s}\right)^{-(\alpha+\beta\log(E/E_s))} \tag{4.2}$$

  where, L_0, α, β are the normalization, photon and curvature index respectively. We have kept a fixed value of scaling factor (E_s) near the low energy part of the γ-ray SED (300 MeV).

We have fitted each SED of different phases with the above-mentioned models: PL (Power-law) and LP (Log parabola)

Figure-4.9 shows SEDs (Pre-flare, Flare, Post-flare) of Flare-A. Spectral index ('Γ_{PL}' in PL model) is constant during the change of Pre-flare to Flare phase. However, Γ_{PL} changes from 2.29±0.04 to 2.36±0.03 as the source transited from Flare to Post-flare phase, which is a sign of spectral hardening behavior. The fitted Parameters of different models have been elucidated in Table-4.4.

All the four phases of Flare-B show significant spectral hardening with increasing flux ($\Gamma_{PL} \propto F_0^{-1}$) value, which are illustrated in Figure-4.10. The detailed description of model parameters have been shown in Table-4.5.

Similar to other flaring states, SED of Flare-C also shows (shown in Figure-4.11) spectral hardening. When the source entered from Flare to Post-flare phase, its spectral index Γ_{PL} changed from 2.10±0.02 to 2.16±0.02. The modelling parameters has been described in Table-4.6.

The differences in log-likelihood values (equation-3.6) have also been given in the tables (Table-4.4 to Table-4.6) to compare the LP model with power-law model. Table-4.7 shows the reduced- χ^2 value for two different model. The value of $\Delta log(\mathcal{L})$ and the reduced- χ^2 suggest that the LP is better describing the γ-ray SED than PL.

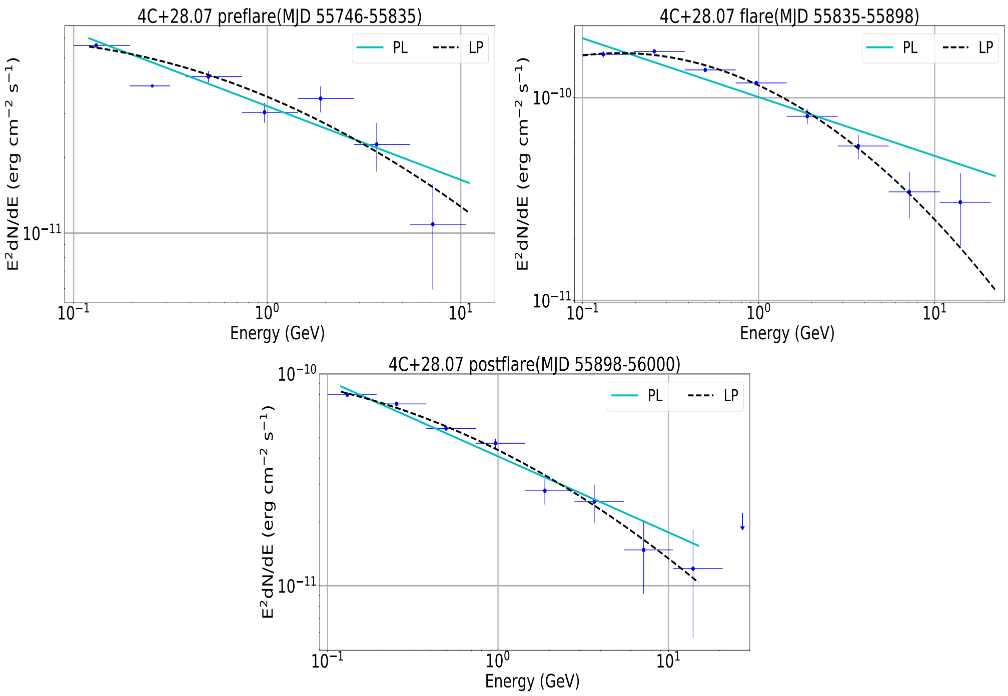

Figure 4.9: γ-ray SED of different periods of activity (Pre-flare, flare, Post-flare) of Flare-A. PL, LP describe the Powerlaw, Logparabola model respectively, which are fitted to data points.

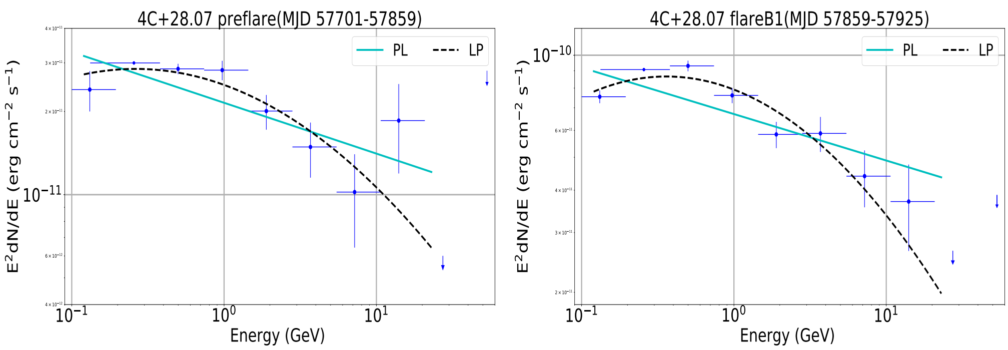

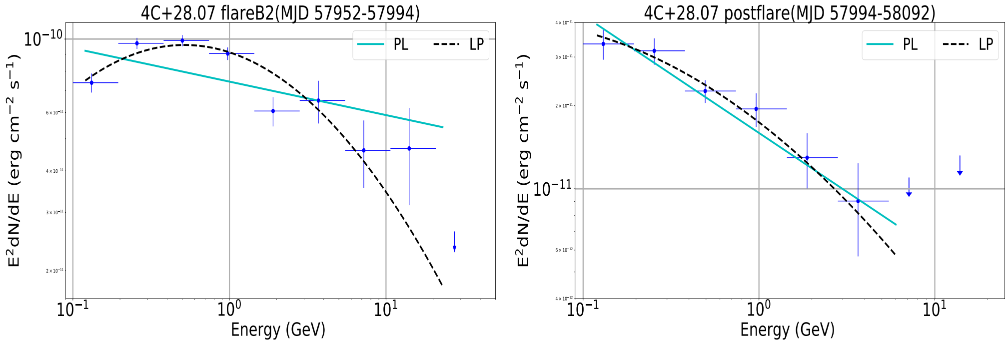

Figure 4.10: γ-ray SED of different periods of activity (Pre-flare, flare-B1, flare-B2, Post-flare) of Flare-B. PL, LP describe the Powerlaw, Logparabola model respectively, which are fitted to data points.

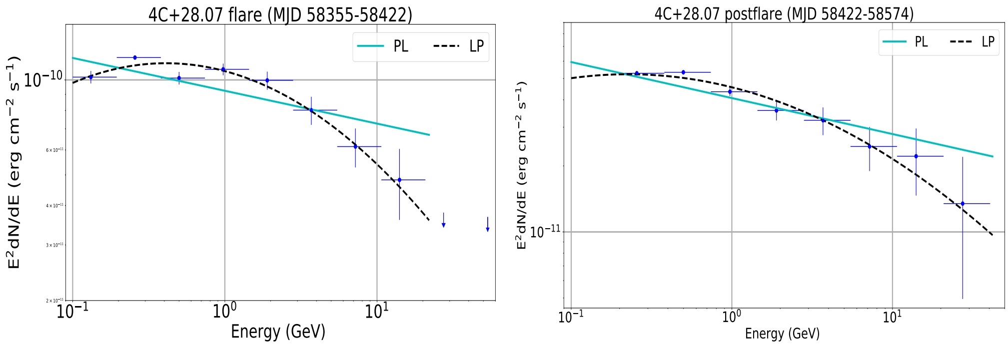

Figure 4.11: γ-ray SED of different periods of activity (flare, Post-flare) of Flare-C. PL, LP describe the Powerlaw, Logparabola model respectively, which are fitted to data points.

4.5 Multi-wavelength Study

4.5.1 Multi-wavelength light curve & correlation study

In this section, we have studied the multi-wavelength property (Light curve & SED) of 4C+28.07 in various bands. Figure-4.12 shows the multi-wavelength light curve of this source in γ-ray, X-ray, optical, and radio wavebands. SPOL- polarization & Position angle data are also shown in the fourth & fifth panel of the plot, and significant change is observed during all flaring state.

A correlation study between these light curves can give an idea about the location of different emission regions in the jet. For this purpose we have done zDCF (Discrete Correlation Function; Edelson and Krolik [167]) analysis. Unbinned Discrete Correlation

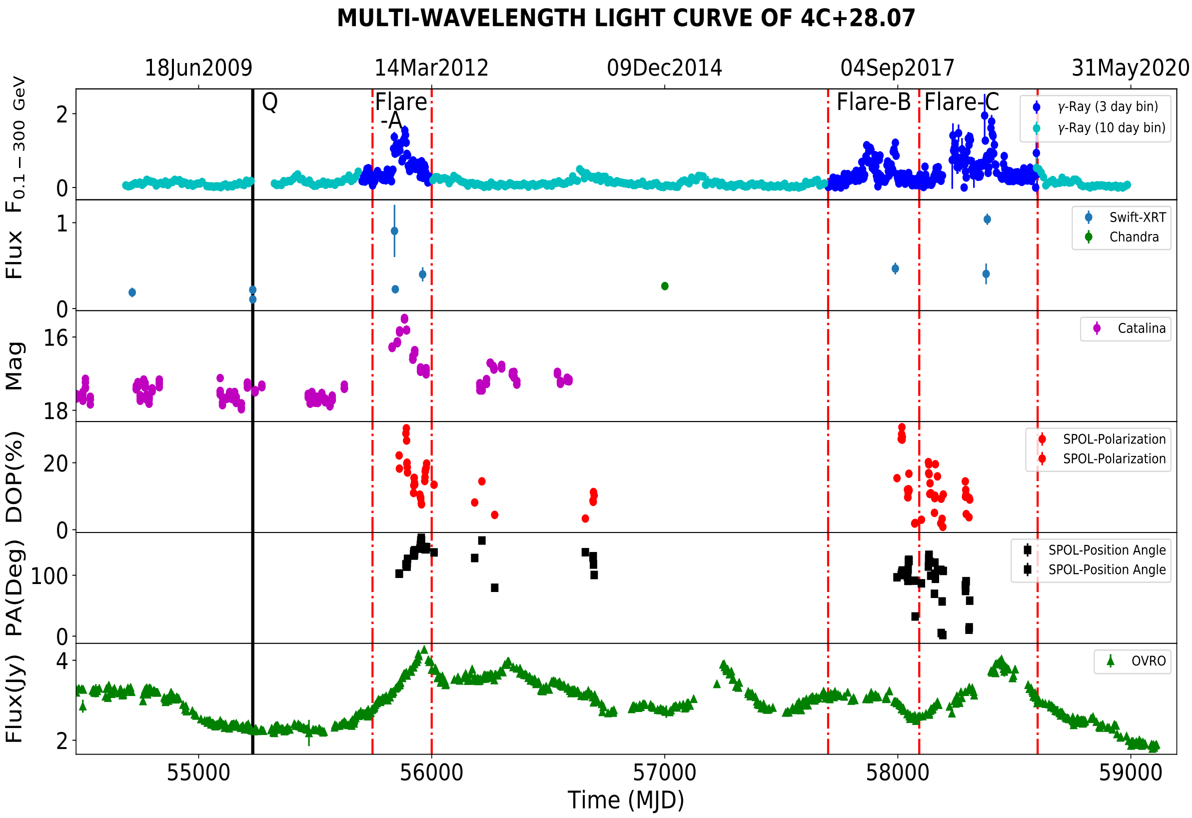

Figure 4.12: Multi-wavelength light curve of 4C+28.07. Top panel shows the Fermi-LAT data with 3 day & 10 day time bin. Swift-XRT & Chandra data are shown in second panel in units of 10^{-11} erg cm^{-2} s^{-1}.

Function (UDCF) is given by -

$$UDCF_{ij} = \frac{(a_i - < a >)(b_j - < b >)}{\sqrt{(\sigma_a^2 - e_a^2)(\sigma_b^2 - e_b^2)}} \tag{4.3}$$

where, a_i, b_j are the two discrete time series data sets. σ_a & σ_b are their standard deviations. If we bin the above quantity (UDCF$_{ij}$) over M number of pairs for which $\tau - \Delta\tau/2 \leq \Delta t_{ij} (= t_j - t_i) \leq \tau + \Delta\tau/2$, we will get the Discrete Correlation Function (DCF) -

$$DCF(\tau) = \frac{1}{M} UDCF_{ij} \pm \frac{1}{M-1} \sqrt{\sum [UDCF_{ij} - DCF(\tau)]^2} \tag{4.4}$$

Figure-4.13 and Figure-4.14 show the DCF plots between γ-ray & optical and γ-ray

& radio data respectively. Simultaneous γ-ray & optical (Catalina) data is available only for Flare-A. From Figure-4.13, we can see nearly zero time lag ($\sim$ 6 days) between γ-ray and optical light curves. However, between γ & radio bands, a significant time lag of $\sim$ 70 days is observed (shown in Figure-4.14a). For Flare-B, there are two distinct peaks in γ-ray, but no peaks in radio data, as shown in the multi-wavelength light curve in Figure-4.12. However, in the DCF plot of Flare-B (Figure-4.14b), only one significant peak ($> 95\%$) is observed at a time lag of $\sim$ -135 days, which is at the edge of the DCF or beyond one-third of the total time length of the worst time series [168], hence we did not consider this as a proper time lag between γ-ray & radio light curve. Thus no significant correlation between γ-ray & radio wavelength is found for Flare-B. In the γ-ray region, Flare-C has two distinctive peaks, whereas one clear peak is observed in the radio band. As a result, Figure-4.14c shows two peaks at time lag $\sim$35 & $\sim$134 days with DCF value of 0.58 & 0.63 respectively. We did not perform any X-ray correlation with other wavebands because of the lack of sufficient data points in the X-ray band.

To compute the significance of the DCF peaks, we have simulated 1000 γ-ray light curves using the method mentioned in Emmanoulopoulos et al. [169]. This method accounts for the general Probability distribution function (Log-normal) of the photon flux. We then computed the DCF between the simulated γ-ray data with optical & radio data, respectively. For each time lag 95% significant contour is shown in the DCF plots (Figure-4.13 - Figure-4.14).

Here, we have done a correlation study for the flaring states only. Earlier, Max-Moerbeck et al. [170] performed the correlation analysis for the same source along with several other sources for the first three years (2008 August 4 - 2011 August 12) of Fermi-LAT data and four years (2008 January 1 - 2012 February 26) of 15 GHz OVRO data set, though no significant correlation was found.

DCF plots suggest significant time lags between γ-ray & radio band for Flare-A & Flare-C. However, no correlation is observed for Flare-B. Flare-A & Flare-C consist of only one flaring phase, whereas Flare-B consists of two flaring phases (flare-B1 and flare-

B2) in its γ-ray light curve. Significant variability in flux is observed in the γ-ray band for different flaring phases, but no variation is observed in the low frequency (15 GHz radio band) region during this time interval.

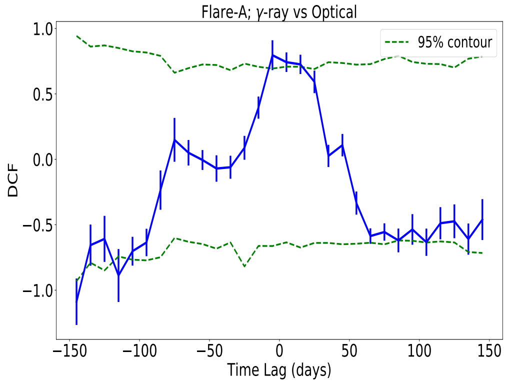

Figure 4.13: DCF plots between γ vs Optical data. 95 % contour is shown in green dashed line.

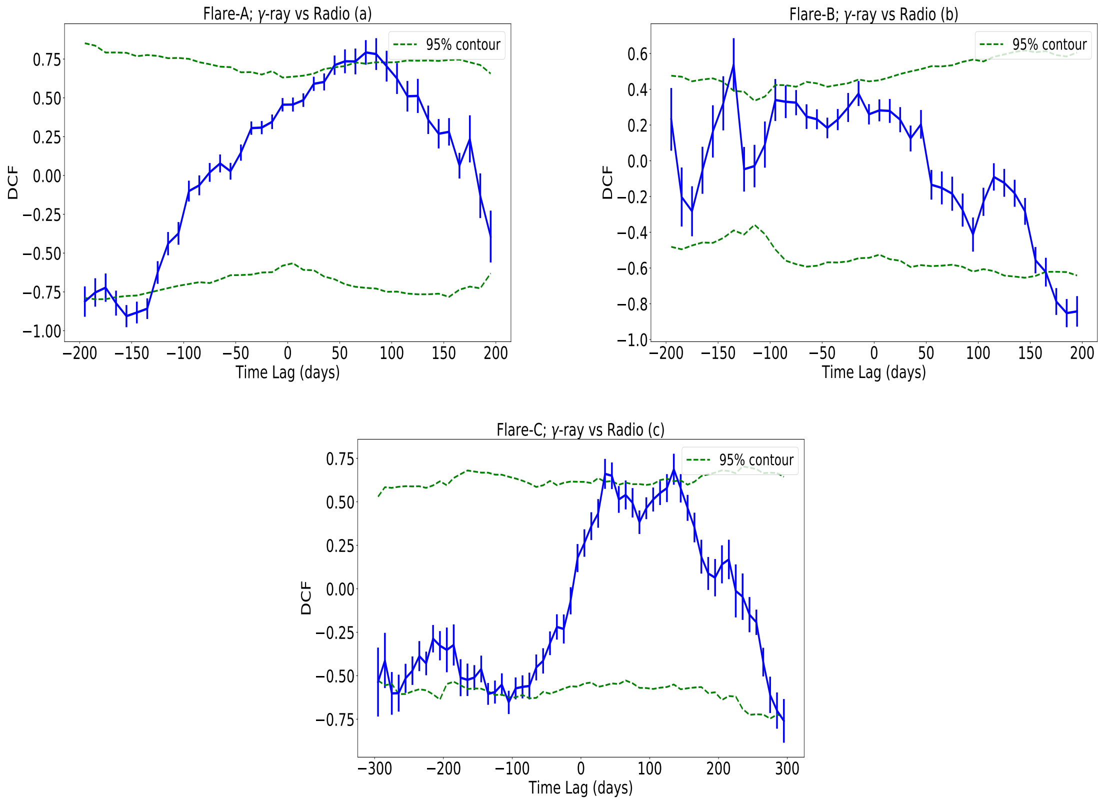

Figure 4.14: DCF plots between γ vs Radio data. 95 % contour is shown in green dashed line.

In our work, we have used a two-zone emission model to explain the multi-wavelength

SED (see 'Summary & Discussion' section). The inner blob (Blob-I) emits radiation via synchrotron, SSC (Synchrotron Self Compton) & EC (External Compton) processes and can explain the X-ray and γ-ray part of the spectrum, whereas the outer blob (Blob-II) contributes to the SED in radio & partially in X-ray frequency via synchrotron & SSC process respectively, as there are no external photons (from disk/BLR/DT) available for EC emission. The size of the BLR & DT region can be calculated by the simple scaling relations : $R_{BLR} \sim L^{0.5}_{Disk,45} \times 10^{17}$ cm and $R_{DT} \sim 2.5L^{0.5}_{Disk,45} \times 10^{18}$ cm (Ghisellini and Tavecchio [138]). We have approximated these sizes as $9.8{\times}10^{17}$ cm & $1.1{\times}10^{19}$ cm respectively. Blob-II is located beyond these regions (BLR & DT). Hence external seed photons from BLR and DT are not abundant at the location of Blob-II for EC emission.

4.5.2 Multi-wavelength modelling

We have modeled the multi-wavelength SED of 4C+28.07 with the publicly available code: 'GAMERA' [7] (Hahn [133]) which considers the time dependent spectral evolution while modelling the SED. This code computes the synchrotron and IC component of radiation by the given electron spectrum, $N(E, t)$. This $N(E, t)$ is calculated by solving the continuity equation-3.7 as described in section-3.6.2. 'GAMERA' uses the full Klein Nishina cross-section to compute the IC radiation (Blumenthal and Gould [135]). The log-parabolic functional form of $Q(E, t)$ is assumed to solve the transport equation as most of the γ-ray SED flaring states are best described by this model (Massaro et al. [134]), which are already discussed in chapter-3.

The value of Lorentz factor Γ is assumed to be 12.7 following Savolainen et al. [171]. Doppler factor (δ) of the jet is chosen as 25, which is a typical value for FSRQ type blazars (Liodakis et al. [172]; Pushkarev et al. [173]; Wu et al. [174]).

BLR & accretion disk photons are considered as seed photons to compute the EC emission component for only Blob-I. SSC components for both the blobs have also been estimated to model the source.

[7] http://joachimhahn.github.io/GAMERA

Energy density of BLR photons in the comoving frame of the jet is given by equation-3.9. BLR photon energy density to accretion disk photon energy density (ζ_{BLR}), assumed to be ~ 0.1. The radius of the BLR region, which is calculated by using the scaling relation (Ghisellini and Tavecchio [138]) - $R_{BLR} = 10^{17} L_{d,45}^{1/2}$. $L_{d,45}$ is the disk luminosity in unit of $10^{45} erg/sec$. From Celotti et al. [175], Maraschi and Tavecchio [176]; Zhang et al. [177] we can assume that accretion disk luminosity is approximately 10 times higher than the BLR luminosity ($L_{Disk} \sim 10 \times L_{BLR}$). In our study, we have taken the value of $L_{BLR} = 10^{45.39}$ erg/sec from Xiong and Zhang [178]. We have used the BLR temperature as 1.0×10^4 K (Dermer and Menon [139]).

The energy density of the disk photons at the location of Blob-I [139] is described by equation-3.10. The mass of the central engine ($M_{BH} \sim 10^{9.22} M_{\odot}$) is taken from Xiong and Zhang [178]. The distance between γ-ray emission region (Blob-I) and central engine of the system (Z), which is estimated to be 9.47×10^{17} cm using this equation $Z = \frac{2\Gamma^2 c t_{var}}{1+z}$, $t_{var} \sim 2.5$ days. Equation-3.10 gives the value of U'_{Disk} as 9.0×10^{-8} erg cm^{-3}. The values used in this work are $U'_{Disk} = 7.0 \times 10^{-8}$ erg cm^{-3} & $T'_{Disk} = 6.0 \times 10^4$ K, which are comparable to the values found for other FSRQs. The sharp fall in optical-UV region is explained by the direct disk emission.

Apart from these, we also constrain the radius of Blob-I (R'_I) in the jet frame by using the following relation -

$$R'_I \leqslant \frac{c t_{var} \delta}{1+z}. \tag{4.5}$$

The value of variability time (t_{var}) is used as ~ 2.5 days, which gives the upper limit of the emission region : $R_I \sim 4.7 \times 10^{16}$ cm. However, it is noted that the above formula is just an approximation & several effects that may introduce error in determining R_I (Protheroe [141]). We have used the radius of Blob-I as 2.0×10^{16} cm, which gives the best fit to the SED data. We have computed the distance between Blob-I & Blob-II by the following equation (Fuhrmann et al. [161]) -

$$\Delta r'_{I-II} = \frac{\beta_{app} c \Delta t_{obs}}{(1+z)\sin\theta}. \tag{4.6}$$

Where, $\beta_{app} = 18.8$ is the apparent speed of jet. Δt_{obs} & θ are the observed time lag & viewing angle of the source, respectively. Viewing angle is chosen as 3.4° ([179]). By using the above values, the computed values of Δr_{I-II} as 2.79×10^{19} cm and 1.30×10^{19} cm for flare phases of Flare-A and Flare-C. After that, we have calculated the radius of Blob-II under conical jet approximation, which gives the value of 1.44×10^{18} cm & 6.94×10^{17} cm for the above flare phases (Flare-A & Flare-C respectively). However, these high values of radii increase the required electron jet power in the emission region (Blob-II), and as a result, the total jet power exceeds the Eddington luminosity ($L_{edd} = 2.29 \times 10^{47}$ erg/sec) of the source. Hence, in our model, we used the optimum value of the Blob-II radius as 6.5×10^{17} cm for all the flares & quiescent state.

After constraining the above parameters, we have modelled all the multi-wavelength SEDs of flaring phases except flare-B1 (due to non-availability of simultaneous X-ray & optical-UV data) and one quiescent state, which are shown in Figure-4.15. We have also shown the non-simultaneous archival data with the cyan plus points. A pictorial representation of our model is shown with a cartoon diagram in Figure-4.16. This represents the case of Flare-A, where Blob-II is around 9 pc away from the SMBH, beyond the Dusty Torus (DT) region. For Flare-C though the situation is very similar, Blob-II is near the boundary of the DT.

There are several free parameters in our model, e.g: spectral index (α), curvature index (β) & normalization factor (l_0) of the injected log parabolic electron spectrum, minimum (e_{min}) & maximum (e_{max}) energy of the injected electrons, magnetic field (B) of the emission regions.

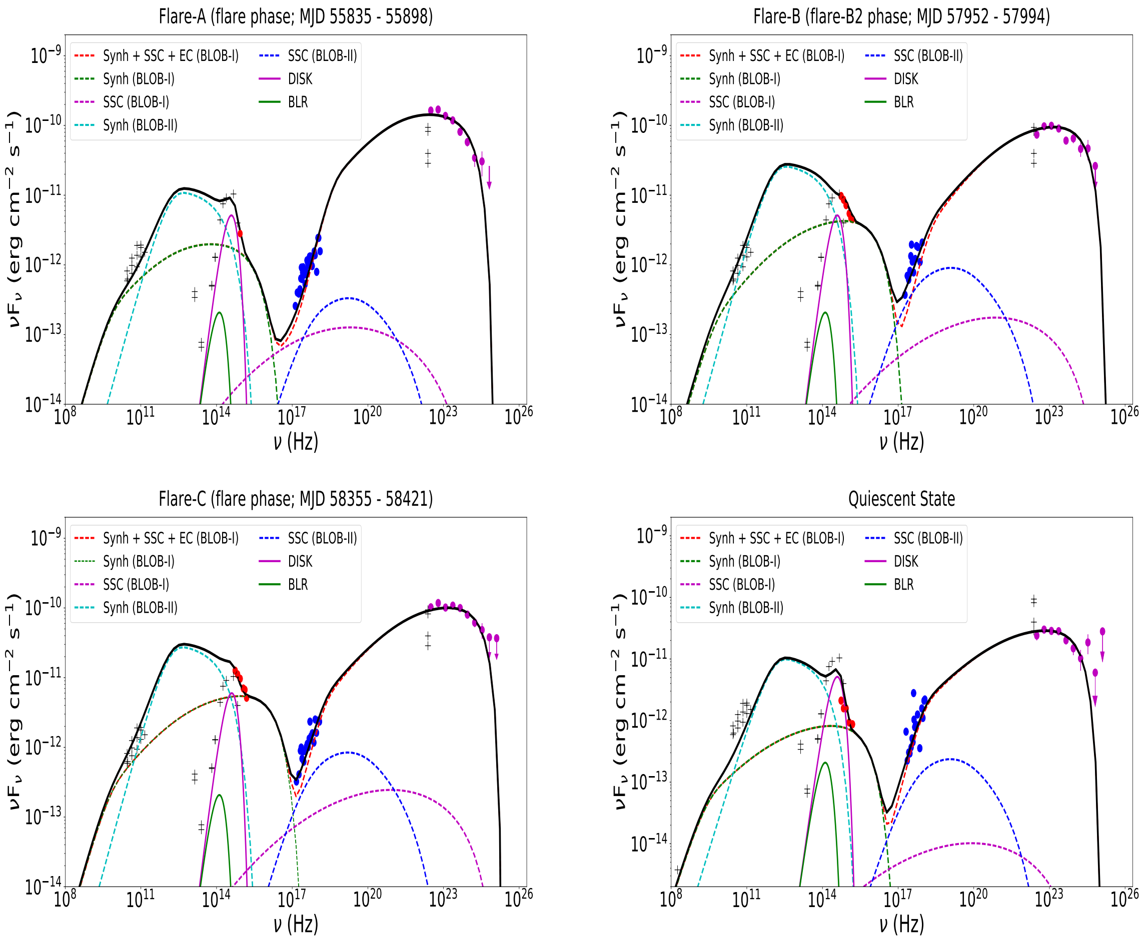

Figure 4.15: Two zone model fits of the multi-wavelength SEDs. Emission processes of Blob-I & Blob-II have been shown in different colors. Disk & BLR emission are also illustrated in solid magenta & green color respectively.

Total required jet power of both blobs are computed by the following equation -

$$P_{tot} = \pi\Gamma^2 c \sum_i R_i^2 (U'_{e,i} + U'_{B,i} + U'_{p,i}) \tag{4.7}$$

where, i runs over Blob-I and Blob-II. Energy density of electrons, magnetic field & cold protons in the co-moving frame are represented by U'_e, U'_B & U'_p respectively. Energy density of electrons and magnetic field are given by -

$$U'_{e,i} = \frac{3}{4\pi R_i^3} \int_{e_{min}}^{e_{max}} EQ_i(E)dE \tag{4.8}$$

and,

$$U'_{B,i} = \frac{B_i^2}{8\pi}. \tag{4.9}$$

$Q(E)$ is the injected electron (log-parabolic form for both blobs) spectrum in the jet -

$$Q(E) = l_0 \left(\frac{E}{E_{ref}} \right)^{-(\alpha + \beta \log(E/E_{ref}))} \tag{4.10}$$

l_0, α, β are the normalization factor, spectral & curvature index respectively. E_{ref} is the reference energy, which is fixed at 90.0 MeV. We have assumed, 10:1 ratio of the electron-positron pair and cold protons to compute the value of U'_p.

In our study, we have calculated the total required jet power of all the flaring states and one quiescent state and found the maximum value as 9.64×10^{46} erg sec^{-1} for Flare-A. The detailed description of multi-wavelength SED modelling parameters has been elucidated in Table-4.8.

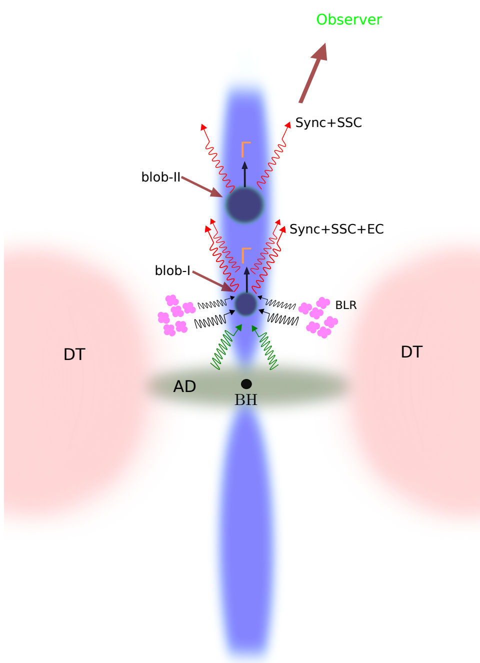

Figure 4.16: Schematic representation of two blob model in the jet used for the broad-band SED modeling. Image is not in scale. AD: Accretion Disk; BH: Black Hole; BLR: Broad Line Region; DT: Dusty Torus.

4.6 Summary and Discussion

The blazar 4C +28.07/BZQJ0237+2848 has not been studied before with multi-wavelength SED modelling. Here, we present the first comprehensive temporal and spectral study on this source.

We have analyzed the Fermi-LAT light curve of FSRQ 4C+28.07 in 10 days binning with a time span of $\sim$ 12 years (MJD 54682 - 59000) and found three distinct Flares: Flare-A, Flare-B & Flare-C. These Flares have been further analyzed in 3 days time bin, which is illustrated in Figure-4.1. Due to irregular & large error-bar in photon counts, we have restricted our analysis to 3 day binning only. In a three-day binned light curve, we have applied the Bayesian block method to identify the various phases within each flare. The following phases have been identified pre-flare, flare, and post-flare. The flux values above 5σ considered to be part of the high active phases e.g., flare-A, flare-B1, etc. We have also collected broadband data from various ground and space-based telescopes such as Swift, Steward, Catalina, and OVRO (15 GHz). In Swift-XRT, we do not have many observations, and hence we could not perform any temporal study. However, the spectrum from a few observations available during flare phases of Flare-A, Flare-B, and Flare-C is used for the broadband SED modeling.

This source has been included in the F-GAMMA program and observed in the frequency range of 2.64 GHz to 43 GHz between 2007 and 2015 (Angelakis et al. [163]). This source has also been monitored by the MOJAVAE survey (Lister et al. [159]) since 1994. We have used the OVRO data from (Richards et al. [96]) in the 15 GHz radio band, which covers the period of Fermi-LAT observations. We have performed the correlation study among various optical and radio band emission at 15 GHz with γ-ray. They show a very small time lag (order of a day) between γ-ray and optical emission with a very high correlation coefficient ($\sim$80%). However, a significant time lag of the order of $\sim$70 days and 35 days is observed between γ-ray and radio emission at 15 GHz for Flare-A and Flare-C with more than 60% significance. The Flare-B does not show any correlation between γ-ray with radio band emission. To model the broadband SED from radio to γ-ray for Flare-A and Flare-C, we have used two-zone emission model responsible for the radio and γ-ray emission separately. A cartoon diagram for the two-zone model is shown in Figure-4.16, though the image does not represent the correct relative scale. In Flare-A, these emission regions are separated by $\sim$9 pc and in Flare-C they are separated by $\sim$4 pc along the jet axis. Similar results were also observed in other FSRQ Ton 599 by Prince [180] where a separation of $\sim$5 pc was found between the γ-ray and radio band emission at 15 GHz. One way to explain the separation between γ-ray and radio emission could be the shock in the jet model (Marscher and Gear [181], Valtaoja et al. [182]). The delay in emission at a lower frequency can be caused by high opacity at the base of the jet under the shock in the jet model, and the synchrotron self-absorption can absorb the lower frequency emission. In shock in jet model, a shock is formed at the base of the jet where the jet is optically thick at the radio frequency but transparent for the high energy. So, the broadband emission produced at the base of the jet will be observed first at optical/γ-ray and later at the radio when the jet becomes optically thin for the radio emission. The connection between γ-ray, optical variability and parsec scale radio emission of 3C 345 was studied earlier (Schinzel et al. 183). The authors assumed that the emissions in radio, optical, and γ-ray frequencies are simultaneous. They suggested that the SSC mechanism could produce the γ-ray emission in a jet region extending up to $\sim$23 pc from the VLBI core, which is beyond the BLR and much more than one pc away from the central engine. We tried to fit our SED for 4C+28.07 with a single zone SSC model, where the emission zone is located outside the BLR, several parsecs away from the black hole. We found that it requires super-Eddington luminosity to fit the multi-wavelength data. Moreover, if we keep the blob size 2×10^{16} cm to explain the observed γ-ray variability, then we cannot fit the radio data.

A detailed discussion of radio follow-up of γ-ray emission from PKS 1510-089 at different radio frequencies are provided in Orienti et al. [184]. Two major γ-ray flares were detected from PKS 1510-089 in 2011 July and October. After 2011 September, a huge radio burst was also detected, first in millimeter, after some time delay in centimeter and also in decimetre wavelengths. This observation of radio emission suggests the formation of shock and its evolution due to expansion of emission region and radiative cooling of electrons.

The study done in Aleksić et al. [185] discusses the EC with infrared photons from dusty torus and also the spine-sheath model where the γ-ray emission region is placed at the radio core to explain the broadband SED. The authors suggested a common origin of millimeter radio and high energy γ-ray emission. In a more recent paper by H. E. S. S. Collaborationet al. [186], the authors discuss that the emission region of very high energy γ-rays from PKS 1510-089 is located 50 pc away from the black hole down the jet. During the γ-ray flare VLBI observations at 43 GHz revealed a fast-moving knot interacting with the standing jet feature. In their work, the very high energy γ-ray spectrum showed attenuation consistent with EBL absorption, which supports the speculation that the γ-rays are produced outside the BLR.

In our study of blazar 4C+28.07, there is neither any detection of very high energy γ-rays by MAGIC or HESS nor any detection of simultaneous radio knot emission. Therefore we cannot argue that the γ-ray and radio emissions originate from the same region several parsecs away from the black hole. Moreover, the BLR photons are not available there to efficiently produce γ-rays by EC mechanism. If there is a source of seed photons several parsecs away from the black hole or the radio emission were near the edge of the BLR, then one could argue in favour of a single zone emission model.

The above arguments suggest that multi-zone emission modeling is required to explain the broadband spectrum from radio to high energy γ-ray. Therefore, we consider the two emitting zones located at two different locations along the jet axis and separated by a distance of $\sim$ 9 pc for Flare-A and $\sim$ 4 pc for Flare-C.

For Flare-B, there is no variability observed in the radio band as compared to the γ-ray band. In this case, plasma instabilities could have prevented the production of significant radio emission that could relate to γ-ray activity up-stream, or another scenario was shown in Schinzel et al. 183, where γ-ray emission is shown to be produced at parsec scales along with the jet, as well as the presence of fast γ-ray variability, but this interpretation would further complicate a more simplistic two-zone model.

In subsection-4.5.2, we have discussed that the radius of the outer blob used in our work is smaller than the radius obtained from conical jet approximation. This is done under the assumption that the outer blob does not cover the entire cross-section of the conical jet. Otherwise the required jet power is very high. In Patel et al. [187] two-zone modeling has been done to explain orphan γ-ray flares from three FSRQs. There the first emission region is assumed to be the production site of γ-rays. This region is located near the dusty torus region for PKS 1510-089 and, 3C 279 and its radius is assumed to be smaller than the cross-section of the jet under conical jet approximation to explain the variability observed in the γ-ray data during orphan γ-ray flares.

The multi-zone emission modeling is done before also for many other blazars, where the high energy γ-ray emission could not be explained by single-zone emission model. A study by Cerruti et al. [188] on blazar PKS 1424+240 suggests that to explain the high energy γ-ray, the one zone emission model is not sufficient, and a very high Doppler factor above 250 is required in this case, which is unrealistic. Due to this reason, they have modelled the broadband SED with the two-zone emission model, which allows a reasonable value of Doppler factor, $\delta = 30$. A recent study of simultaneous γ-ray flare and neutrino event from TXS 0506+056 by Xue et al. [189] also indicates that two-zone emission model is required to explain the broadband SED and the emission of neutrino. In their model, one emitting zone is located close to the BLR, where the γ-rays and neutrinos are produced in pγ interaction of high energy protons with the BLR photons, and the second emission zone is responsible for the optical and X-ray emission through synchrotron and SSC (synchrotron self Compton).

We define an asymmetry parameter K (equation-3.17) for different peaks. In this work, we have found that 2 peaks have $T_r > T_d$ ($\zeta < -0.3$), 1 peak has $T_r < T_d$ ($\zeta > -0.3$) and 7 peaks have $T_r \sim T_d$ ($|\zeta| \leqslant 0.3$).

In Table-4.8, the parameter values for the two zone modelling are given. The total jet power required is always lower than the Eddington luminosity of this source 2.29×10^{47} erg/sec.

Table 4.1: The value of peak time (t_0) & peak flux (F_0) are given in column 2 & column 3 respectively. column 4 & column 5 represent the rising (T_r) & decay time (T_d). Here, results are shown for 3 day binning light curve (Flare-A).

Flare-A				
Peak	t_0 [MJD]	F_0 [10^{-6} ph cm^{-2} s^{-1}]	T_r [day]	T_d [day]
P1	55839.5	1.37±0.13	5.64±0.44	1.41±0.32
P2	55884.5	1.55±0.13	3.67±0.51	2.37±0.60

Table 4.2: All the mentioned parameters are same as Table-4.1

Flare-B				
flare-B1				
Peak	t_0 [MJD]	F_0 [10^{-6} ph cm^{-2} s^{-1}]	T_r [day]	T_d [day]
P1	57866.5	1.14±0.12	5.24±0.62	3.89±1.37
P2	57881.5	1.07±0.12	4.02±1.59	5.58±2.74
P3	57902.5	0.84±0.11	2.05±0.70	3.08±0.55
P4	57923.5	0.87±0.11	3.00±0.46	2.42±0.43
flare-B2				
P1	57983.5	1.04±0.10	5.22±1.16	1.48±0.47
P2	57989.5	1.21±0.11	2.77±0.40	1.17±0.28

Table 4.3: All the mentioned parameters are same as Table-4.1

Flare-C				
Peak	t_0 [MJD]	F_0 [10^{-6} ph cm^{-2} s^{-1}]	T_r [day]	T_d [day]
P1	58372.5	1.95±0.57	5.15±0.45	11.23±0.81
P2	58402.5	1.79±0.18	4.10±0.61	3.93±0.76

Table 4.4: Result of γ-ray SEDs for Flare-A, which are fitted with different models: PL and LP (see text for more details). Column 1 represents the different periods of activity, column 2 and column 3 to column 5 represent the total Flux (F_0) during the activity and parameters of different models respectively. The goodness of fit ($log(\mathcal{L})$) is mentioned in column 6. Column 7 represents the difference in the goodness of fit compared to PL model (equation-3.6).

			Powerlaw			
Activity	F_0 [10^{-6} ph cm^{-2} s^{-1}]	Γ_{PL}			-log($\mathcal{L}$)	
Pre-flare	0.28±0.01	2.29±0.04	-	-	195076.01	-
Flare	0.98±0.002	2.29±0.04	-	-	201995.31	-
Post-flare	0.43±0.02	2.36±0.03	-	-	228257.65	-
			Logparabola			
Activity	F_0 [10^{-6} ph cm^{-2} s^{-1}]	α	β	-	-log($\mathcal{L}$)	Δ log($\mathcal{L}$)
Pre-flare	0.27±0.02	2.20±0.07	0.05±0.02	-	195074.42	-1.59
Flare	0.94±0.02	2.14±0.03	0.11±0.02	-	201969.99	-25.32
Post-flare	0.42±0.02	2.28±0.05	0.05±0.02	-	228255.26	-2.39

Table 4.5: All the described parameters are same as Table-4.4, but for Flare-B.

			Powerlaw			
Activity	F_0 [10^{-6} ph cm^{-2} s^{-1}]	Γ_{PL}			-log($\mathcal{L}$)	
Pre-flare	0.18±0.01	2.18±0.04	-	-	318041.29	-
flare-B1	0.53±0.01	2.14±0.02	-	-	277904.79	-
flare-B2	0.55±0.02	2.10±0.02	-	-	163365.33	-
Post-flare	0.20±0.01	2.43±0.06	-	-	196929.05	-
			Logparabola			
Activity	F_0 [10^{-6} ph cm^{-2} s^{-1}]	α	β	-	-log($\mathcal{L}$)	Δ log($\mathcal{L}$)
Pre-flare	0.17±0.01	2.02±0.07	0.07±0.03	-	318036.96	-3.33
flare-B1	0.50±0.01	1.97±0.04	0.08±0.01	-	277887.31	-17.48
flare-B2	0.51±0.02	1.87±0.04	0.12±0.02	-	163345.13	-20.02
Post-flare	0.19±0.01	2.32±0.09	0.07±0.04	-	196927.64	-1.41

Table 4.6: All the described parameters are same as Table-4.4, but fot Flare-C.

			Powerlaw			
Activity	F_0 [10^{-6} ph cm^{-2} s^{-1}]	Γ_{PL}			-log($\mathcal{L}$)	
Flare	0.68±0.02	2.10±0.02	-	-	271738.69	-
Post-flare	0.31±0.01	2.16±0.02	-	-	334160.84	-
			Logparabola			
Activity	F_0 [10^{-6} ph cm^{-2} s^{-1}]	α	β	-	-log($\mathcal{L}$)	Δ log($\mathcal{L}$)
Flare	0.64±0.02	1.95±0.03	0.07±0.01	-	271719.74	-18.95
Post-flare	0.30±0.01	2.03±0.05	0.06±0.02	-	334154.53	-6.31

Table 4.7: Results of reduced-χ^2 value (column 2) for different spectral models (Powerlaw and Logparabola). Column 1 represents different flares activity.

Activity	Reduced-χ^2	
	Powerlaw	Log-parabola
Flare-A		
flare	16.75	2.02
Flare-B		
flare-B1	8.03	1.71
flare-B2	8.48	1.84
Flare-C		
flare	9.28	2.74

Table 4.8: Results of multi-wavelength SED modelling. 1st column represents the study of different periods. The values of the different parameters for Blob-I and Blob-II are given in column-4 and column-5 respectively (see text for more details).

Activity	Parameters	Symbol	BLOB-I	BLOB-II
	Temperature of BLR region	T'_{BLR}	1.0×10^4 K	$\times$
	Phonton density of BLR region	U'_{BLR}	4.28 erg/cm^3	$\times$
	Temperature of Disk	T'_{Disk}	6.0×10^4 K	$\times$
	Phonton density of Disk	U'_{Disk}	7.0×10^{-8} erg/cm^3	$\times$
	Size of the emission region	R	2.0×10^{16} cm	6.5×10^{17} cm
	Doppler factor	δ	25	25
	Lorentz factor	Γ	12.7	12.7
flare-A (71 days)	Spectral index	α	1.90	1.82
	Curvature index	β	0.15	0.15
	Min energy of electrons	e_{min}	3.58 MeV	148 MeV
	Max enrgy of electrons	e_{max}	4854 MeV	3321 MeV
	Magnetic field	B	1.20 G	0.25 G
	Power in the injected electrons	P_e	0.71×10^{46} erg/sec	5.86×10^{46} erg/sec
	Power in the magnetic field	P_B	0.03×10^{46} erg/sec	1.59×10^{46} erg/sec
	Total required jet power	P_{tot}	1.61×10^{46} erg/sec	8.03×10^{46} erg/sec
flare-B2 (42 days)	Spectral index	α	1.77	2.01
	Curvature index	β	0.11	0.06
	Min energy of electrons	e_{min}	2.4 MeV	135.9 MeV
	Max enrgy of electrons	e_{max}	7562.8 MeV	3321.5 MeV
	Magnetic field	B	2.1 G	0.14 G
	Power in the injected electrons	P_e	0.37×10^{46} erg/sec	6.59×10^{46} erg/sec
	Power in the magnetic field	P_B	0.11×10^{46} erg/sec	0.50×10^{46} erg/sec
	Total required jet power	P_{tot}	0.88×10^{46} erg/sec	7.79×10^{46} erg/sec
flare-C (66 days)	Spectral index	α	1.80	2.01
	Curvature index	β	0.10	0.06
	Min energy of electrons	e_{min}	2.45 Mev	148.2 Mev
	Max enrgy of electrons	e_{max}	8176.0 MeV	3321.5 MeV
	Magnetic field	B	2.3 G	0.15 G
	Power in the electrons	P_e	0.44×10^{46} erg/sec	6.03×10^{46} erg/sec
	Power in the magnetic field	P_B	0.13×10^{46} erg/sec	0.57×10^{46} erg/sec
	Total required jet power	P_{tot}	1.06×10^{46} erg/sec	7.20×10^{46} erg/sec
Quiescent State (3 days)	Spectral index	α	1.90	2.01
	Curvature index	β	0.08	0.06
	Min energy of electrons	e_{min}	1.84 MeV	163.5 MeV
	Max enrgy of electrons	e_{max}	5110.0 MeV	3066.0 MeV
	Magnetic field	B	1.7 G	0.10 G
	Power in the electrons	P_e	1.46×10^{46} erg/sec	4.77×10^{46} erg/sec
	Power in the magnetic field	P_B	0.07×10^{46} erg/sec	0.25×10^{46} erg/sec
	Total required jet power	P_{tot}	1.81×10^{46} erg/sec	5.48×10^{46} erg/sec

4.7 Chapter conclusions

Below, the important aspects of chapter-4 are briefly highlighted -

- First broadband study ever done to understand the nature of the blazar 4C +28.07.
- Three major flares and many sub-flares have been observed in the decade-long γ-ray light curve ($\sim$ 12 years)
- A significant correlation between γ-ray and radio light curves was observed with a time lag of $\sim$ 70 days and $\sim$ 135 days for Flare-A and Flare-C, respectively. However, no significant correlation was seen for Flare-B.
- Gamma-ray production can happen efficiently by EC mechanism near the BLR region, while the time delay in radio emission indicates its emission region is separated by $\sim$ nine pc and $\sim$ four pc from Gamma-ray emission region for Flare-A and Flare-C respectively.
- To account for the different emission zones of radio and γ-ray emission for Flare-A and Flare-C, two-zone emission model is used for the broadband SED modeling under the leptonic scenario.

Chapter 5

Conclusion

Blazars are observed in all wavelengths, from radio to very high-energy gamma-rays. It is one of the most luminous sources of high energy non-thermal emission in the universe. The study of these sources in the high energy regime plays a crucial role in tracing the various physical properties of the system e.g., particle acceleration mechanism, production of γ-rays, neutrinos, etc. Gamma-ray astronomy has evolved in the past few decades while investigating these phenomena. On 11th June 2008, after the launch of the Fermi Gamma-ray Space Telescope, this field has attracted more attention of the whole astrophysics community. The latest fourth fermi catalog (4FGL) has listed approximately 5000 high energy sources, most of which are known as blazars. With the help of Fermi-LAT data and other temporal and spectral data from different space and ground-based telescopes, efforts are being made continuously to understand the nature of blazars.

5.1 Summary of the thesis

In this thesis, I have studied temporal and spectral behaviour in gamma-rays of two FSRQs namely 3C454.3 and 4C+28.07. I have also analyzed the Swift-XRT/UVOT data for these sources. By using other publicly available spectral data (e.g., Catalina, SMARTS, OVRO), multi-wavelength leptonic modelling has been done to understand the physical properties of jets during flaring states.

In chapter-3, I have included the results of extensively studied gamma-ray light curves ($\sim$ 9 years) and SEDs for the source 3C454.3. This long-term hourly binning (6 hours) light curve history has identified five major flares and several sub-flares. After scanning this whole 6-hour binning light curve, a variability time of 1.70$\pm$0.38 hours has been found, which constrains the size of the gamma-ray emission region to be $\sim 10^{15}$ cm. In most cases, the γ-ray SEDs of the flares are best described by the log-parabolic model, indicating that the injected electrons spectrum also follows the same under the leptonic scenario. A simple one-zone leptonic modelling of the brightest flares (Flare-2A & Flare-2D) has been done to explain the multi-wavelength SED. The required magnetic fields are 3.8 G and 2.3 G for Flare-2A and Flare-2D, respectively, which are comparable to other FSRQs. The modelling of the γ-ray light curves has also been done by varying two main parameters with time, which are involved in multi-wavelength SED modelling. These are- i) Doppler factor (δ) and ii) Luminosity factor of the injected electrons (l_0). Time variation of the Doppler factor indicates the purely geometrical origin of the variability in the light curves, whereas l_0 is related to the intrinsic physical properties of the system.

In chapter-4, I have included the results of the multi-wavelength study of the source 4C+28.07. This is the first broadband study ever done on this source. Three major flares have been identified in this long-term 10 days binned γ-ray light curve history ($\sim$ 12 years). These flares are further studied in 3 days binning to identify the different states of activity (e.g. Pre-flare, flare etc.) by Bayesian block representation. The correlation study between optical & γ-ray light curve for Flare-A show a small time lag ($\sim$ 6 days) with high significance. A significant (more than 60%) correlation between γ-ray and 15 GHz radio light curves was observed with a time lag of $\sim$ 70 days and $\sim$ 135 days for Flare-A and Flare-C respectively. However, no significant correlation was observed for Flare-B. Two zone leptonic modelling has been used to explain the multi-wavelength SEDs. In Flare-A, these emission regions are separated by $\sim$ 9 pc, whereas in Flare-C this separation is $\sim$ 4 pc along the jet axis. The inner emission region (Blob-I) emits radiation via synchrotron, SSC and EC processes. The outer emission region (Blob-II) emits via only synchrotron and SSC processes. BLR and accretion disk photons are available only for Blob-I to produce EC emission. The maximum required jet power in this two-zone model is 9.34×10^{46} erg sec^{-1} for flare-A, which is below the Eddington luminosity of the source (2.29×10^{47} erg sec^{-1}).

5.2 Future directions

This thesis is a small contribution to the blazars community to understand more about the physical properties of the jets. There are several open issues about AGN jets that still remain unclear, such as jet launching mechanism, acceleration of particles to relativistic energy, production of high energy γ-rays, the origin of fast variability, Quasi-periodicity of blazars, etc. Multi-wavelength study of more and more blazars will directly or indirectly resolve some of these issues. Due to these reasons, availability of simultaneous multi-wavelength temporal and spectral data are indispensable. Steward, Smarts, OVRO, and SMA are the Fermi-LAT support program that are continuously helping to acquire multi-wavelength data of blazars. There are other space & ground-based telescopes such as Swift-XRT/UVOT, NuSTAR, XMM-Newton, ASTROSAT, Catalina, which are also helping to this program.

Hadronic or lepto-hadronic models of blazars are still under investigations, moreover multiple zones of emissions in jets of blazars may be necessary in many cases. On September 22, 2017, a $\sim$ 290 TeV muon neutrino (ν_μ) was detected by IceCube Neutrino Observatory during the γ-ray flaring state of TXS 0506+056. This supports the hadronic scenario of emission from jets. IceCube detector located at the South pole has detected hundreds of astrophysical neutrinos whose origins are not yet known. Blazars may be sources of at least some of the astrophysical neutrinos detected by IceCube as discussed in many recent papers (Aartsen et al. [190], Rodrigues et al. [191], Das et al. [192]).

Currently, the very high energy γ-ray detectors e.g., High Energy Stereoscopic System (H.E.S.S.[1]), Major Atmospheric Gamma Imaging Cherenkov Telescopes (MAGIC[2]), Very Energetic Radiation Imaging Telescope Array System (VERITAS[3]), Tibet, High Altitude Water Cherenkov Experiment (HAWC[4]), Large High Altitude Air Shower Observatory (LHAASO[5]) are observing the TeV gamma ray universe. These ground-based telescopes cover the energy range from 100 GeV to more than 100 TeV energy. In future, the next-generation ground-based high-energy gamma-ray detector Cherenkov Telescope Array (CTA) will surely add further attention to gamma-ray astronomy. This will be the most sensitive ground-based gamma-ray detection observatory [6], that will cover ~ 20 GeV to ~ 300 TeV energy range with better angular and temporal resolution compared to the existing detectors. The understanding of TeV blazars, beaming, variability, acceleration of charged particles in the jets, etc. will improve much more with the data from CTA in the upcoming days.

[1] `https://www.mpi-hd.mpg.de/hfm/HESS/pages/about/telescopes/`

[2] `https://www.mpp.mpg.de/en/research/astroparticle-physics-and-cosmology/magic-and-cta-gamma-ray-telescopes/magic`

[3] `https://veritas.sao.arizona.edu/`

[4] `https://www.hawc-observatory.org/`

[5] `http://english.ihep.cas.cn/lhaaso/`

[6] `https://www.cta-observatory.org/about/`

Bibliography

[1] Guinevere Kauffmann et al. The host galaxies of active galactic nuclei. *mnras*, 346 (4):1055–1077, December 2003. doi: 10.1111/j.1365-2966.2003.07154.x.

[2] Edward Arthur Fath. The spectra of some spiral nebulae and globular star clusters. *Lick Observatory Bulletin*, 149:71–77, January 1909. doi: 10.5479/ADS/bib/1909LicOB.5.71F.

[3] H. D. Curtis. Descriptions of 762 Nebulae and Clusters Photographed with the Crossley Reflector. *Publications of Lick Observatory*, 13:9–42, January 1918.

[4] V. M. Slipher. The spectrum and velocity of the nebula N.G.C. 1068 (M 77). *Lowell Observatory Bulletin*, 3:59–62, January 1917.

[5] M. L. Humason. The Emission Spectrum of the Extra-Galactic Nebula N. G. C. 1275. *pasp*, 44(260):267, August 1932. doi: 10.1086/124242.

[6] N. U. Mayall. The Spectrum of the Spiral Nebula NGC 4151. *pasp*, 46(271):134, June 1934. doi: 10.1086/124429.

[7] Carl K. Seyfert. Nuclear Emission in Spiral Nebulae. *apj*, 97:28, January 1943. doi: 10.1086/144488.

[8] W. Baade and R. Minkowski. Identification of the Radio Sources in Cassiopeia, Cygnus A, and Puppis A. *apj*, 119:206, January 1954. doi: 10.1086/145812.

[9] D. O. Edge, J. R. Shakeshaft, W. B. McAdam, J. E. Baldwin, and S. Archer. A survey of radio sources at a frequency of 159 Mc/s. *memras*, 68:37–60, January 1959.

[10] A. S. Bennett. The preparation of the revised 3C catalogue of radio sources. *mnras*, 125:75, January 1962. doi: 10.1093/mnras/125.1.75.

[11] J. A. Ekers. The Parkes catalogue of radio sources, declination zone +20 to -90 . *Australian Journal of Physics Astrophysical Supplement*, 7:3–75, January 1969.

[12] J. D. H. Pilkington and J. F. Scott. A survey of radio sources between declinations 20° and 40°. *memras*, 69:183, January 1965.

[13] J. F. R. Gower, P. F. Scott, and D. Wills. A survey of radio sources in the declination ranges —07° to 20° and 40° to 80°. *memras*, 71:49, January 1967.

[14] C. Hazard, S. Gulkis, and A. D. Bray. Lunar Occultation Studies of Five Weak Radio Sources of Small Angular Size. *apj*, 148:669, June 1967. doi: 10.1086/149192.

[15] R. S. Dixon and J. D. Kraus. A High-Sensivity 1415 MHz Survey at North Declinations betwen 19 and 37 degrees . *aj*, 73:381–407, January 1968. doi: 10.1086/110642.

[16] J. R. Ehman, R. S. Dixon, C. M. Ramakrishna, and J. D. Kraus. The Ohio Survey: VI. *aj*, 79:144–317, February 1974. doi: 10.1086/111543.

[17] E. T. Byram, T. A. Chubb, and H. Friedman. Cosmic X-ray Sources, Galactic and Extragalactic. *Science*, 152(3718):66–71, April 1966. doi: 10.1126/science.152.3718.66.

[18] D. J. Thompson et al. Calibration of the Energetic Gamma-Ray Experiment Telescope (EGRET) for the Compton Gamma-Ray Observatory. *apjs*, 86:629, June 1993. doi: 10.1086/191793.

[19] R. C. Hartman et al. The Third EGRET Catalog of High-Energy Gamma-Ray Sources. *apjs*, 123(1):79–202, July 1999. doi: 10.1086/313231.

[20] W. B. Atwood et al. The Large Area Telescope on the Fermi Gamma-Ray Space Telescope Mission. *apj*, 697(2):1071–1102, June 2009. doi: 10.1088/0004-637X/697/2/1071.

[21] M. Ajello et al. The Fourth Catalog of Active Galactic Nuclei Detected by the Fermi Large Area Telescope. *apj*, 892(2):105, April 2020. doi: 10.3847/1538-4357/ab791e.

[22] John T. Stocke, Simon L. Morris, Ray J. Weymann, and Craig B. Foltz. The Radio Properties of the Broad-Absorption-Line QSOs. *apj*, 396:487, September 1992. doi: 10.1086/171735.

[23] C. Megan Urry and Paolo Padovani. Unified Schemes for Radio-Loud Active Galactic Nuclei. *pasp*, 107:803, September 1995. doi: 10.1086/133630.

[24] W. Z. Wisniewski and D. E. Kleinmann. 16. Multicolor photometry of Seyfert galaxies and measurement at 1.55 microns of the jet in M 87. *Astron. J.*, 73:866–867, Nov 1968. ISSN 0004-6256. doi: 10.1086/110721.

[25] J. S. Kaastra, K. C. Steenbrugge, A. J. J. Raassen, R. L. J. van der Meer, A. C. Brinkman, D. A. Liedahl, E. Behar, and A. de Rosa. X-ray spectroscopy of NGC 5548. *Astron. Astrophys.*, 386(2):427–445, May 2002. ISSN 0004-6361. doi: 10.1051/0004-6361:20020235.

[26] E. Y. Khachikian and D. W. Weedman. An atlas of Seyfert galaxies. *Astrophys. J.*, 192:581–589, Sep 1974. ISSN 0004-637X. doi: 10.1086/153093.

[27] É. Ya. Khachikyan and D. W. Weedman. A spectroscopic study of luminous galactic nuclei. *Astrophysics*, 7(3):231–240, July 1971. doi: 10.1007/BF01001021.

[28] James S. Ulvestad and Andrew S. Wilson. Radio Structures of Seyfert Galaxies. VII. Extension of a Distance-limited Sample. *Astrophys. J.*, 343:659, Aug 1989. ISSN 0004-637X. doi: 10.1086/167737.

[29] A. Lawrence. The relative frequency of broad-lined and narrow-lined active galactic nuclei : implications for unified schemes. *Mon. Not. R. Astron. Soc.*, 252:586, Oct 1991. ISSN 0035-8711. doi: 10.1093/mnras/252.4.586.

[30] Luigi Spinoglio and Juan Antonio Fernández-Ontiveros. AGN types and unification model. *Proc. Int. Astron. Union*, 15(S356):29–43, Oct 2019. ISSN 1743-9213. doi: 10.1017/S1743921320002549.

[31] G. Matt, S. Bianchi, M. Guainazzi, X. Barcons, and F. Panessa. The Suzaku X-ray spectrum of NGC 3147 - Further insights on the best "true" Seyfert 2 galaxy candidate. *Astron. Astrophys.*, 540:A111, Apr 2012. ISSN 0004-6361. doi: 10.1051/0004-6361/201118729.

[32] D. E. Osterbrock. Seyfert galaxies with weak broad H alpha emission lines. *Astrophys. J.*, 249:462–470, Oct 1981. ISSN 0004-637X. doi: 10.1086/159306.

[33] Paola Grandi, Laura Maraschi, C. Megan Urry, and Giorgio Matt. Weak Reprocessed Features in the Broad-Line Radio Galaxy 3C 382. *Astrophys. J.*, 556(1): 35–41, Jul 2001. ISSN 0004-637X. doi: 10.1086/321546.

[34] S. A. Grandi and D. E. Osterbrock. Optical spectra of radio galaxies. *Astrophys. J.*, 220:783–789, Mar 1978. ISSN 0004-637X. doi: 10.1086/155966.

[35] P. Padovani. Gamma-Ray Emitting AGN and Unified Schemes. In Y. Giraud-Heraud and J. Tran Thanh van, editors, *Very High Energy Phenomena in the Universe; Moriond Workshop*, page 7, January 1997.

[36] S. J. Lilly, M. S. Longair, and L. Miller. Non-stellar radiation in radio galaxies at

3.5 MU m. *Mon. Not. R. Astron. Soc.*, 214:109–118, May 1985. ISSN 0035-8711. doi: 10.1093/mnras/214.2.109.

[37] B. L. Fanaroff and J. M. Riley. ADS. *Monthly Notices of the Royal Astronomical Society, Vol. 167, p. 31P-36P (1974)*, 167:31P, May 1974. ISSN 0035-8711. doi: 10.1093/mnras/167.1.31P.

[38] A. H. Bridle. ADS. *Astronomical Journal, Vol. 89, p. 979-986 (1984)*, 89:979, Jul 1984. ISSN 0004-6256. doi: 10.1086/113593.

[39] Stefi A. Baum, Esther L. Zirbel, and Christopher P. O'Dea. ADS. *Astrophysical Journal v.451, p.88*, 451:88, Sep 1995. ISSN 0004-637X. doi: 10.1086/176202.

[40] Robert Antonucci. Unified models for active galactic nuclei and quasars. *araa*, 31: 473–521, January 1993. doi: 10.1146/annurev.aa.31.090193.002353.

[41] Jian-Min Wang and En-Peng Zhang. The Unified Model of Active Galactic Nuclei. II. Evolutionary Connection. *Astrophys. J.*, 660(2):1072–1092, May 2007. ISSN 0004-637X. doi: 10.1086/513685.

[42] Stefano Bianchi, Roberto Maiolino, and Guido Risaliti. AGN Obscuration and the Unified Model. *Adv. Astron.*, 2012:782030, Feb 2012. ISSN 1687-7969. doi: 10.1155/2012/782030.

[43] Hagai Netzer. Revisiting the Unified Model of Active Galactic Nuclei. *Annu. Rev. Astron. Astrophys.*, 53(1):365–408, Aug 2015. ISSN 0066-4146. doi: 10.1146/annurev-astro-082214-122302.

[44] Edward A. Pier and Julian H. Krolik. Radiation-Pressure–supported Obscuring Tori around Active Galactic Nuclei. *Astrophys. J.*, 399:L23, Nov 1992. ISSN 0004-637X. doi: 10.1086/186597.

[45] Edward A. Pier and Julian H. Krolik. Infrared Spectra of Obscuring Dust Tori around Active Galactic Nuclei. II. Comparison with Observations. *Astrophys. J.*, 418:673, Dec 1993. ISSN 0004-637X. doi: 10.1086/173427.

[46] Volker Beckmann and Chris R. Shrader. *Active Galactic Nuclei.* Aug 2012. ISBN 978-3-52741078-1. URL `https://ui.adsabs.harvard.edu/abs/2012agn..book.....B/abstract`.

[47] Steven A. Balbus and John F. Hawley. A Powerful Local Shear Instability in Weakly Magnetized Disks. I. Linear Analysis. *Astrophys. J.*, 376:214, Jul 1991. ISSN 0004-637X. doi: 10.1086/170270.

[48] R. D. Blandford and R. L. Znajek. Electromagnetic extraction of energy from Kerr black holes. *Mon. Not. R. Astron. Soc.*, 179:433–456, May 1977. ISSN 0035-8711. doi: 10.1093/mnras/179.3.433.

[49] R. D. Blandford and D. G. Payne. Hydromagnetic flows from accretion disks and the production of radio jets. *mnras*, 199:883–903, June 1982. doi: 10.1093/mnras/199.4.883.

[50] Gian Luigi Granato, Luigi Danese, and Alberto Franceschini. Thick Tori around Active Galactic Nuclei: The Case for Extended Tori and Consequences for Their X-Ray and Infrared Emission. *Astrophys. J.*, 486(1):147–159, Sep 1997. ISSN 0004-637X. doi: 10.1086/304502.

[51] G. Weigelt et al. Diffraction-limited bispectrum speckle interferometry of the nuclear region of the Seyfert galaxy NGC 1068 in the H and K' bands. *Astron. Astrophys.*, 425(1):77–87, Oct 2004. ISSN 0004-6361. doi: 10.1051/0004-6361:20040362.

[52] R. E. Mason. Spatially Resolved Mid-Infrared Spectroscopy of NGC 1068: The Nature and Distribution of the Nuclear Material. *Astrophys. J.*, 640(2):612–624, Apr 2006. ISSN 0004-637X. doi: 10.1086/500299.

[53] K. R. W. Tristram. Resolving the complex structure of the dust torus in the active nucleus of the Circinus galaxy. *Astron. Astrophys.*, 474(3):837–850, Nov 2007. ISSN 0004-6361. doi: 10.1051/0004-6361:20078369.

[54] Maia Nenkova, Željko Ivezić, and Moshe Elitzur. Dust Emission from Active Galactic Nuclei. *Astrophys. J.*, 570(1):L9–L12, May 2002. ISSN 0004-637X. doi: 10.1086/340857.

[55] A. L. Müller and G. E. Romero. Radiation from the impact of broad-line region clouds onto AGN accretion disks. *Astron. Astrophys.*, 636:A92, Apr 2020. ISSN 0004-6361. doi: 10.1051/0004-6361/202037639.

[56] W. Kollatschny and M. Zetzl. The shape of broad-line profiles in active galactic nuclei. *Astron. Astrophys.*, 549:A100, Jan 2013. ISSN 0004-6361. doi: 10.1051/0004-6361/201219411.

[57] R. D. Blandford, H. Netzer, L. Woltjer, T. J.-L. Courvoisier, and M. Mayor. *Active Galactic Nuclei*. 1990. ISBN 978-354053285. URL `https://ui.adsabs.harvard.edu/abs/1990agn..conf.....B/abstract`.

[58] H. Netzer. ADS. *20. Saas-Fee Advanced Course of the Swiss Society for Astrophysics and Astronomy: Active galactic nuclei, p. 57 - 160*, page 57, 1990. URL `https://ui.adsabs.harvard.edu/abs/1990agn..conf...57N/abstract`.

[59] Hagai Netzer. Physical Processes in Starburst and Active Galaxies. In Itziar Aretxaga, Daniel Kunth, and Raúl Mújica, editors, *Advanced Lectures on the Starburst-AGN*, page 117, January 2001. doi: 10.1142/9789812811318_0004.

[60] ADS, Feb 1997. URL `https://ui.adsabs.harvard.edu/abs/1997iagn.book.....P/abstract`. [Online; accessed 30. Aug. 2021].

[61] M. Villar Martín, E. Bellocchi, J. Stern, C. Ramos Almeida, C. Tadhunter, and R. González Delgado. Deconstructing the narrow-line region of the nearest obscured

quasar. *Mon. Not. R. Astron. Soc.*, 454(1):439–456, Nov 2015. ISSN 0035-8711. doi: 10.1093/mnras/stv1864.

[62] Zhi-Fu Chen, Y. Qin, Z. Chen, and L. Lü. The size of narrow line region and [oiii] luminosity analyzed from sdss dr7 quasar catalogue. *Journal of Astrophysics and Astronomy*, 32:273–276, 2011.

[63] N. Bennert, B. Jungwiert, S. Komossa, M. Haas, and R. Chini. Size and properties of the narrow-line region in Seyfert-2 galaxies from spatially-resolved optical spectroscopy. *Astron. Astrophys.*, 456(3):953–966, Sep 2006. ISSN 0004-6361. doi: 10.1051/0004-6361:20065319.

[64] Nicola Bennert, Heino Falcke, Hartmut Schulz, Andrew S. Wilson, and Beverley J. Wills. Size and Structure of the Narrow-Line Region of Quasars∗. *Astrophys. J.*, 574(2):L105–L109, Jun 2002. ISSN 0004-637X. doi: 10.1086/342420.

[65] Svetlana G. Jorstad et al. Multiepoch Very Long Baseline Array Observations of EGRET-detected Quasars and BL Lacertae Objects: Connection between Superluminal Ejections and Gamma-Ray Flares in Blazars. *Astrophys. J.*, 556(2):738–748, Aug 2001. ISSN 0004-637X. doi: 10.1086/321605.

[66] Alan H. Bridle, David H. Hough, Colin J. Lonsdale, Jack O. Burns, and Robert A. Laing. Deep VLA Imaging of Twelve Extended 3CR Quasars. *Astron. J.*, 108:766, Sep 1994. ISSN 0004-6256. doi: 10.1086/117112.

[67] Roger Blandford, David Meier, and Anthony Readhead. Relativistic Jets from Active Galactic Nuclei. *Annu. Rev. Astron. Astrophys.*, 57(1):467–509, Aug 2019. ISSN 0066-4146. doi: 10.1146/annurev-astro-081817-051948.

[68] J. H. Fan, K. S. Cheng, L. Zhang, and C. H. Liu. Polarization and beaming effect for BL Lacertae objects. *Astron. Astrophys.*, 327:947–951, Nov 1997. ISSN 0004-6361. URL `https://ui.adsabs.harvard.edu/abs/1997A&A...327..947F/abstract`.

[69] R. D. Blandford and R. L. Znajek. Electromagnetic extraction of energy from Kerr black holes. *mnras*, 179:433–456, May 1977. doi: 10.1093/mnras/179.3.433.

[70] D. L. Meier, S. Edgington, P. Godon, D. G. Payne, and K. R. Lind. A magnetic switch that determines the speed of astrophysical jets - Nature. *Nature*, 388:350–352, Jul 1997. ISSN 1476-4687. doi: 10.1038/41034.

[71] Vladimir Semenov, Sergey Dyadechkin, and Brian Punsly. Simulations of Jets Driven by Black Hole Rotation. *Science*, 305(5686):978–980, Aug 2004. ISSN 0036-8075. doi: 10.1126/science.1100638.

[72] Alexander Tchekhovskoy, Ramesh Narayan, and Jonathan C. Mckinney. Efficient generation of jets from magnetically arrested accretion on a rapidly spinning black hole. *Mon. Not. R. Astron. Soc. Lett.*, 418(1):L79–L83, Nov 2011. ISSN 1745-3933. doi: 10.1111/j.1745-3933.2011.01147.x.

[73] M. Stickel, P. Padovani, C. M. Urry, J. W. Fried, and H. Kuehr. ADS. *Astrophysical Journal v.374, p.431*, 374:431, Jun 1991. ISSN 0004-637X. doi: 10.1086/170133.

[74] John T. Stocke et al. ADS. *Astrophysical Journal Supplement v.76, p.813*, 76:813, Jul 1991. ISSN 0067-0049. doi: 10.1086/191582.

[75] Hermine Landt, Paolo Padovani, Eric S. Perlman, and Paolo Giommi. A physical classification scheme for blazars. *Mon. Not. R. Astron. Soc.*, 351(1):83–100, Jun 2004. ISSN 0035-8711. doi: 10.1111/j.1365-2966.2004.07750.x.

[76] P. Giommi. Open Universe for Blazars: a new generation of astronomical products based on 14 years of Swift-XRT data. *Astron. Astrophys.*, 631:A116, Nov 2019. ISSN 0004-6361. doi: 10.1051/0004-6361/201935646.

[77] G. Tagliaferri. The concave X-ray spectrum of the blazar ON 231: the signature of intermediate BL Lacertae objects. *aap*, 354:431–438, February 2000.

[78] A. Abramowski et al. Simultaneous multi-wavelength campaign on PKS 2005-489 in a high state. *Astron. Astrophys.*, 533:A110, Sep 2011. ISSN 0004-6361. doi: 10.1051/0004-6361/201016170.

[79] Anna Barnacka, Rafal Moderski, Bagmeet Behera, Pierre Brun, and Stefan Wagner. PKS 1510-089: a rare example of a flat spectrum radio quasar with a very high-energy emission. *Astron. Astrophys.*, 567:A113, Jul 2014. ISSN 0004-6361. doi: 10.1051/0004-6361/201322205.

[80] S. J. Wagner and A. Witzel. Intraday Variability in Quasars and BL LAC Objects. *Annu. Rev. Astron. Astrophys.*, 33(1):163–197, Sep 1995. ISSN 0066-4146. doi: 10.1146/annurev.aa.33.090195.001115.

[81] Marie-Helene Ulrich, Laura Maraschi, and C. Megan Urry. VARIABILITY OF ACTIVE GALACTIC NUCLEI. *Annu. Rev. Astron. Astrophys.*, 35(1):445–502, Sep 1997. ISSN 0066-4146. doi: 10.1146/annurev.astro.35.1.445.

[82] F. Aharonian et al. An Exceptional Very High Energy Gamma-Ray Flare of PKS 2155-304. *apjl*, 664(2):L71–L74, August 2007. doi: 10.1086/520635.

[83] A. A. Abdo et al. Gamma-ray Light Curves and Variability of Bright Fermi-detected Blazars. *Astrophys. J.*, 722(1):520–542, Oct 2010. ISSN 0004-637X. doi: 10.1088/0004-637X/722/1/520.

[84] C. M. Raiteri et al. The awakening of BL Lacertae: observations by Fermi, Swift and the GASP-WEBT. *Mon. Not. R. Astron. Soc.*, 436(2):1530–1545, Dec 2013. ISSN 0035-8711. doi: 10.1093/mnras/stt1672.

[85] A. Shukla, K. Mannheim, S. R. Patel, J. Roy, V. R. Chitnis, D. Dorner, A. R. Rao, G. C. Anupama, and C. Wendel. Short-timescale γ-Ray Variability in CTA 102. *Astrophys. J. Lett.*, 854(2):L26, Feb 2018. ISSN 2041-8213. doi: 10.3847/2041-8213/aaacca.

[86] George B. Rybicki and Alan P. Lightman. *Radiative Processes in Astrophysics*. May 1985. ISBN 978-0-47182759-7. doi: 10.1002/9783527618170.

[87] K. Mannheim. Possible production of high-energy gamma rays from proton acceleration in the extragalactic radio source markarian 501. *Science*, 279(5351):684–686, Jan 1998. ISSN 1095-9203. doi: 10.1126/science.279.5351.684.

[88] K. Mannheim. The proton blazar. *Astron. Astrophys.*, 269:67–76, Mar 1993. ISSN 0004-6361. URL `https://ui.adsabs.harvard.edu/abs/1993A%26A...269...67M/abstract`.

[89] W. B. Atwood et al. The Large Area Telescope on the Fermi Gamma-Ray Space Telescope Mission. *apj*, 697(2):1071–1102, June 2009. doi: 10.1088/0004-637X/697/2/1071.

[90] N. Gehrels et al. The Swift Gamma-Ray Burst Mission. *Astrophys. J.*, 611(2): 1005–1020, Aug 2004. ISSN 0004-637X. doi: 10.1086/422091.

[91] David N. Burrows et al. The Swift X-Ray Telescope. *ssr*, 120(3-4):165–195, October 2005. doi: 10.1007/s11214-005-5097-2.

[92] Peter W. A. Roming et al. The Swift Ultra-Violet/Optical Telescope. *Space Sci. Rev.*, 120(3-4):95–142, Oct 2005. ISSN 0038-6308. doi: 10.1007/s11214-005-5095-4.

[93] Edward F. Schlafly and Douglas P. Finkbeiner. Measuring Reddening with Sloan Digital Sky Survey Stellar Spectra and Recalibrating SFD. *Astrophys. J.*, 737(2): 103, Aug 2011. ISSN 0004-637X. doi: 10.1088/0004-637X/737/2/103.

[94] A. A. Breeveld, W. Landsman, S. T. Holland, P. Roming, N. P. M. Kuin, and M. J. Page. An Updated Ultraviolet Calibration for the Swift/UVOT. *arXiv*, Feb 2011. doi: 10.1063/1.3621807.

[95] V. M. Larionov et al. Exceptional outburst of the blazar CTA 102 in 2012: the GASP-WEBT campaign and its extension. *mnras*, 461(3):3047–3056, September 2016. doi: 10.1093/mnras/stw1516.

[96] Joseph L. Richards et al. BLAZARS IN THE FERMI ERA: THE OVRO 40 m TELESCOPE MONITORING PROGRAM. *Astrophys. J. Suppl. Ser.*, 194(2):29, May 2011. ISSN 0067-0049. doi: 10.1088/0067-0049/194/2/29.

[97] P. S. Smith, E. Montiel, S. Rightley, J. Turner, G. D. Schmidt, and B. T. Jannuzi. Coordinated Fermi/Optical Monitoring of Blazars and the Great 2009 September Gamma-ray Flare of 3C 454.3. *arXiv e-prints*, page arXiv:0912.3621, Dec 2009. URL `https://ui.adsabs.harvard.edu/abs/2009arXiv0912.3621S/abstract`.

[98] A. J. Drake et al. FIRST RESULTS FROM THE CATALINA REAL-TIME TRANSIENT SURVEY. *Astrophys. J.*, 696(1):870–884, Apr 2009. ISSN 0004-637X. doi: 10.1088/0004-637x/696/1/870.

[99] R. C. Hartman et al. 3C 454.3 and CTA 102. *International Astronomical Union Circular*, 5477:2, Mar 1992. ISSN 0081-0304. URL `https://ui.adsabs.harvard.edu/abs/1992IAUC.5477....2H/exportcitation`.

[100] R. C. Hartman et al. EGRET Detection of High-Energy Gamma Radiation from the OVV Quasar 3C 454.3. *Astrophys. J.*, 407:L41, Apr 1993. ISSN 0004-637X. doi: 10.1086/186801.

[101] P. Giommi. Swift and infra-red observations of the blazar 3C 454.3 during the giant X-ray flare of May 2005. *Astron. Astrophys.*, 456(3):911–916, Sep 2006. ISSN 0004-6361. doi: 10.1051/0004-6361:20064874.

[102] C. M. Raiteri et al. The high activity of 3C 454.3 in autumn 2007. Monitoring by the WEBT during the AGILE detection. *Astron. Astrophys.*, 485(2):L17–L20, Jul 2008. ISSN 0004-6361. doi: 10.1051/0004-6361:200809995.

[103] S. Vercellone et al. Multiwavelength Observations of 3C 454.3. I. The AGILE 2007 November campaign on the "Crazy Diamond". *Astrophys. J.*, 690(1):1018–1030, Jan 2009. ISSN 0004-637X. doi: 10.1088/0004-637X/690/1/1018.

[104] I. Donnarumma et al. Multiwavelength Observations of 3C 454.3. II. The AGILE 2007 December Campaign. *Astrophys. J.*, 707(2):1115–1123, Dec 2009. ISSN 0004-637X. doi: 10.1088/0004-637X/707/2/1115.

[105] A. A. Abdo et al. Early Fermi Gamma-ray Space Telescope Observations of the Quasar 3C 454.3. *Astrophys. J.*, 699(1):817–823, Jul 2009. ISSN 0004-637X. doi: 10.1088/0004-637X/699/1/817.

[106] E. W. Bonning, C. Bailyn, C. M. Urry, M. Buxton, G. Fossati, L. Maraschi, P. Coppi, R. Scalzo, J. Isler, and A. Kaptur. Correlated Variability in the Blazar 3C 454.3. *Astrophys. J.*, 697(2):L81–L85, Jun 2009. ISSN 0004-637X. doi: 10.1088/0004-637X/697/2/L81.

[107] Haritma Gaur, Alok C. Gupta, and Paul J. Wiita. Multiwavelength Variability of the Blazars Mrk 421 and 3C 454.3 in the High State. *Astron. J.*, 143(1):23, Jan 2012. ISSN 0004-6256. doi: 10.1088/0004-6256/143/1/23.

[108] Alok C. Gupta et al. A peculiar multiwavelength flare in the blazar 3C 454.3. *Mon. Not. R. Astron. Soc.*, 472(1):788–798, Nov 2017. ISSN 0035-8711. doi: 10.1093/mnras/stx2072.

[109] C. M. Raiteri et al. The long-lasting activity of 3C 454.3. GASP-WEBT and satellite observations in 2008-2010. *Astron. Astrophys.*, 534:A87, Oct 2011. ISSN 0004-6361. doi: 10.1051/0004-6361/201117026.

[110] Svetlana G. Jorstad et al. A Tight Connection between Gamma-Ray Outbursts and Parsec-scale Jet Activity in the Quasar 3C 454.3. *Astrophys. J.*, 773(2):147, Aug 2013. ISSN 0004-637X. doi: 10.1088/0004-637X/773/2/147.

[111] Ann E. Wehrle, Alan P. Marscher, Svetlana G. Jorstad, Mark A. Gurwell, Manasvita Joshi, Nicholas R. MacDonald, Karen E. Williamson, Iván Agudo, and Dirk Grupe. Multiwavelength Variations of 3C 454.3 during the 2010 November to 2011 January Outburst. *Astrophys. J.*, 758(2):72, Oct 2012. ISSN 0004-637X. doi: 10.1088/0004-637X/758/2/72.

[112] Mahito Sasada et al. Extremely High Polarization in the 2010 Outburst of Blazar 3C 454.3. *Astrophys. J.*, 784(2):141, Apr 2014. ISSN 0004-637X. doi: 10.1088/0004-637X/784/2/141.

[113] A. G. Gorshkov et al. Long-Term and Rapid Radio Variability of the Blazar 3C 454.3 in 2010-2017. *Astron. Rep.*, 62(3):183–199, Mar 2018. ISSN 1063-7729. doi: 10.1134/S1063772918030046.

[114] Pankaj Kushwaha, Alok C. Gupta, Ranjeev Misra, and K. P. Singh. Multiwavelength temporal variability of the blazar 3C 454.3 during 2014 activity phase. *Mon. Not. R. Astron. Soc.*, 464(2):2046–2052, Jan 2017. ISSN 0035-8711. doi: 10.1093/mnras/stw2440.

[115] Richard J. Britto, Eugenio Bottacini, Benoît Lott, Soebur Razzaque, and Sara Buson. Fermi-LAT Observations of the 2014 May-July Outburst from 3C 454.3. *apj*, 830(2):162, October 2016. doi: 10.3847/0004-637X/830/2/162.

[116] Bhoomika Rajput, C. S. Stalin, S. Sahayanathan, Suvendu Rakshit, and Amit Kumar Mandal. Temporal correlation between the optical and γ-ray flux variations in the blazar 3C 454.3. *Mon. Not. R. Astron. Soc.*, 486(2):1781–1795, Jun 2019. ISSN 0035-8711. doi: 10.1093/mnras/stz941.

[117] Krzysztof Nalewajko, Alok C. Gupta, Mai Liao, Krzysztof Hryniewicz, Maitrayee Gupta, and Minfeng Gu. Long-term optical spectroscopic variations in blazar 3C 454.3. *Astron. Astrophys.*, 631:A4, Nov 2019. ISSN 0004-6361. doi: 10.1051/0004-6361/201935904.

[118] A. Sarkar. Long-term Variability and Correlation Study of the Blazar 3C 454.3 in the Radio, NIR, and Optical Wavebands. *apj*, 887(2):185, December 2019. doi: 10.3847/1538-4357/ab5281.

[119] Zachary R. Weaver et al. The 2016 June Optical and Gamma-Ray Outburst and Optical Microvariability of the Blazar 3C 454.3. *Astrophys. J.*, 875(1):15, Apr 2019. ISSN 0004-637X. doi: 10.3847/1538-4357/ab0e7c.

[120] M. Zamaninasab et al. Evidence for a large-scale helical magnetic field in the quasar 3C 454.3. *Mon. Not. R. Astron. Soc.*, 436(4):3341–3356, Dec 2013. ISSN 0035-8711. doi: 10.1093/mnras/stt1816.

[121] Justin D. Finke and Charles D. Dermer. On the Break in the Fermi-Large Area Telescope Spectrum of 3C 454.3. *Astrophys. J.*, 714(2):L303–L307, May 2010. ISSN 0004-637X. doi: 10.1088/2041-8205/714/2/L303.

[122] Matteo Cerruti, Charles D. Dermer, Benoît Lott, Catherine Boisson, and Andreas Zech. Gamma-Ray Blazars near Equipartition and the Origin of the GeV Spectral Break in 3C 454.3. *apjl*, 771(1):L4, July 2013. doi: 10.1088/2041-8205/771/1/L4.

[123] L. Hunger and A. Reimer. Shaping the GeV-spectra of bright blazars. *Astron. Astrophys.*, 589:A96, May 2016. ISSN 0004-6361. doi: 10.1051/0004-6361/201424738.

[124] C. Diltz and M. Böttcher. Leptonic and Lepto-Hadronic Modeling of the 2010 November Flare from 3C 454.3. *apj*, 826(1):54, July 2016. doi: 10.3847/0004-637X/826/1/54.

[125] Zahir Shah, S. Sahayanathan, Nijil Mankuzhiyil, Pankaj Kushwaha, Ranjeev Misra, and Naseer Iqbal. Clues on high-energy emission mechanism from blazar 3C 454.3 during 2015 August flare. *Mon. Not. R. Astron. Soc.*, 470(3):3283–3299, Sep 2017. ISSN 0035-8711. doi: 10.1093/mnras/stx1194.

[126] F. Acero et al. Fermi Large Area Telescope Third Source Catalog. *apjs*, 218(2):23, June 2015. doi: 10.1088/0067-0049/218/2/23.

[127] M. Villata et al. The unprecedented optical outburst of the quasar <ASTROBJ>3C 454.3</ASTROBJ>. The WEBT campaign of 2004-2005. *aap*, 453(3):817–822, July 2006. doi: 10.1051/0004-6361:20064817.

[128] Raj Prince, Pratik Majumdar, and Nayantara Gupta. Long-term Study of the Light Curve of PKS 1510-089 in GeV Energies. *Astrophys. J.*, 844(1):62, Jul 2017. ISSN 0004-637X. doi: 10.3847/1538-4357/aa78f4.

[129] Raj Prince, Gayathri Raman, Joachim Hahn, Nayantara Gupta, and Pratik Majumdar. Fermi-Large Area Telescope Observations of the Brightest Gamma-Ray Flare Ever Detected from CTA 102. *Astrophys. J.*, 866(1):16, Oct 2018. ISSN 0004-637X. doi: 10.3847/1538-4357/aadadb.

[130] A. A. Abdo et al. Gamma-ray Light Curves and Variability of Bright Fermi-detected Blazars. *apj*, 722(1):520–542, October 2010. doi: 10.1088/0004-637X/722/1/520.

[131] A. A. Abdo et al. Spectral Properties of Bright Fermi-Detected Blazars in the Gamma-Ray Band. *apj*, 710(2):1271–1285, February 2010. doi: 10.1088/0004-637X/710/2/1271.

[132] S. Vercellone et al. The Brightest Gamma-Ray Flaring Blazar in the Sky: AGILE and Multi-wavelength Observations of 3C 454.3 During 2010 November. *apjl*, 736 (2):L38, August 2011. doi: 10.1088/2041-8205/736/2/L38.

[133] J. Hahn. GAMERA - a new modeling package for non-thermal spectral modeling. In *34th International Cosmic Ray Conference (ICRC2015)*, volume 34 of *International Cosmic Ray Conference*, page 917, July 2015.

[134] E. Massaro, M. Perri, P. Giommi, and R. Nesci. Log-parabolic spectra and particle acceleration in the BL Lac object Mkn 421: Spectral analysis of the complete

BeppoSAX wide band X-ray data set. *Astron. Astrophys.*, 413:489–503, Jan 2004. ISSN 0004-6361. doi: 10.1051/0004-6361:20031558.

[135] George R. Blumenthal and Robert J. Gould. Bremsstrahlung, Synchrotron Radiation, and Compton Scattering of High-Energy Electrons Traversing Dilute Gases. *Rev. Mod. Phys.*, 42(2):237–271, 1970. ISSN 0034-6861. doi: 10.1103/RevModPhys.42.237.

[136] Malcolm S. Longair. *High Energy Astrophysics*. Feb 2011. URL `https://ui.adsabs.harvard.edu/abs/2011hea..book.....L/abstract`.

[137] G. Bonnoli, G. Ghisellini, L. Foschini, F. Tavecchio, and G. Ghirlanda. The γ-ray brightest days of the blazar 3C 454.3. *Mon. Not. R. Astron. Soc.*, 410(1):368–380, Jan 2011. ISSN 0035-8711. doi: 10.1111/j.1365-2966.2010.17450.x.

[138] G. Ghisellini and F. Tavecchio. Canonical high-power blazars. *Mon. Not. R. Astron. Soc.*, 397(2):985–1002, Aug 2009. ISSN 0035-8711. doi: 10.1111/j.1365-2966.2009.15007.x.

[139] Charles D. Dermer and Govind Menon. *High Energy Radiation from Black Holes*. Princeton University Press, Princeton, NJ, USA, Nov 2009. ISBN 978-0-69114408-5. URL `https://press.princeton.edu/books/paperback/9780691144085/high-energy-radiation-from-black-holes`.

[140] Vaidehi S. Paliya. Fermi-Large Area Telescope Observations of the Exceptional Gamma-Ray Flare from 3C 279 in 2015 June. *Astrophys. J.*, 808(2):L48, Aug 2015. ISSN 0004-637X. doi: 10.1088/2041-8205/808/2/L48.

[141] R. J. Protheroe. Factors Determining Variability Time in Active Galactic Nucleus Jets. *Publ. Astron. Soc. Aust.*, 19(4):486–498, 2002. ISSN 1323-3580. doi: 10.1071/AS02008.

[142] Alok C. Gupta et al. A peculiar multiwavelength flare in the blazar 3C 454.3. *mnras*, 472(1):788–798, November 2017. doi: 10.1093/mnras/stx2072.

[143] Atreyee Sinha et al. On the Spectral Curvature of VHE Blazar 1ES 1011+496: Effect of Spatial Particle Diffusion. *Astrophys. J.*, 836(1):83, Feb 2017. ISSN 0004-637X. doi: 10.3847/1538-4357/836/1/83.

[144] A. A. Abdo et al. The Spectral Energy Distribution of Fermi Bright Blazars. *apj*, 716(1):30–70, June 2010. doi: 10.1088/0004-637X/716/1/30.

[145] Svetlana G. Jorstad et al. A Tight Connection between Gamma-Ray Outbursts and Parsec-scale Jet Activity in the Quasar 3C 454.3. *apj*, 773(2):147, August 2013. doi: 10.1088/0004-637X/773/2/147.

[146] Minfeng Gu, Xinwu Cao, and D. R. Jiang. On the masses of black holes in radio-loud quasars. *Mon. Not. R. Astron. Soc.*, 327(4):1111–1115, Nov 2001. ISSN 0035-8711. doi: 10.1046/j.1365-8711.2001.04795.x.

[147] D. V. Khangulyan, M. V. Barkov, V. Bosch-Ramon, F. A. Aharonian, and A. V. Dorodnitsyn. Star-Jet Interactions and Gamma-Ray Outbursts from 3C454.3. *Astrophys. J.*, 774(2):113, Sep 2013. ISSN 0004-637X. doi: 10.1088/0004-637X/774/2/113.

[148] S. Saito, Ł. Stawarz, Y. T. Tanaka, T. Takahashi, M. Sikora, and R. Moderski. Time-dependent Modeling of Gamma-Ray Flares in Blazar PKS1510–089. *Astrophys. J.*, 809(2):171, Aug 2015. ISSN 0004-637X. doi: 10.1088/0004-637X/809/2/171.

[149] William J. Potter. Modelling blazar flaring using a time-dependent fluid jet emission model - an explanation for orphan flares and radio lags. *Mon. Not. R. Astron. Soc.*, 473(3):4107–4121, Jan 2018. ISSN 0035-8711. doi: 10.1093/mnras/stx2371.

[150] R. D. Blandford and A. Königl. Relativistic jets as compact radio sources. *apj*, 232:34–48, August 1979. doi: 10.1086/157262.

[151] A. A. Abdo et al. Early Fermi Gamma-ray Space Telescope Observations of the Quasar 3C 454.3. *apj*, 699(1):817–823, July 2009. doi: 10.1088/0004-637X/699/1/817.

[152] Susanna Kohler and Krzysztof Nalewajko. Turbulent spectra of the brightest gamma-ray flares of blazars. *Mon. Not. R. Astron. Soc.*, 449(3):2901–2909, May 2015. ISSN 0035-8711. doi: 10.1093/mnras/stv478.

[153] A. L. Fey et al. The Second Extension of the International Celestial Reference Frame: ICRF-EXT.1. *Astron. J.*, 127(6):3587–3608, Jun 2004. ISSN 0004-6256. doi: 10.1086/420998.

[154] Michael S. Shaw et al. SPECTROSCOPY OF BROAD-LINE BLAZARS FROM 1LAC. *Astrophys. J.*, 748(1):49, Mar 2012. ISSN 0004-637X. doi: 10.1088/0004-637x/748/1/49.

[155] I. Nestoras et al. Broad band radio outburst of gamma-ray flaring blazar 4C+28.07. *The Astronomer's Telegram*, 3674:1, October 2011.

[156] F. K. Schinzel and S. Ciprini. Fermi LAT detection of increasing gamma-ray activity of blazar 4C +28.07. *The Astronomer's Telegram*, 3670:1, October 2011.

[157] K. V. Sokolovsky, F. D'Ammando, F. K. Schinzel, and J. A. Kennea. Swift follow up observations of the flaring gamma-ray blazar 4C +28.07. *The Astronomer's Telegram*, 3676:1, October 2011.

[158] L. Carrasco et al. A new NIR flare of the Blazar 4C+28.07. *The Astronomer's Telegram*, 5711:1, January 2014.

[159] M. L. Lister et al. MOJAVE. XVII. Jet Kinematics and Parent Population Properties of Relativistically Beamed Radio-loud Blazars. *Astrophys. J.*, 874(1):43, Mar 2019. ISSN 1538-4357. doi: 10.3847/1538-4357/ab08ee.

[160] E. Angelakis et al. The F-GAMMA program: multi-wavelength AGN studies in the Fermi-GST era. *arXiv e-prints*, art. arXiv:1006.5610, June 2010.

[161] L. Fuhrmann et al. Detection of significant cm to sub-mm band radio and γ-ray correlated variability in Fermi bright blazars. *Mon. Not. R. Astron. Soc.*, 441(3): 1899–1909, Jul 2014. ISSN 0035-8711. doi: 10.1093/mnras/stu540.

[162] E. Angelakis et al. Radio jet emission from GeV-emitting narrow-line Seyfert 1 galaxies. *Astron. Astrophys.*, 575:A55, Mar 2015. ISSN 0004-6361. doi: 10.1051/0004-6361/201425081.

[163] E. . Angelakis et al. F-GAMMA: Multi-frequency radio monitoring of Fermi blazars - The 2.64 to 43 GHz Effelsberg light curves from 2007–2015. *Astron. Astrophys.*, 626:A60, Jun 2019. ISSN 0004-6361. doi: 10.1051/0004-6361/201834363.

[164] Stephen E. Healey et al. CGRaBS: An All-Sky Survey of Gamma-Ray Blazar Candidates. *Astrophys. J. Suppl. Ser.*, 175(1):97–104, Mar 2008. ISSN 0067-0049. doi: 10.1086/523302.

[165] Jeffrey D. Scargle, Jay P. Norris, Brad Jackson, and James Chiang. STUDIES IN ASTRONOMICAL TIME SERIES ANALYSIS. VI. BAYESIAN BLOCK REPRESENTATIONS. *Astrophys. J.*, 764(2):167, Feb 2013. ISSN 0004-637X. doi: 10.1088/0004-637x/764/2/167.

[166] Manuel Meyer, Jeffrey D. Scargle, and Roger D. Blandford. Characterizing the Gamma-Ray Variability of the Brightest Flat Spectrum Radio Quasars Observed with the Fermi LAT. *Astrophys. J.*, 877(1):39, May 2019. ISSN 1538-4357. doi: 10.3847/1538-4357/ab1651.

[167] R. A. Edelson and J. H. Krolik. The Discrete Correlation Function: A New Method for Analyzing Unevenly Sampled Variability Data. *Astrophys. J.*, 333:646, Oct 1988. ISSN 0004-637X. doi: 10.1086/166773.

[168] Raj Prince, Nayantara Gupta, and Krzysztof Nalewajko. Two-zone Emission Modeling of PKS 1510-089 during the High State of 2015. *Astrophys. J.*, 883(2):137, Sep 2019. ISSN 1538-4357. doi: 10.3847/1538-4357/ab3afa.

[169] D. Emmanoulopoulos, I. M. McHardy, and I. E. Papadakis. Generating artificial light curves: revisited and updated. *Mon. Not. R. Astron. Soc.*, 433(2):907–927, Aug 2013. ISSN 0035-8711. doi: 10.1093/mnras/stt764.

[170] W. Max-Moerbeck et al. Time correlation between the radio and gamma-ray activity in blazars and the production site of the gamma-ray emission. *Mon. Not. R. Astron. Soc.*, 445(1):428–436, Nov 2014. ISSN 0035-8711. doi: 10.1093/mnras/stu1749.

[171] T. Savolainen et al. Relativistic beaming and gamma-ray brightness of blazars. *Astron. Astrophys.*, 512:A24, Mar 2010. ISSN 0004-6361. doi: 10.1051/0004-6361/200913740.

[172] I. Liodakis et al. F-GAMMA: variability Doppler factors of blazars from multiwavelength monitoring. *Mon. Not. R. Astron. Soc.*, 466(4):4625–4632, May 2017. ISSN 0035-8711. doi: 10.1093/mnras/stx002.

[173] A. B. Pushkarev, Y. Y. Kovalev, M. L. Lister, and T. Savolainen. Jet opening angles and gamma-ray brightness of AGN. *Astron. Astrophys.*, 507(2):L33–L36, Nov 2009. ISSN 0004-6361. doi: 10.1051/0004-6361/200913422.

[174] Linhui Wu, Qingwen Wu, Dahai Yan, Liang Chen, and Xuliang Fan. Constraints on the Location of γ-Ray Sample of Blazars with Radio Core-shift Measurements. *Astrophys. J.*, 852(1):45, Jan 2018. ISSN 1538-4357. doi: 10.3847/1538-4357/aa9b7e.

[175] A. Celotti, P. Padovani, and G. Ghisellini. Jets and accretion processes in active galactic nuclei: further clues. *Mon. Not. R. Astron. Soc.*, 286(2):415–424, Apr 1997. ISSN 0035-8711. doi: 10.1093/mnras/286.2.415.

[176] Laura Maraschi and Fabrizio Tavecchio. The Jet-Disk Connection and Blazar Unification. *Astrophys. J.*, 593(2):667–675, Aug 2003. ISSN 0004-637X. doi: 10.1086/342118.

[177] Jin Zhang, Xiao-Na Sun, En-Wei Liang, Rui-Jing Lu, Ye Lu, and Shuang-Nan Zhang. RELATIVISTIC JET PROPERTIES OF GeV–TeV BLAZARS AND POSSIBLE IMPLICATIONS FOR THE JET FORMATION, COMPOSITION, AND CAVITY KINEMATICS. *Astrophys. J.*, 788(2):104, May 2014. ISSN 0004-637X. doi: 10.1088/0004-637x/788/2/104.

[178] D. R. Xiong and X. Zhang. Intrinsic γ-ray luminosity, black hole mass, jet and accretion in Fermi blazars. *Mon. Not. R. Astron. Soc.*, 441(4):3375–3395, Jul 2014. ISSN 0035-8711. doi: 10.1093/mnras/stu755.

[179] T. Hovatta, E. Valtaoja, M. Tornikoski, and A. Lähteenmäki. Doppler factors, Lorentz factors and viewing angles for quasars, BL Lacertae objects and radio galaxies. *aap*, 494(2):527–537, February 2009. doi: 10.1051/0004-6361:200811150.

[180] Raj Prince. Multi-frequency Variability Study of Ton 599 during the High Activity of 2017. *Astrophys. J.*, 871(1):101, Jan 2019. ISSN 1538-4357. doi: 10.3847/1538-4357/aaf475.

[181] A. P. Marscher and W. K. Gear. Models for high-frequency radio outbursts in extragalactic sources, with application to the early 1983 millimeter-to-infrared flare of 3C 273. *Astrophys. J.*, 298:114–127, Nov 1985. ISSN 0004-637X. doi: 10.1086/163592.

[182] E. Valtaoja, H. Terasranta, S. Urpo, N. S. Nesterov, M. Lainela, and M. Valtonen. Five years monitoring of extragalactic radio sources. III. Generalized shock models and the dependence of variability on frequency. *aap*, 254:71–79, February 1992.

[183] F. K. Schinzel et al. Relativistic outflow drives γ-ray emission in 3C 345. *aap*, 537: A70, January 2012. doi: 10.1051/0004-6361/201117705.

[184] M. Orienti et al. Radio and γ-ray follow-up of the exceptionally high-activity state of PKS 1510-089 in 2011. *Mon. Not. R. Astron. Soc.*, 428(3):2418–2429, Jan 2013. ISSN 0035-8711. doi: 10.1093/mnras/sts201.

[185] J. Aleksić et al. MAGIC gamma-ray and multi-frequency observations of flat spectrum radio quasar PKS 1510-089 in early 2012. *aap*, 569:A46, September 2014. doi: 10.1051/0004-6361/201423484.

[186] H. E. S. S. Collaborationet al. H.E.S.S. and MAGIC observations of a sudden cessation of a very-high-energy γ-ray flare in PKS 1510$-$089 in May 2016. *aap*, 648: A23, April 2021. doi: 10.1051/0004-6361/202038949.

[187] S. R. Patel, D. Bose, N. Gupta, and M. Zuberi. Broadband modelling of Orphan gamma ray flares. *J. High Energy Astrophys.*, 29:31–39, Mar 2021. ISSN 2214-4048. doi: 10.1016/j.jheap.2020.12.001.

[188] M. Cerruti, W. Benbow, X. Chen, J. P. Dumm, L. F. Fortson, and K. Shahinyan. Luminous and high-frequency peaked blazars: the origin of the γ-ray emission from PKS 1424+240. *Astron. Astrophys.*, 606:A68, Oct 2017. ISSN 0004-6361. doi: 10.1051/0004-6361/201730799.

[189] Rui Xue et al. A Two-zone Model for Blazar Emission: Implications for TXS 0506+056 and the Neutrino Event IceCube-170922A. *Astrophys. J.*, 886(1):23, Nov 2019. ISSN 1538-4357. doi: 10.3847/1538-4357/ab4b44.

[190] M. G. Aartsen et al. The Contribution of Fermi-2LAC Blazars to Diffuse TeV-PeV Neutrino Flux. *apj*, 835(1):45, January 2017. doi: 10.3847/1538-4357/835/1/45.

[191] Xavier Rodrigues et al. Multiwavelength and Neutrino Emission from Blazar PKS

1502 + 106. *Astrophys. J.*, 912(1):54, May 2021. ISSN 0004-637X. doi: 10.3847/1538-4357/abe87b.

[192] Saikat Das, Nayantara Gupta, and Soebur Razzaque. PeV–EeV Neutrinos from Gamma-Ray Blazars due to Ultrahigh-energy Cosmic-Ray Propagation. *Astrophys. J.*, 910(2):100, Apr 2021. ISSN 0004-637X. doi: 10.3847/1538-4357/abe4cd.